STUDY OF THE EFFECTS OF THE DRYOUT FUNCTION PARAMETERS IN HETEROGENEOUS RESERVOIRS AND EXPERIMENTAL CHALLENGES OF CARBON DIOXIDE FOAMS IN MICROFLUIDICS

Diego Sanchez

Study of the effects of the dryout function parameters in heterogeneous reservoirs and experimental challenges of carbon dioxide foams in microfluidics

By

Diego Sanchez

in partial fulfilment of the requirements for the degree of

Master of Science
in Applied Earth Sciences

at the Delft University of Technology,
to be defended publicly on October 31, 2018

Student number 4520564

Supervisor:
Dr. R. Farajzadeh — Delft University of Technology

Thesis committee:
Dr. G. Bertotti — Delft University of Technology
Dr. KHAA Wolf — Delft University of Technology
Dr. D. Voskov — Delft University of Technology
Dr. SYF Vincent-Bonnieu — Delft University of Technology / Shell GSI
Dr. S. Kahrobaei — TNO

TU Delft

TU Delft

Table of Contents

1 Introduction 1

1.1 Gas injection 1

1.2 Foams 2

1.2.1 Foam apparent viscosity and quality 3

1.2.2 Foam flow regimes 4

1.2.3 Effect of permeability on foam behavior 5

1.2.4 Foam generation mechanisms 7

1.2.5 Foam modelling 8

2 Foam Simulation 12

2.1 Non-communicating layers simulation case 15

2.2 Communicating layers simulation case 21

2.3 High *fmmob* contrast simulation case 28

2.4 Conclusions 34

3 Experimental Section 35

3.1 Microfluidics Introduction 35

3.1.1 Hydraulic Capacitance and bottle neck effect 35

3.1.2 Mixing in Microfluidics 35

3.1.3 Microfluidic studies in foams 36

3.2 Experimental motivation 39

3.2.1 Experimental Set-up design 40

3.2.2 Materials 41

3.2.3 Microchip Characterization 42

3.2.4 Pressure and temperature operating point 44

3.2.5 Non-aqueous phase density estimation 44

3.2.6 Non-aqueous phase mixing analysis 47

3.2.7 Experiment velocity set point 48

3.3 Experimental Output 49

3.3.1 Experimental setbacks 49

3.4 Conclusions and way forward 61

Appendix A. Volumetric flowrate Determination 63

Appendix B. Supplementary figures for Foam injection 65

i. Pressure profile comparing *epdry* low and high for Case 1-Communicating layers 65

ii. Apparent viscosity profile comparing *epdry* low and high for Case 1-Communicating layers 66

iii. Apparent viscosity Profiles comparison for Case 2-high *fmmob* contrast 67

Nomenclature 68

References 69

List of figures

Figure 1.1 Gas injection drawbacks (adapted from Advanced Resources International, 2010) 2
Figure 1.2 Foam bulk structure (Schramm, 2005). 2
Figure 1.3 Schematic representations of porous media with (A) no foam, (B) weak foam and (C) strong foam (Sheng, 2013). 3
Figure 1.4 Contour plots of pressure drop caused by foam as a function of fluid velocities. Left with a constant quality line presented in black. Right with a constant velocity line (Li, 2016). 4
Figure 1.5 Foam quality scan curve 5
Figure 1.6. Effect of permeability on capillary pressure (Farajzadeh et al., 2015) 5
Figure 1.7 Schematic representation of the limiting capillary pressure and critical water saturation (Farajzadeh et al., 2015) 6
Figure 1.8 Relation between limiting capillary pressure and permeability (Farajzadeh et al. 2015) 7
Figure 1.9 Effect of single foam formulation on different cores. (Farajzadeh et al. 2015) 7
Figure 1.10 Snap off mechanism (adapted from (Almajid et al. 2016). 8
Figure 1.11 Lamellae division mechanism (Almajid et al. 2016). 8
Figure 1.12 Leave behind Mechanism (Almajid et al. 2016). 8
Figure 1.13 F_w function plotted for same *fmdry* and different *epdry* (5000 light green, 138 blue) 10
Figure 1.14 Effect of foam on mobility. Left: high perm layer. Right: low perm layer 10
Figure 1.15 Foam quality scan for *k=1500 mD, fmdry=0.27, fmmob=5000* 11
Figure 2.1. Schematic representation of reservoir 12
Figure 2.2. Apparent viscosity vs. water saturation for case 1. Left: LPL. Right: HPL. 14
Figure 2.3 Apparent viscosity vs. water saturation for case 2. Left: LPL. Right: HPL. 14
Figure 2.4. Recovery factor for non-communicating layers as function of injection quality. Top left: LPL. Top Right: HPL. Bottom: Total reservoir recovery factor 15
Figure 2.5. Production profile for non-communicating layers as function of time. Left: low perm layer. Right: High perm layer 16
Figure 2.6 Saturation Profile for non-communicating layers as function of position at different dimensionless times. Top left: fg=0.50. Top right: fg=0.95. Bottom: fg=1.00 16
Figure 2.7 Foam apparent viscosity in LPL for non-communicating layers as function of position at different dimensionless times. Left: fg =0.50. Right: fg=0.95. Bottom: fg=1.0 17
Figure 2.8 Foam apparent viscosity in HPL for non-communicating layers as function of position at different dimensionless times. Left: fg =0.50. Right: fg=0.95. Bottom: fg=1.0 18
Figure 2.9 Pressure profile in LPL for non-communicating layers as function of position. Left: fg =0.50. Right: fg=0.95. Bottom: fg=1.0 19
Figure 2.10 Pressure profile in HPL for non-communicating layers as function of position. Left: fg =0.50. Right: fg=0.95. Bottom: fg=1.0 20
Figure 2.11 Pressure profiles for communicating layers. Top left: fg=.50 *epdry* low. Top right fg=.50 *epdry* high. Middle left: fg=.95 *epdry* low. Middle right: fg=.95 *epdry* high. Bottom left: fg=1.0 *epdry* low. Bottom right: fg=1.0 *epdry* high 22
Figure 2.12 Pressure difference between HPL and LPL (communicating layers) for different injection qualities and injected volumes. Left: fg=0.51.Right: 0.95. Bottom: 1.0 23
Figure 2.13 Flowrate fraction through HPL and LPL at 0.4PV (communicating layers) for different injection qualities. Left: fg=0.50. Right: fg=0.95. Bottom fg=1.0 24
Figure 2.14 Foam Mobility per layer (communicating layers) at different injection qualities and 0.4PV. Left: fg=0.50. Right: fg=0.95. Bottom: fg=1.0 25

Figure 2.15 Water Saturation Profile for communicating layers at different injection qualities and dimensionless times. left: fg=0.50. right: fg=0.95. Bottom: fg=1.0 26
Figure 2.16 Recovery factor for communicating layers at different injection qualities. Top left: LPL. Top Right: HPL. Bottom: Total 27
Figure 2.17 Pressure profile for high *fmmob* contrast for both *epdry* cases. Top left: fg=.50 *epdry* low. Top right fg=.50 *epdry* high. Middle left: fg=.95 *epdry* low. Middle right: fg=.95 *epdry* high. Bottom left: fg=1.0 *epdry* low. Bottom right: fg=1.0 *epdry* high 28
Figure 2.18. Pressure difference profiles between LPL and HPL for different injection volumes. Top left: fg=0.50 low *epdry*. Top right: fg=0.5 high *epdry*. Middle left: fg=0.95 low *epdry*. Middle right: fg=0.95 high *epdry*. Bottom left: fg=1.0 low *epdry*. Bottom right: fg=1.0 high *epdry*. 29
Figure 2.19 Water Saturation Profiles for high *fmmob* contrast at different injection qualities and injected volumes. left: fg=0.50. right: fg=0.95. Bottom: fg=1.0 30
Figure 2.20 Foam Mobility per layer (high *fmmob* contrast) at different injection qualities. Left: fg=0.50. Right: fg=0.95. Bottom: fg=1.0 31
Figure 2.21 Water saturation in reservoir at 0.6PV Top 4 layers represent HPL and 4 bottom layers represent LPL. Top right: fg=0.5 high *epdry*. Middle left: fg=0.95 low *epdry*. Middle right: fg=0.95 high *epdry*. Bottom left: fg=1.0 low *epdry*. Bottom right: fg=1.0 high *epdry* 32
Figure 2.22 Recovery factor at different injection qualities (high *fmmob* contrast). Top left: LPL. Top Right: HPL. Bottom: Total 33
Figure 3.1 Two inputs one output microfluidic device with only diffusion occurring in the x-direction 36
Figure 3.2 Diagram of foam generation according to injection conditions (Quennouz et al., 2012) 37
Figure 3.3 Oil foam interactions according to Schramm et al. (1990) 38
Figure 3.4 Foam-oil interactions. Foam types as viewed from microscope 39
Figure 3.5 Kahrobaei et al. (2017) CO2 foam apparent viscosity regimes 40
Figure 3.6 Microfluidic set-up Schematic 41
Figure 3.7 Chip design provided by Micronit 42
Figure 3.8 10/11 x 849 gaussian pore pattern etched on micromodel 42
Figure 3.9 Microfluidic chip permeability calculation 43
Figure 3.10. 2D Porosity and permeability graphs 44
Figure 3.11 Phase diagram of $CO_2 – C_{10}$ binary system. Calculated using PVT sim and Peng Robinson EOS 44
Figure 3.12 $CO_2 – C_{10}$ Density experimental and EOS comparison at 10MPa and 313K 45
Figure 3.13 $CO_2 – C_{10}$ Density experimental and EOS comparison at 10MPa and 323K 45
Figure 3.14 Error between HEOS and experimental data at 323 K 46
Figure 3.15 Error between HEOS and experimental data at 313 K 46
Figure 3.16 Flowrate uncertainty at 200 ft/day for f_g=1 46
Figure 3.17 Reynolds and Peclet number sensitivity analysis for different diffusion coefficients 47
Figure 3.18 Sensitivity of mixing order time and distance for different Diffusion coefficients 47
Figure 3.19 CO2 flowrate with 2.5 ml syringe. (Left No CO2 dissolved in brine. Right CO2 dissolved in brine compensated) 48
Figure 3.20 Foam scans: Pressure drop as a function of pore volumes. A,B microfluidics; C core flood (Kagoro, 2017) 50
Figure 3.21 Pressure drop behavior for all Test 2: X=1, Fg=0.5 51
Figure 3.22 Pressure drop zoom for Test 2: X=1, Fg=0.5, showing intervals at which fluid changes are seen in the microscope 52
Figure 3.23. Test 2 Time lapse. A-M Images exhibit the time at which phase alternation occurs. Images taken at 20X zoom. 53
Figure 3.24 Pressure behavior for Test 2: X=1, Fg=0.8 55

Figure 3.25 Test 6 Time lapse. A-F Images that exhibit the time at which fluid alternation occurs. 55
Figure 3.26 Backflow during experiments 56
Figure 3.27 Fluid Leak Evidence. A Barrel. B Plunger 56
Figure 3.28. Corrosion in 2.5 ml syringe plunger 57
Figure 3.29 Pressure response during pump stalling 57
Figure 3.30. Debris particles clogging microchip entrance 58
Figure 3.31 Example of temperature and pressure fluctuations around the set point 59
Figure 0.1 Relative pressure difference between *epdry* high and low for different injection qualities and injected volumes. Left: f_g=0.50. Right: f_g=0.95. Bottom: f_g=1.0 65
Figure 0.2 Apparent Viscosity profiles for non-communicating layers for different qualities and injection volumes. Left: LPL. Right: HPL 66
Figure 0.3 Apparent Viscosity profiles for high *fmmob* contrast for different qualities and injection volumes. Left: LPL. Right: HPL 67

List of tables

Table 2-1 Brooks-Corey Relative permeability parameters 13
Table 2-2 STARS foam model parameters for case 1 13
Table 2-3 STARS foam model parameters for case 2 13
Table 3-1 Microfluidic chip characterization 43
Table 3-2 Harvard Apparatus PHD Ultra 4400 pump specification 48
Table 3-3 HA PHD 4400 Pump - Syringe combinations performance 48
Table 3-4 Experimental set points 49
Table 3-5 Experiments summary 49
Table 3-6, Dimensionless time at which phases alternate in Figure 3.23 54
Table 3-7 Thermal expansion inputs 59
Table 3-8. Experimental Risk assessment 60
Table 0-1 Volumetric flowrates formula 63

Abstract

Gas injection processes suffer from poor volumetric sweep efficiency due to phenomena such as viscous fingering caused by density contrast between the injected gas and the displaced fluid, channeling due to heterogeneities in the reservoir and gravity override due to the inherent lower density of gas. One possible way to overcome these negative effects is by foaming the gas. Foam can be defined as a dispersion of gas separated by lamellae in a continuous liquid phase. Lamellae stability is enhanced by adding surfactants to the aqueous phase (Lake, 2014). The underlying idea is that the pitfalls of gas injection can be overcome by trapping the gas and therefore reducing its mobility. The benefits of foam flooding have been reported by several authors (Almaqbali et al., 2017, Li et al., 2009, Chalbaud et al., 2002, Patil et al., 2018) however, to implement field scale projects, an accurate representation of foams in models that can be applied to reservoir simulators is of paramount importance. In this sense, two main families of foam modelling exist today. One family referred as population balance models, treat foam texture and bubble size explicitly and another family, that treats foam texture implicitly by applying a mobility reduction factor to gas mobility.

In the first part of this document, a model that treats foam texture implicitly will be used to evaluate foam performance in a heterogenous reservoir consisting of two layers with different permeabilities. The model known as STARS (Computer Modelling Group, 2010) reduces gas mobility using semiempirical functions that represent the physics governing foam texture. One of the functions used by the model is the dryout function, which represents the effects of water saturation on foam coalescence. This function is tuned by a couple parameters, namely, *fmdry* and *epdry* that control the water saturation at which foam dries out and how fast it dries out, in other words, how abrupt its collapse is. Farajzadeh et. al, (2015) found that these parameters were permeability dependent.

Inspired by these findings, in the modelling section of this project, foam performance in a two layer reservoir with different permeabilities under varying injection conditions is assessed. Each layer will have its unique set of parameters, namely, *fmmob*, *epdry* and *fmdry*. We are interested in seeing the effects that *epdry* has on foam performance and the effects of having vastly contrasting foam strengths between layers (large *fmmob* contrast). The results suggest that *epdry* can have significant impact on foam performance in the high quality regime. Interestingly, it was found that large *fmmob* contrast reduce vertical conformance and can reduce recovery efficiency in the high quality regime.

It is known that oil can have negative impact on foam stability, however most studies treat gas and oil as different phases. Under miscible conditions, oil and gas become one phase and the extent to how oil destabilizes foam is not clearly understood. Kahrobaei et. al (2017) found in core flood experiments a unique rheological behavior in foams with miscible mixtures of Carbon Dioxide – Decane. Their experiments showed three distinguishable apparent viscosity regimes depending on Carbon dioxide fraction. Regime 1, in which apparent viscosity increased with increasing CO_2 fraction; Regime 2 in which apparent viscosity decreased with increasing CO_2 fraction; and Regime 3 in which apparent viscosity is constant independently of the CO_2 molar composition.

Inspired by Kahrobaei et. al, (2017) findings, the second part of the project attempts to investigate, using microfluidics, the effects in foam texture caused by compositional changes in an AOS surfactant solution and a miscible Carbon Dioxide – Decane mixture. Unfortunately, due to set-up limitations and inability to reliably mix the components, the experiments were inconclusive. Nonetheless, valuable lessons learnt are presented that will facilitate the experimental approach if someone decides to continue with this line of investigation.

1 Introduction

During the production phase of a reservoir, three main phases of hydrocarbon recovery can be identified: Primary, secondary and tertiary recovery. During the primary phase, natural drive mechanisms, such as pressure depletion, gas-drive or water-drive are used to extract crude oil from the reservoir. Recoveries as low as 10% are common during primary recovery phase (Speight, 2016). This stage is followed by a secondary recovery, where improved oil recovery techniques, IOR, such as water flooding or gas injection are used to improve the sweep efficiency and pressure maintenance, which can improve the recovery on average up to 30% (Lake, 2014). Once these recovery methods are no longer capable of maintaining production requirements, tertiary recovery methods can be applied. The recovery at this latter stage involves the use of thermal, chemical or phase behavior alteration processes. These methods are often referred as enhanced oil recovery (EOR) methods; however, they don't just apply to the tertiary phase recovery as they can be used at earlier stages to enhance the ultimate recovery factor.

1.1 Gas injection

Gas injection is a common strategy for enhancing oil recovery. In comparison with water injection, gas injection can result in lower residual oil saturation because of good microscopic sweep efficiency of the gas. Since the injectivity of gas is high, it allows larger injection rates for a fixed pressure drawdown. Furthermore, if gas injection is done under miscible conditions, it will improve the ultimate recovery since the interfacial tension between the injected fluid and oil vanishes, leaving, in theory, no residual phases (Lake, 2014).

In a miscible displacement, two types of miscibility can take place, i.e., first contact miscibility –FCM- and multiple contact miscibility -MCM. FCM occurs when the gas and oil form a single phase when mixed in any proportion. In MCM two drives are available: condensing and vaporizing. In vaporizing the injected fluid, e.g. gas, is enriched by extracting the lighter components of the reservoir oil into the gas phase. In contrast, during a condensing drive, the heavier components of the injected gas are extracted and incorporated into the reservoir oil. In general, the heavier the reservoir oil, the richer the injected gas needs to be.

Hydrocarbon gases are not the only suitable gases in gas flooding, other gases such as carbon dioxide or nitrogen are suitable as well. Carbon dioxide, CO_2, is often seen as an option due to its relatively low minimum miscibility pressure (MMP), which can be achieved under normal reservoir conditions. Moreover, in the midst of the increasing global warming concerns, the use of CO_2 in CCUS (carbon capture, utilization and sequestration) processes is gaining importance for EOR developments. Unlike Carbon dioxide, nitrogen is seldom never miscible with hydrocarbons and therefore its application is mainly related with foam floods.

CO_2 miscibility is a function of reservoir pressure, temperature and the chemical nature of the reservoir oil; however, despite the oil composition there is an inverse correlation between hydrocarbon weight and CO_2 solubility. To achieve a miscible displacement, CO_2 needs to be injected at pressures above the MMP. The resulting injected phase is either a "dense" or supercritical fluid depending on the temperature at which the injection is done. Although CO_2 and oil are not usually FCM, developed miscibility is achieved at the front of the injection bank trough vaporizing drive (Speight, 2016).

Despite the enhancements given by gas injection in terms of microscopic sweep efficiency, the ultimate recovery can remain low due to inefficient volumetric sweep efficiency as depicted in Figure 1.1. This low volumetric efficiency is an overall result of three main phenomena (Sheng, 2013)

- Viscous fingering caused by viscosity differences between the reservoir fluid and injected gas.
- Gravity override caused by density differences that the make the gas flow at the top of the reservoir.

- And channeling due to heterogeneities in the reservoir.

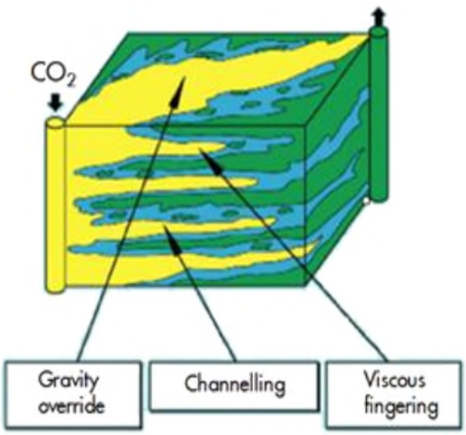

Figure 1.1 Gas injection drawbacks (adapted from Advanced Resources International, 2010)

As an alternative, to overcome the drawbacks mentioned, gas mobility can be reduced by using surfactants that adsorb at the interface liquid interface and create foams. The foam basics and application will be discussed in the following section.

1.2 Foams

As mentioned earlier, the objective of using foams in reservoir applications is mainly to overcome gas flooding drawbacks. Foam is defined as a dispersion of gas trapped in a continuous liquid phase. Lamellae stability is enhanced by adding surfactants to the aqueous phase (Lake, 2014). The liquid film trapping the gas, and therefore separating gas bubbles is called the lamellae. In field applications, foams can be created by co-injecting a gas and the aqueous surfactant solution or by an alternating injection scheme of gas and aqueous surfactant solution, SAG.

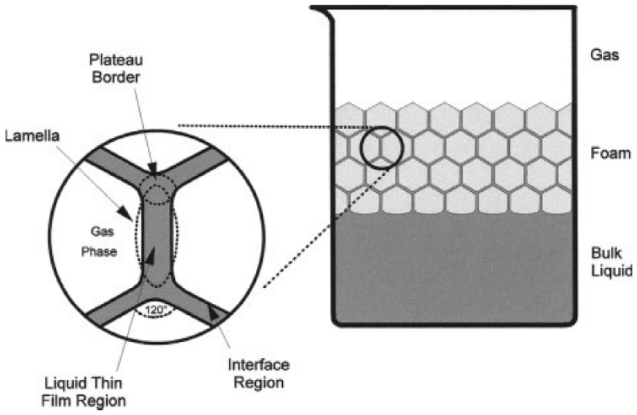

Figure 1.2 Foam bulk structure (Schramm, 2005).

Foams in porous media, unlike bulk foams, are more stable as they constantly experience in-situ lamellae creation and coalescence processes as they move through the reservoir (Sheng, 2013). As lamellae moves through the reservoir, it experiences viscous dissipation that further reduces gas mobility (Sheng, 2013). Figure 1.2 shows the terminology commonly used in literature to describe the physical aspects of foam structures.

Foams can be classified as either strong (fine-textured) or weak (coarse-textured) and the strength is given by the number of lamellas. Figure 1.3 depicts a schematic representation of weak and strong foams in a porous media, the thin blue films represent lamellas. Strong foams exhibit a fine texture where the increased lamellae density

vastly improves the apparent viscosity. In contrast, weak foams only cause a moderate improvement (Sheng, 2013). The apparent viscosity, which will be defined in the following section, is commonly used to refer to the foam strength, the higher the apparent viscosity the stronger the foam.

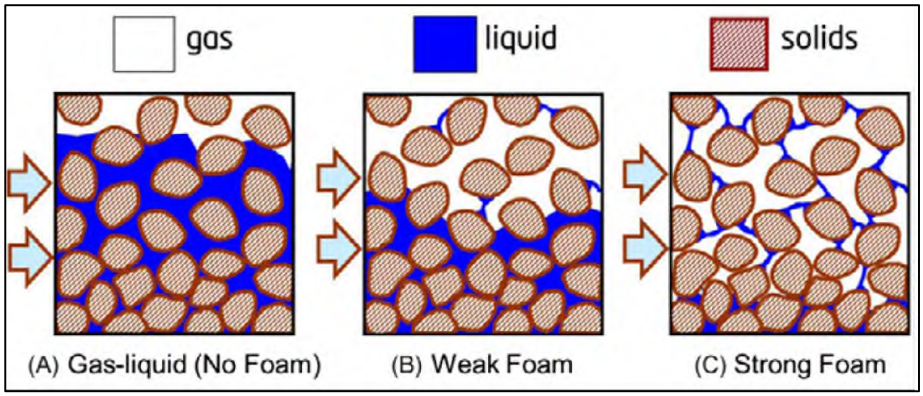

Figure 1.3 Schematic representations of porous media with (A) no foam, (B) weak foam and (C) strong foam (Sheng, 2013).

1.2.1 Foam apparent viscosity and quality

Foam exhibits an apparent viscosity of a few orders magnitude higher than its constituent gas, leading to a reduced mobility. The mobility reduction is not only caused by the trapping of bubbles within the porous media but also due to viscous dissipation associated with bubbles moving through pore throats (Sheng, 2013). Both these phenomena affect the pressure gradient in the porous media. Therefore, in most of the foam applications the pressure drop along a certain length of the porous media is measured and used as an indicator for foam flow behavior. The measured pressure drop can be converted to apparent viscosity using single-phase Darcy's law.

$$\mu_{app} = \frac{k}{u_t} \nabla p \qquad \text{Equation 1.2.1}$$

Where μ_{app} *[Pa.s]* is apparent viscosity, k [m^2] is the absolute permeability, u_t [m/s] represent the total velocity of the non-aqueous phase and the aqueous phase (surfactant solution), and ∇p [Pa/m] is the pressure gradient. For simplicity in nomenclature throughout the document, the aqueous phase will be referred as water phase and the non-aqueous phase will be referred as gas phase, unless it is referred to a miscible mixture of gas and another constituent. If the superscript *f* is used, it indicates that the gas phase is considered in "foam state" as opposed to no superscript, that indicates that it is considered in pure gas phase.

If a two phase Darcy flow, with a water and gas phases, Darcy's law can be written as:

$$u_t = k\left[\frac{k_{rw}}{\mu_w} + \frac{k_{rg}}{\mu_g}\right]\nabla p \qquad \text{Equation 1.2.2}$$

By combining Equation 1.2.1and Equation 1.2.2 the apparent viscosity can be defined in terms of relative permeabilities and viscosities, where the relative permeabilities are functions of water saturation. The ratio of permeability and viscosity of phase i is referred as mobility, λ_i [Pa.s/m^2]. When dealing with foams, it is assumed that the water phase mobility remains unaltered and the effects of foam are felt in the gas phase mobility (Bernard et al. 1965). Hence, foam apparent viscosity can be defined as

$$\mu_{app} = \left[\lambda_w + \lambda_g^f\right]^{-1} \qquad \text{Equation 1.2.3}$$

A parameter that will be referred often throughout the document is foam quality. Quality is defined as the ratio of gas injection rate and total injection rate; this ratio can be expressed in terms of superficial velocities as well and it is shown in Equation 1.2.4

$$f_g = \frac{q_g}{q_w + q_g} = \frac{u_g}{u_w + u_g} \qquad \text{Equation 1.2.4}$$

1.2.2 Foam flow regimes

The steady-state rheology of foam in porous media is tuned by the gas phase fractional flow or foam quality, f_g. Figure 1.4 presents pressure gradient contours as function of gas and water velocities. Here, two different regimes are clearly observed: a regime where pressure gradient contour plots are vertical and another where pressure gradient contour plots are horizontal. The former is referred as the low quality regime where the pressure gradient (or foam strength) is determined by the gas velocity. The latter is referred as the high-quality regime and in it, liquid velocity plays the dominant role in the pressure gradient.

In the high quality regime, bubble size becomes very sensitive to injection rates and foam behavior is governed by coalescence. The transition between regimes is given by the limiting capillary pressure, P_c^*. The dashed-dotted black line in Figure 1.4 left indicates a constant gas volume fraction (foam quality) at which the transition from high-quality to low-quality regime occurs. This quality is referred as the transition foam quality.

However, in most cases, laboratory experiments are conducted along a constant velocity line, represented by the red dashed-dotted line in Figure 1.4 right. The gas phase fraction (quality) is varying while the total injection velocity (u_g+u_w) is kept constant. A representation of such experiment is shown in Figure 1.5, this type of experiment represents a foam rheological behavior and is referred as foam quality scan.

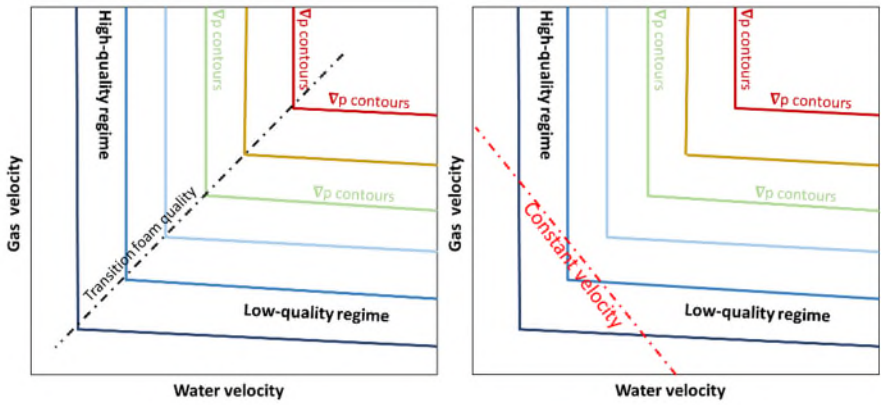

Figure 1.4 Contour plots of pressure drop caused by foam as a function of fluid velocities. Left with a constant quality line presented in black. Right with a constant velocity line (Li, 2016).

Foam scans allows investigation of steady-state foam behavior at both high- and low-quality regimes. The transition between high and low quality regimes can also be observed in this type of experiment. As it can be seen from Figure 1.5, in the low-quality regime the apparent viscosity is increased by increasing the foam quality until it reaches the transition foam quality. Thereafter, in the high-quality regime, the apparent viscosity starts to decrease by increasing the foam quality. The green dashed line represents a foam quality at which regime transition occurs, this line is equivalent to the black line from Figure 1.4. The rheological nature of foams can also be identified in this type of experiments, whereby in the low quality regime, a shear-thinning behavior is seen.

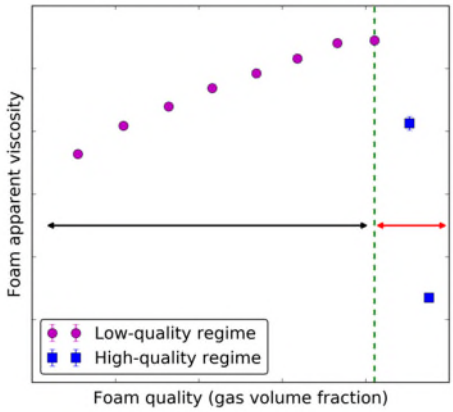

Figure 1.5 Foam quality scan curve

1.2.3 Effect of permeability on foam behavior

Reservoir rocks are in general heterogenous in nature (Peters, 2012) this implies that within the reservoir, differences in permeability, porosity and even fluid saturation are found. During a primary drainage process, the non-wetting phase, usually gas or oil, displaces the wetting phase, usually water. In this process, the non-wetting phase enters the porous media at a higher pressure than the wetting phase, displacing the wetting phase until it's finally held place by capillary forces. This creates a pressure difference within the displaced phase and the displacing phase, referred as the capillary pressure, one of the ways in which this pressure is represented is shown in Equation 1.2.5.

$$P_c = P_{nw} - P_w \qquad \text{Equation 1.2.5}$$

Capillary pressure can also be expressed in terms of the interfacial tension, the contact angle and radius of the interface, however, this will not be discussed, for the intention here is to relate the origins of capillary pressure, how it relates to saturation and permeability, and ultimately, how it affects foam stability.

As stated, when two phases are present within the reservoir it is expected to have capillary pressures that depend upon the relative fractions of the phases i.e. S_w and S_{nw}. Throughout this document, the properties that depend on the relative fractions of the phases will be referred in terms of water saturation, $S_{w,}$ unless explicitly stated.

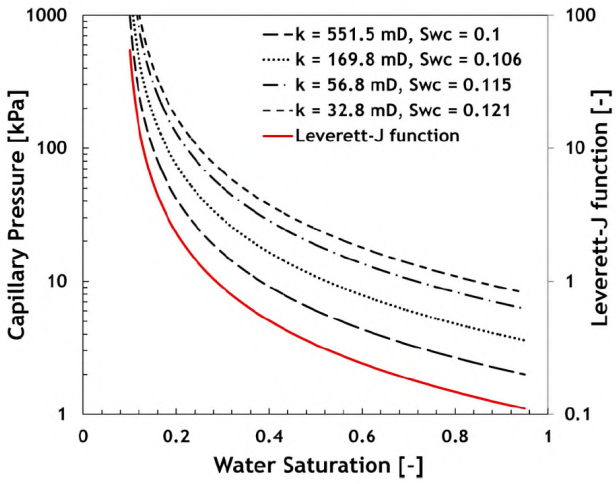

Figure 1.6. Effect of permeability on capillary pressure (Farajzadeh et al., 2015)

For a water-wet reservoir, the capillary pressure increases as S_w and permeability, *k,* decrease, as shown in Figure 1.6. By inspecting this figure, it can be seen that a strong coupling between water saturation, capillary pressure

and permeability exists. In section 1.2.2, it was discussed that there is a limit after which significant foam collapse occur. For a given fixed superficial velocity, the intersection of the iso-velocity (Figure 1.4 red dashed line) and the iso-quality transition line (Figure 1.4 black dashed line) determines the pressure gradient at which foam collapse starts, this pressure is referred as the limiting capillary pressure, Pc*. Therefore, due to the coupling between permeability, water saturation and capillary pressure, it is sound to imagine, that the limiting capillary pressure will depend on water saturation as well as permeability.

A schematic representation of a capillary pressure curve is presented in Figure 1.7. As capillary pressure increases, it draws water out of the lamellae (Rossen, 2013) drying the foam until it abruptly collapses (Khatib, Hirasaki and Falls, 1988). The red dashed line in Figure 1.7 represents the region where no foam will exist, and gas mobility will be significantly increased, ceasing the viscosifying effect of foam. The critical point where this occurs is determined by parameters that are foam formulation dependent such as surfactant concentration, water salinity, etc. and reservoir properties such as relative permeabilities, permeability, pressure, temperature etc. Nonetheless, the net effect of permeability on the limiting capillary pressure is predictable, and as shown in Figure 1.8, it exhibits a relation between limiting capillary pressure and permeability.

While Figure 1.6 shows the effect of water saturation and permeability on capillary pressure, and Figure 1.7 suggests that each capillary curve should have a unique critical saturation-pressure combination, they do not provide much idea on how permeability and the critical point relate. Farajzadeh (2015) found that there is a linear relation between the limiting capillary pressure and the inverse of the square root of permeability, this relation is shown in Figure 1.8. This linear relation is maintained, regardless of the petrophysical parameters used to describe the reservoir rock, nonetheless the accuracy of the values depends on the accuracy of the parameters chosen to represent the formation.

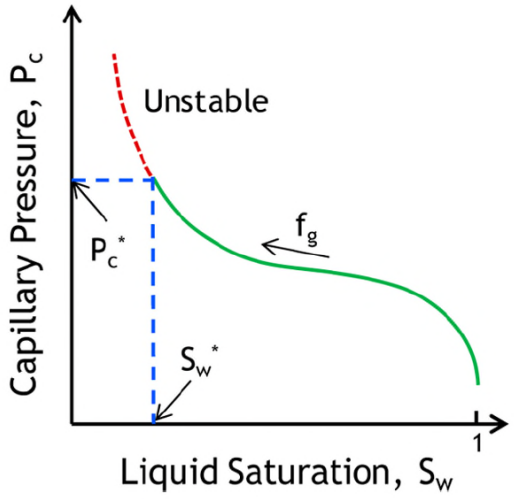

Figure 1.7 Schematic representation of the limiting capillary pressure and critical water saturation (Farajzadeh et al., 2015)

The foam scans presented in Figure 1.9 are based on laboratory results obtained with CO_2 foams (Khatib, Hirasaki and Falls, 1988) and presented by Farajzadeh et al.(2015), where the effects of a single foam formulation in cores with different permeabilities is presented. It is shown, that for a single foam formulation, apparent viscosity is larger in the high permeable media; this implies that mobility reduction is more efficient in high permeability media, and the effects of gas channeling due to heterogeneities can be overcame by using foams.

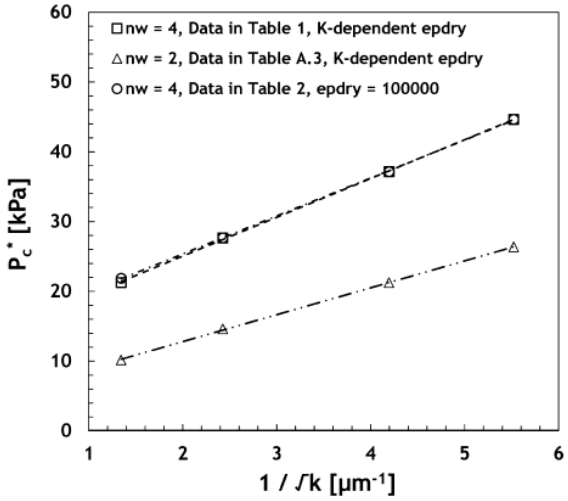

Figure 1.8 Relation between limiting capillary pressure and permeability (Farajzadeh et al. 2015)

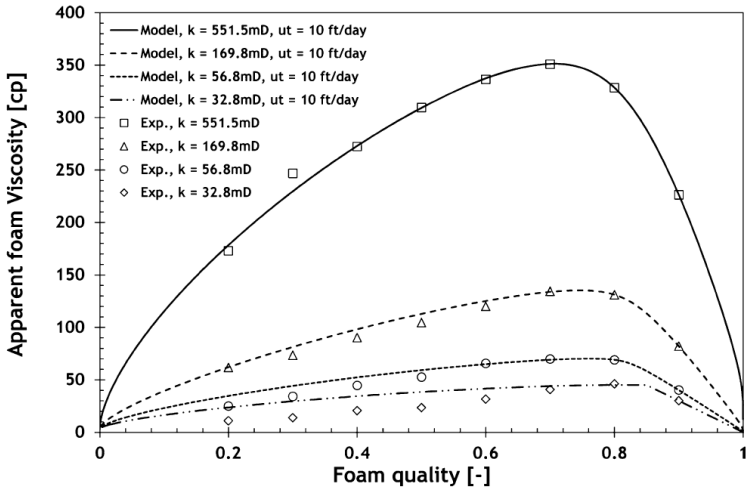

Figure 1.9 Effect of single foam formulation on different cores. (Farajzadeh et al. 2015)

1.2.4 Foam generation mechanisms

The mechanisms by which foams are created in porous media and the effects on apparent gas viscosity are of paramount importance in foam studies. Throughout literature there is a common agreement on three fundamental foam generation mechanisms: snap off, lamellae division and leave behind (Almajid and Kovscek, 2016).

The snap off sequence can be observed in Figure 1.10. Once a gas bubble overcomes the entry capillary pressure at the pore throat, a wetting phase collar is formed around the bubble (Figure 1.10a). As the bubble advances to the pore body, it encounters a lower capillary pressure at the front of the gas-water interface (Figure 1.10b). The capillary pressure difference causes the wetting phase to fallback growing the collar at the pore throat and snapping off the bubble (Figure 1.10c). This mechanism, known as snap off requires the pore body to be much larger than the pore throat.

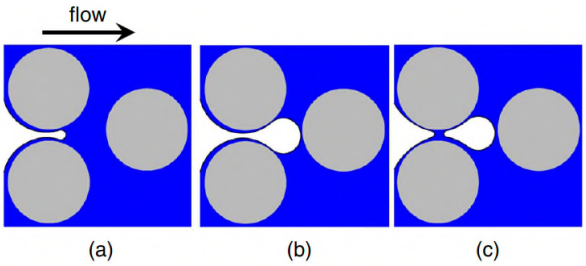

Figure 1.10 Snap off mechanism (adapted from (Almajid et al. 2016).

The second mechanism, Lamellae division, shown in Figure 1.11 occurs when a gas bubble is larger than the pore body and in regions where the main content in the pores surrounding the gas bubble is aqueous phase (Figure 1.11a). As the bubble reaches a branching point, the large bubble invades the surrounding pore throats and divides (Figure 1.11b).

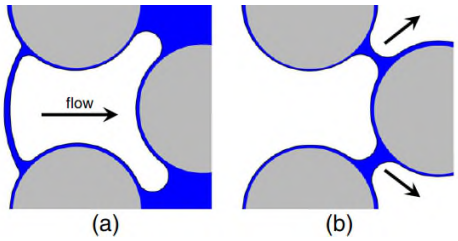

Figure 1.11 Lamellae division mechanism (Almajid et al. 2016).

The third mechanism, leave behind, shown in Figure 1.12, occurs when two bubbles approach a pore body (Figure 1.12a). As the bubbles converge downstream, a lens is formed in the pore body (Figure 1.12b).

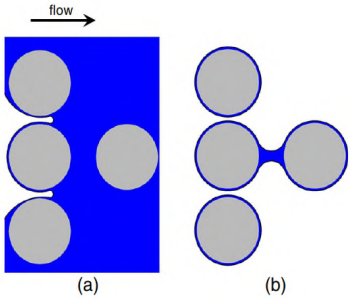

Figure 1.12 Leave behind Mechanism (Almajid et al. 2016).

1.2.5 Foam modelling

The effects of foam on reservoir rocks for EOR processes is widely studied, these studies, to a great extent, are limited to laboratories where core scale prevails. It is therefore important to find ways in which these observations can be upscaled to reservoir scale. One approach relies on creating models that mimic foam behavior, which can later be applied on simulators that will help understanding and predicting reservoir performance. Foam models are fundamentally divided in two main families ((Rossen, 2013), (Farajzadeh et al., 2015), (Lotfollahi et al., 2016)), one referred as population balance models, PB, and other referred as local equilibrium models or Implicit texture model, IT models.

PB models attempt to recreate processes of lamellae creation and destruction and treat foam texture explicitly (Lotfollahi et al., 2016), i.e. gas mobility is explicitly a function of foam texture (Rossen, 2013). The other group treats foam texture implicitly. This means that it takes the parameters that have incidence on foam texture and

reflects them in functions that alter gas mobility. The latter models are known as implicit texture foam models, IT models (Lotfollahi et al., 2016).

As mentioned in the previous sections, foam rheology is dependent on the capillary pressure in a way that it will collapse above the limiting capillary pressure or equivalently, below the critical water saturation. In PB models, critical water saturation and/or the limiting capillary pressure are explicitly treated as inputs and foam collapse occurs when either capillary pressure or water saturation approach their critical value (Lotfollahi et al. 2016). In contrast, in IT models, the limiting capillary pressure is introduced implicitly, by having foam collapse when foam dries out in the vicinity of the critical water saturation (Lotfollahi et al., 2016).

One important difference between the models, is how they deal with transient states, e.g. when foam is being created such as the injection boundary or shock front. Under transient conditions, only PB models can recreate the physics of the foam (Lotfollahi et al. 2016). However, once the transient process ceases and foam reaches local equilibrium, both models can describe foam performance. Different authors have found that in PB models, foam comes to local equilibrium fast (Rossen 2013, Lotfollahi et al. 2016, Al Ayesh et al. 2017).

For the purpose and objective of this project, the IT model known as STARS (Computer Modelling Group, 2010) will be described as it will be used during the simulations. The STARS foam model proposes that gas mobility is scaled by a factor *FM*. How this factor is estimated will be discussed further in this section. Nonetheless, its main attribute is that it gives foam a hypothetical minimum mobility that is increased when the physical parameters governing foam behavior such as water saturation, oil saturation, surfactant concentration, capillary number, salinity etc. are considered (Ma et al., 2013). Each physical parameter is represented by a semi-empirical function F_i that varies from 0 to 1. The relation between the STARS model and gas mobility is shown in Equation 1.2.6. and the scaling factor, *FM*, is defined in Equation 1.2.7.

$$\lambda_g^f = FM * \lambda_g \qquad \text{Equation 1.2.6}$$

$$FM = \frac{1}{1 + fmmob \prod_{i=1}^{6} F_i} \qquad \text{Equation 1.2.7}$$

The scaling factor for gas mobility, *FM*, is related to the parameter *fmmob* and the product of F_i functions. *fmmob* is related to foam strength and determines the minimum attainable foam mobility or equivalently, the maximum apparent viscosity if the product of F_i functions was 1. In the simulation part of this document, only the effects of the water saturation in the dryout semi-empirical function will be studied. The dryout function is defined as:

$$F_w = 0.5 + \frac{1}{\pi}\tan^{-1}(epdry(sw - fmdry)) \qquad \text{Equation 1.2.8}$$

In the F_w function the independent variable is water saturation. The other parameters: *fmdry* and *epdry* determine at which water saturation foam collapse starts occurring and how fast this transition happens respectively. Hence, *fmdry* is inherently related to the transition between high quality and low quality regime while *epdry* is related to the smoothness in the transition. Figure 1.13 shows the F_w, function for two cases where the same value of *fmdry* is used and *epdry* of 5000 in the light green curve and 138 in the blue curve.

From Figure 1.13 it can be suspected that *epdry* has a tremendous impact on foam performance near *fmdry*. Interestingly, it can be noted, that as *epdry* increases, F_w behaves as a step function that changes dramatically from 0 to 1 at *fmdry*. If a sufficiently large number of *epdry* is chosen, *fmdry* becomes the critical water saturation (Ma et al., 2013). The effect of the parameters controlling F_w are also illustrated by the arrows in Figure 1.13,

where *fmdry* displaces the curves horizontally and *epdry* makes the transition from 0 to 1 steeper with sharper edges.

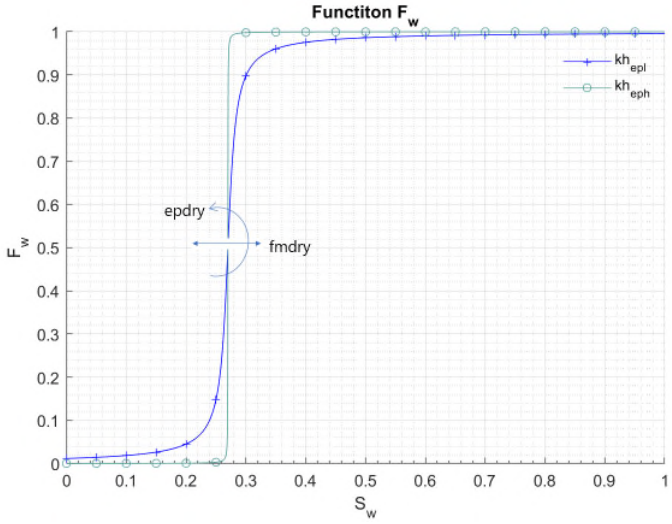

Figure 1.13 F_w function plotted for same *fmdry* and different *epdry* (5000 light green, 138 blue) .

Although important to see the effect of *epdry* and *fmdry* on the dryout function, the real interest lies in the effect the FM factor has on gas mobility. This is presented in Figure 1.14. The left image mimics foam performance in a porous media with permeability of 1500 mD and the right with 150 mD. The red line presents gas mobility without the effect of foam for comparison, the other two curves present the effect of *epdry* for the same *fmdry* value. The parameter *fmmob* is different in the left and right image and it has been changed to reflect the effect of permeability on foam strength. The square marker represents a water saturation of 0.2, which can be thought as the irreducible water saturation i.e. the minimum water saturation achievable and therefore pure gas injection. When the injection condition is pure gas, and the fluid upstream is surfactant the displacement can be compared to a SAG.

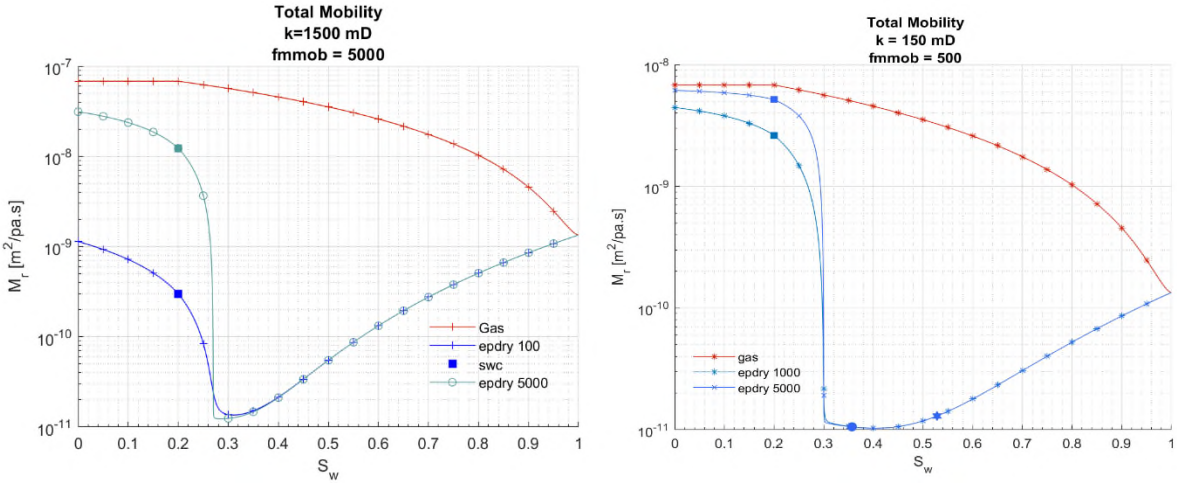

Figure 1.14 Effect of foam on mobility. Left: high perm layer. Right: low perm layer

The STARS model depends on the combination of different functions that represent the physics impacting foam rheology, hence, by just using the dryout function it is not mandatory to have foam collapse below the critical water saturation. The main objective of the dryout function is to show how foam performs while it undergoes dehydration, i.e. transitioning from wet foam to dry. Nonetheless, the dryout function can represent important

features of foams such as the transition between low quality and high quality regimes. To illustrate this point, a foam scan simulation using the STARS model with only the dryout function is presented in Figure 1.15.

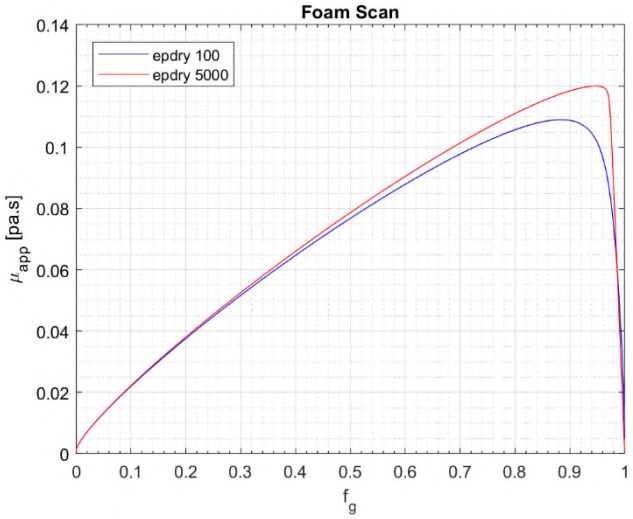

Figure 1.15 Foam quality scan for *k=1500 mD, fmdry=0.27, fmmob=5000*

2 Foam Simulation

This part of the project is dedicated to the analysis of the effects, that different combinations of parameters from the dryout function from the STARS model (Computer Modelling Group, 2010) have in foam flooding in heterogeneous reservoirs. In the past, studies such as the one performed by Zinati et. al, (2008) used stochastic bubble population modelling to asses foam performance in a heterogeneous reservoir and found that foam diversion increases recovery in the reservoir. In this study we intend to extend their findings by using an implicit texture model and expanding the observations to different injection qualities and varying the parameters that control foam strength.

To achieve this objective, different sets of parameters representing foams in different permeability porous media, will be simulated in a reservoir consisting of two identical layers 200m in length and 10m height with a permeability contrast of 10:1. Each layer will be discretized into 40 grids along the horizontal direction and 4 along the vertical, creating a reservoir with a mesh of 40 x 8 cells. The reservoir porosity will be fixed at 20% and the layers will have permeabilities of 1500 mD and 150 mD with an initial pressure of 2300 psi (158.6 Bar). In the reservoir, a well located at one end will inject foam at a constant rate of 400 ft^3/day (11.3 m^3/day) and another well located at the opposite end will produce with a constant wall face pressure of 2000 psi ($1.38x10^7$ Pa, 138 Bar). A schematic representation of the reservoir is presented in Figure 2.1. The simulations are conducted using a self-written implementation of the STARS model into the FVT toolbox simulator (Eftekhari, Schüller and Brosa Planella, 2015). During the simulation the effects of gravity and capillary pressure will be neglected. The first one will not be considered for the intention is to see only the effects of water saturation. The second one is neglected but treated implicitly through the critical water saturation as explained in section 1.2.5.

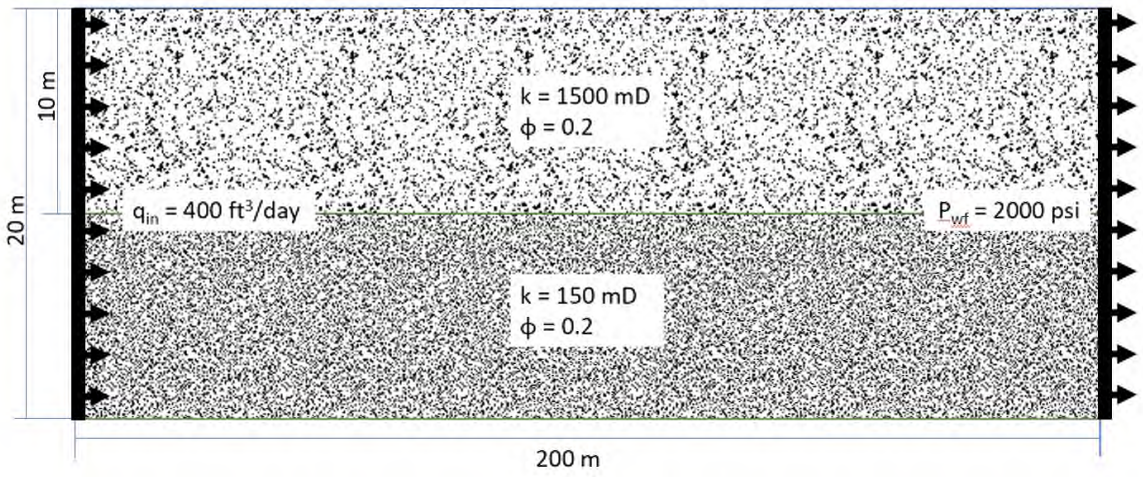

Figure 2.1. Schematic representation of reservoir

The injection method will be co-injection of surfactant solution and gas and it will be referred in terms of the gas fractional flow, f_g, also regarded as injection quality. The injection quality will be changed between simulations to analyze foam performance with varying injection conditions. One of the parameters considered to evaluate foam performance is *epdry,* whereby foam with a "low" *epdry* value will be compared against a foam with "high" value. The other parameter considered will be *fmmob* where different *fmmob* combinations will be used in two different cases. Since the STARS model will be used, it will be assumed that foam is instantaneously created at the injection boundary.

The first foam analysis will be done by forcing a no-communication condition between the high and low perm layers, the objective is to analyze the individual behavior of foam in each layer without interference of crossflow.

This step will be followed by allowing communication between layers, so that crossflow can occur and its impact on foam performance can be analyzed. Each of these two scenarios will be simulated with three different injection qualities and two *epdry* values. Finally, the effect of having a foam with high *fmmob* contrast between layers (116:1) will be analyzed, again comparing two different *epdry* values. The first two simulation scenarios, non-communicating layers and communicating layers, will be referred as case 1, while the scenario with high *fmmob* contrast will be referred as case 2. The parameters used in the STARS model (Computer Modelling Group, 2010) are shown in Table 2-2 and Table 2-3 for cases 1 and 2 respectively. The parameters are inspired by the findings of Farajzadeh et. al, (2015) where *fmmob* will be larger in high permeable media while *fmdry* will be higher in lower permeable media. Although their observations suggested that *epdry* decreases with increasing permeability, this parameter will be subjected to a sensitivity analysis, whereby low values will follow the trend observed by them and high values will be set to a higher value in an effort to force *fmdry* to be the critical water saturation.

The STARS model assumes that water relative mobility remains unaltered in the presence of foam while the gas relative mobility is scaled by the FM factor, to represent the relative permeabilities Brooks-Corey type relations will be used. The simulations will be done using water viscosity of 5.5e-4 [Pa.s] and gas viscosity of 2.23e-5 [Pa.s]. The time will be shown in pore volumes injected, which is referred as the dimensionless time. The physical parameters governing these relations are given in Table 2-1 .

Brooks-Corey relative permeability parameters	
swc	0.2
sgc	0
krw0	0.5
krg0	1
nw	3.4
ng	1.4

Table 2-1 Brooks-Corey Relative permeability parameters

Case 1 STARS Foam model Parameters				
	Low *epdry* case		High *epdry* case	
	Low perm Layer	High perm Layer	Low perm Layer	High perm Layer
k [D]	0.15	1.5	0.15	1.5
phi	0.2	0.2	0.2	0.2
fmmob	500	5000	500	5000
epdry	1000	100	5000	5000
fmdry	0.3	0.27	0.3	0.27

Table 2-2 STARS foam model parameters for case 1

Case 2 STARS Foam model Parameters				
	Low *epdry* case		High *epdry* case	
	Low perm Layer	High perm Layer	Low perm Layer	High perm Layer
k [D]	0.15	1.5	0.15	1.5
phi	0.2	0.2	0.2	0.2
fmmob	1720	199450	1720	199450
epdry	139	138	5000	5000
fmdry	0.35	0.28	0.35	0.28

Table 2-3 STARS foam model parameters for case 2

Foam's ability to reduce mobility is indicated by the apparent viscosity. One way to present the apparent viscosity is through foam quality scans, that show the steady state rheology of foam for different injection qualities (Figure 1.15). However, when foam scans are presented in this way, the effect of water saturation is not shown explicitly. During the simulations, the grid cells will undergo water saturation transition from the initial condition to the injection condition, hence, to ease the understanding the foam flood, the apparent viscosity will be presented in

a similar way to foam scans, but with water saturation in the horizontal axis. This type of representation is shown in Figure 2.2 and Figure 2.3, where the apparent viscosities are modelled according to the parameters given in Table 2-2 and Table 2-3.

The apparent viscosities figures have markers that indicate water saturation at the injection face for the three different injection qualities simulated. The square corresponds to $f_g=1$, the circle to $f_g=0.95$ and the hexagon to $f_g=0.50$. In both simulation cases (CASE 1 and CASE 2), the simulated qualities are intended to show simulations in the low and high quality regimes as well as pure gas injection (Figure 2.2 and Figure 2.3).

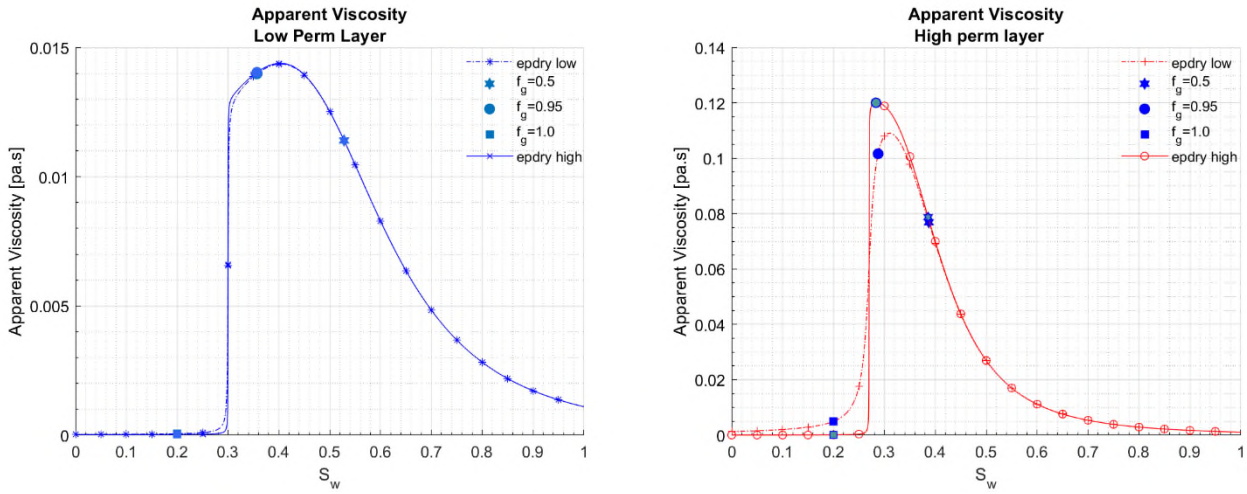

Figure 2.2. Apparent viscosity vs. water saturation for case 1. Left: LPL. Right: HPL

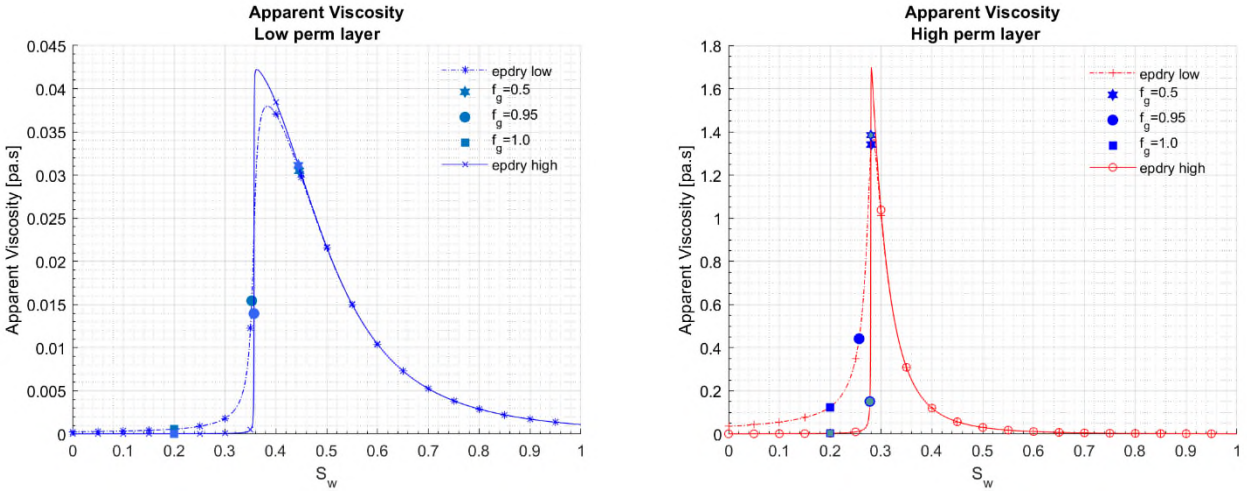

Figure 2.3 Apparent viscosity vs. water saturation for case 2. Left: LPL. Right: HPL

In the subsequent sections of the chapter, the results from the simulations will be analyzed. As previously stated, the first analysis will be done for case 1 with non- communicating layers, followed by case 1 with communicating layers and finally case 2 with non communicating layers.

2.1 Non-communicating layers simulation case

One of the aims of foaming gas is to improve the sweep efficiency, hence, its effect should be reflected in the recovery factor, RF. The RF for the low permeability layer (LPL), high permeability layer (HPL) and total reservoir RF after injection 1 PV while disallowing communication between the layers are shown in Figure 2.4. One of the main observations is that the RF increases in both layers as the injection quality is increased, even when injection pure gas (f_g=1). The total RF in the HPL (Figure 2.4 right) is higher for all injection qualities and reaches a maximum of 73% compared to maximum recovery of 69% in the LPL (Figure 2.4 left).

At 50% injection quality, the effect of *epdry* in the RF is negligible and reaches 50% in the HPL compared to 47% in the LPL. As quality increases in the HPL, the effect of high *epdry* on the RF becomes more noticeable. Figure 2.4 right shows that higher *epdry* acts in both ways, improving and worsening the total RF in the HPL whereas in the LPL the RF remains unchanged. At f_g=1 the RF in the HPL is reduced from 74% in the low *epdry* case to 73% in high *epdry* case. Conversely, at f_g=0.95 the RF is improved by approximately 0.5% with high *epdry*. This indicates that the effect of *epdry* depends on the injection quality. Nonetheless, with the simulated foam parameters the differences in recoveries are rather marginal.

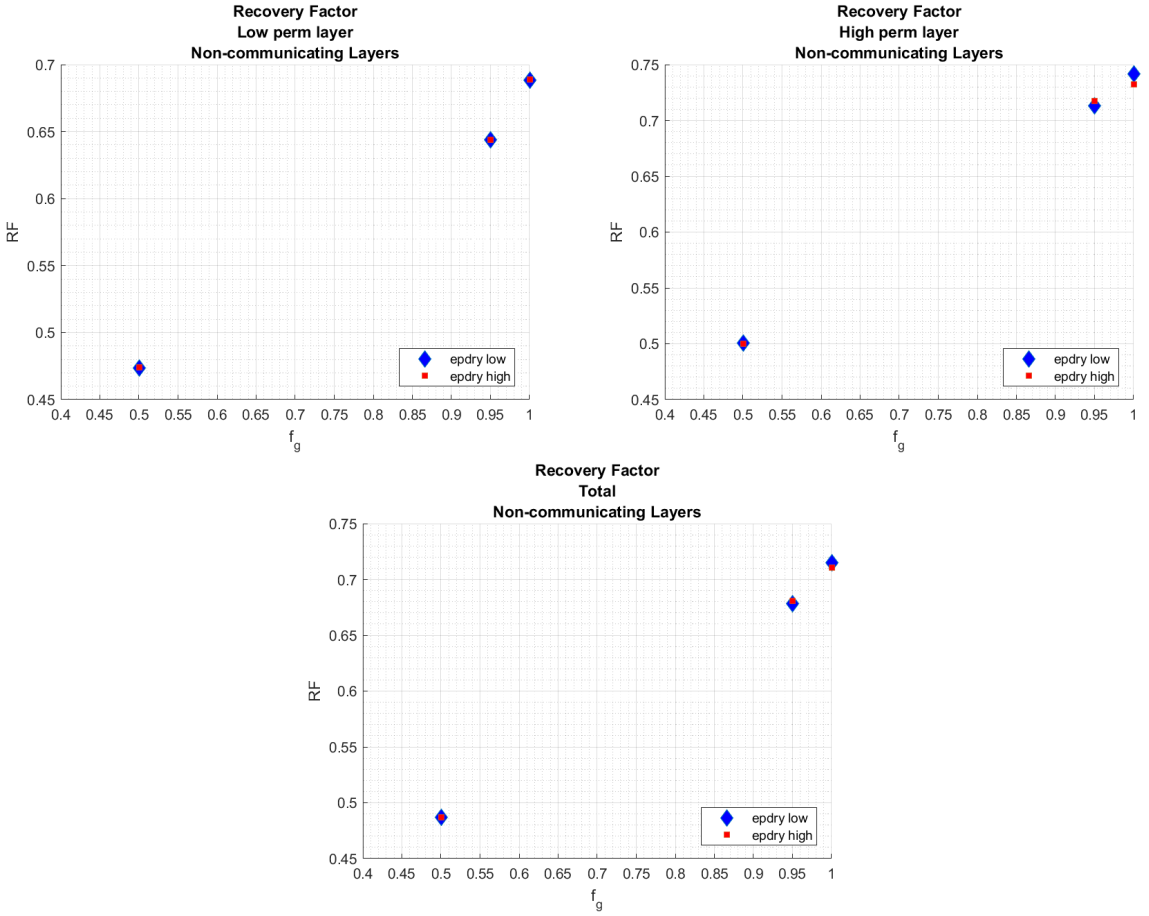

Figure 2.4. Recovery factor for non-communicating layers as function of injection quality. Top left: LPL. Top Right: HPL. Bottom: Total reservoir recovery factor

To illustrate these differences better, the production profile as injection progresses in time is shown in Figure 2.5. As noted, the RF does not exhibit sensitivity to *epdry* in the LPL as opposed to the HPL layer. In both layers the slopes of the RF line prior BT are 0.50 for *50%* injection quality, 0.95 for 95% injection quality and 1.0 for 100% injection quality. Hence, the differences in ultimate RF can be only attributed to different BT times and the additional recovery after BT. At 100% injection quality, in the HPL, the differences between high and low *epdry* are mainly caused by an earlier BT in the high *epdry* case (diamond markers in Figure 2.5 right) that can be

attributed to the weaker foam at 100%. Conversely, at *95%* injection quality the difference, although related to BT, is attributed to a stronger foam at 95% high .

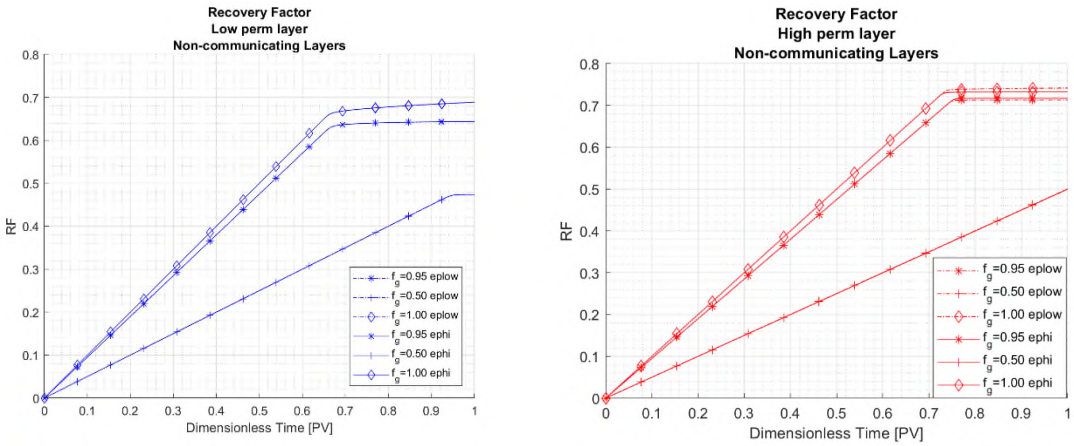

Figure 2.5. Production profile for non-communicating layers as function of time. Left: low perm layer. Right: High perm layer

The shape of the production profiles in Figure 2.5 can be better understood with the saturation profiles, which are shown in Figure 2.6. At 50% injection quality in both layers, the position of the foam fronts for the different injection volumes (dimensionless time) indicate that no BT has occurred after injection 1PV. Interestingly, the saturation plots show the effect of foam mobility reduction, whereby foam fronts moves faster in the LPL indicating that foam is less movable in the HPL.

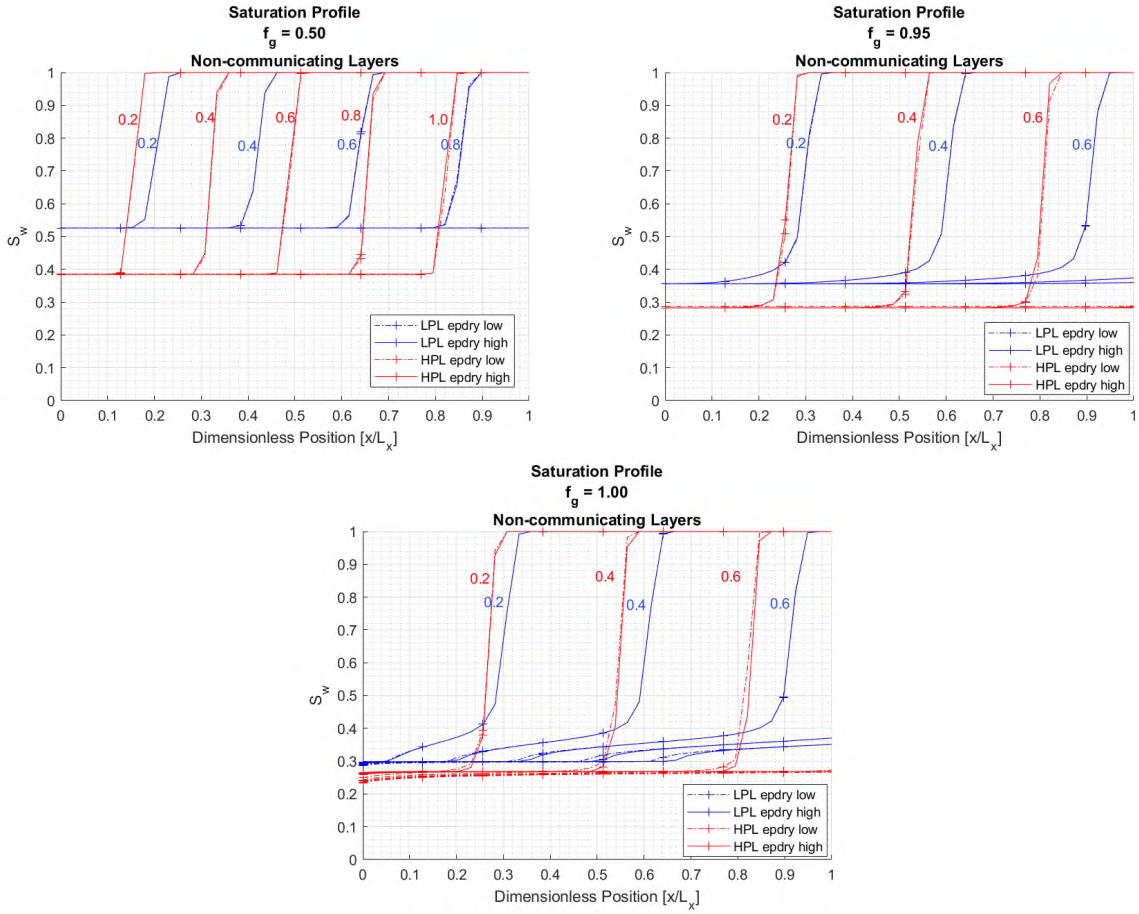

Figure 2.6 Saturation Profile for non-communicating layers as function of position at different dimensionless times. Top left: fg=0.50. Top right: fg=0.95. Bottom: fg=1.00

Another important feature that can be noted from the saturation profiles is how desaturation occurs. For the 50% and 95% injection qualities in the HPL layer (red lines Figure 2.6 right and left), once the front passes the desaturation is efficient, and the remnant water saturation is close to the injection face water, although in the LPL at 95% injection quality spreading waves behind the foam front can be seen, indicating additional recoveries after BT.

In pure gas injection (Figure 2.6 bottom) the desaturation behind the shock remains higher than the injection face water saturation (swc, 0.2) in both layers. Nonetheless, in the LPL the water saturation behind the shock is at nearly 0.4 and reduces further upstream to *fmdry*, where the desaturation seems to stagnate slightly below *fmdry (0.3)* for both *epdry* values. In contrast, the HPL desaturates behind the shock immediate to a value slightly below *fmdry* (0.28), though *epdry* has two effects. With high *epdry* saturation stagnates slightly below fmdry (0.28) while in low epdry it keeps decreasing below fmdry, though slowly. This behavior suggests that desaturation below *fmdry* is delayed as the *epdry* value is increased.

Foams work by trapping gas and therefore reducing its mobility, the extent to which mobility is reduced is indicated by the foam apparent viscosity where higher values indicate stronger foams. Figure 2.8 and Figure 2.7 show the apparent viscosities in the HPL and LPL for different dimensionless times and injection qualities. Interestingly, the effect of *epdry* becomes more noticeable in the apparent viscosity profiles. In the HPL, the high *epdry* simulation creates a stronger foam than *epdry* low, as shown by the larger peak in the continuous redlines in Figure 2.8. In general, apparent viscosity in the HPL becomes larger with high *epdry* and increases with the injection quality. In contrast, the LPL viscosity profiles show insensitivity to *epdry* in terms of foam strength but show that the maximum value is achieve in the high quality regime. However, observable differences attributed to *epdry* in the LPL are perceived in the abruptness of foam dryout.

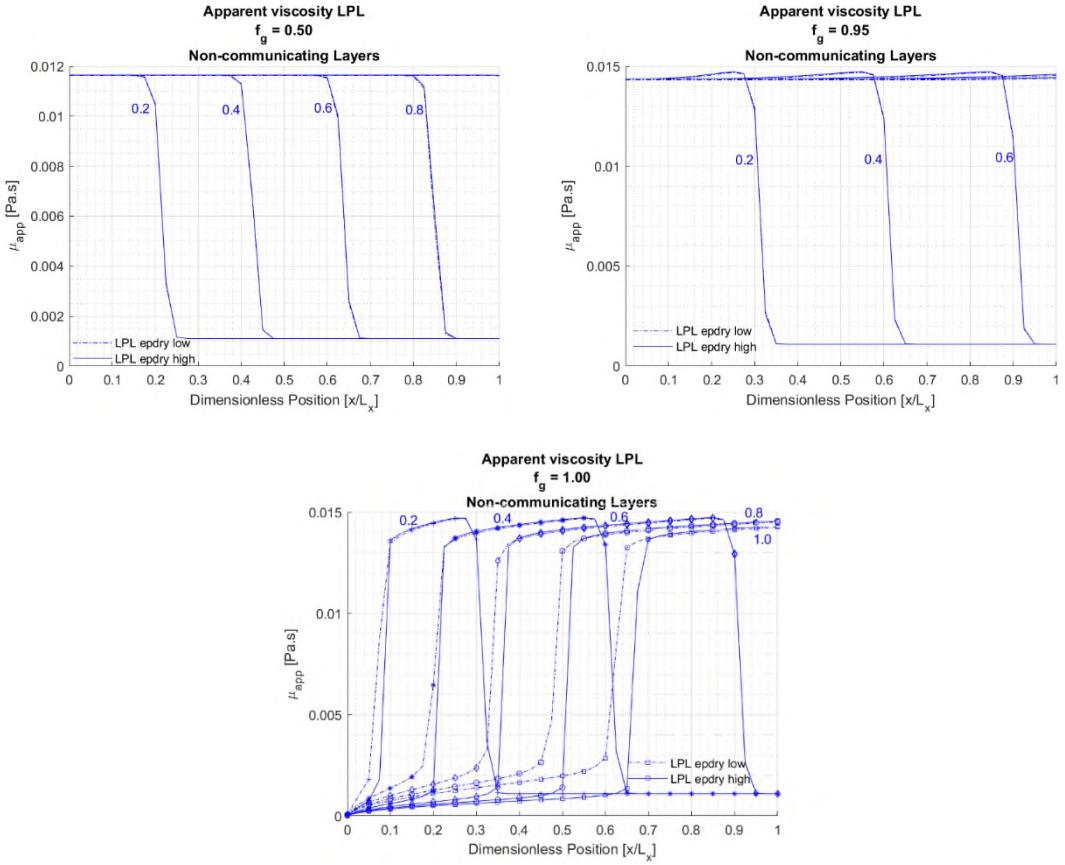

Figure 2.7 Foam apparent viscosity in LPL for non-communicating layers as function of position at different dimensionless times. Left: fg =0.50. Right: fg=0.95. Bottom: fg=1.0

At 50% and 95% injection qualities in both layers (Figure 2.8 and Figure 2.7 right and left), the apparent viscosity behind the shock remains close to the maximum attainable value (as per the foam scan Figure 2.2), though with differences in shape behind the foam front attributed to quality regime. At 100% injection quality it is evident that foam is exposed to a wide range of foam apparent viscosities, from maximum apparent viscosity behind at foam front to a minimum value close to the injection face.

One of the interesting attributes of the apparent viscosity profiles is that they clearly show the effect of quality regime. In the low quality regime, the apparent viscosity at the shock and behind it is constant and its value depends on the foam strength for the injection quality. A slightly different behavior is observed in the high quality regime above *fmdry*, where a peak in apparent viscosity at the shock is seen, followed (upstream) by a small decrease in apparent viscosity due to foam collapse (light collapse as saturation is higher than *fmdry*).

At 100% injection quality in the LPL (Figure 2.7 bottom), the high quality regime peak is observed behind the foam front, however the interesting feature is that layer is filled with saturations (belonging to the spreading waves behind the shock) that are greater than *fmdry* and therefore filling a great portion of the layer with foam strong foam. This foam remains strong until saturation approaches *fmdry* (0.3) when it collapses abruptly. Interestingly, the way in which collapse occurs is one of the few differences attributed to *epdry* in the LPL, whereby larger *epdry* creates a more abrupt collapse. Furthermore, with the collapse profiles, it can be seen that spreading waves with water saturation above *fmdry* move slightly faster in high *epdry* than in low *epdry*.

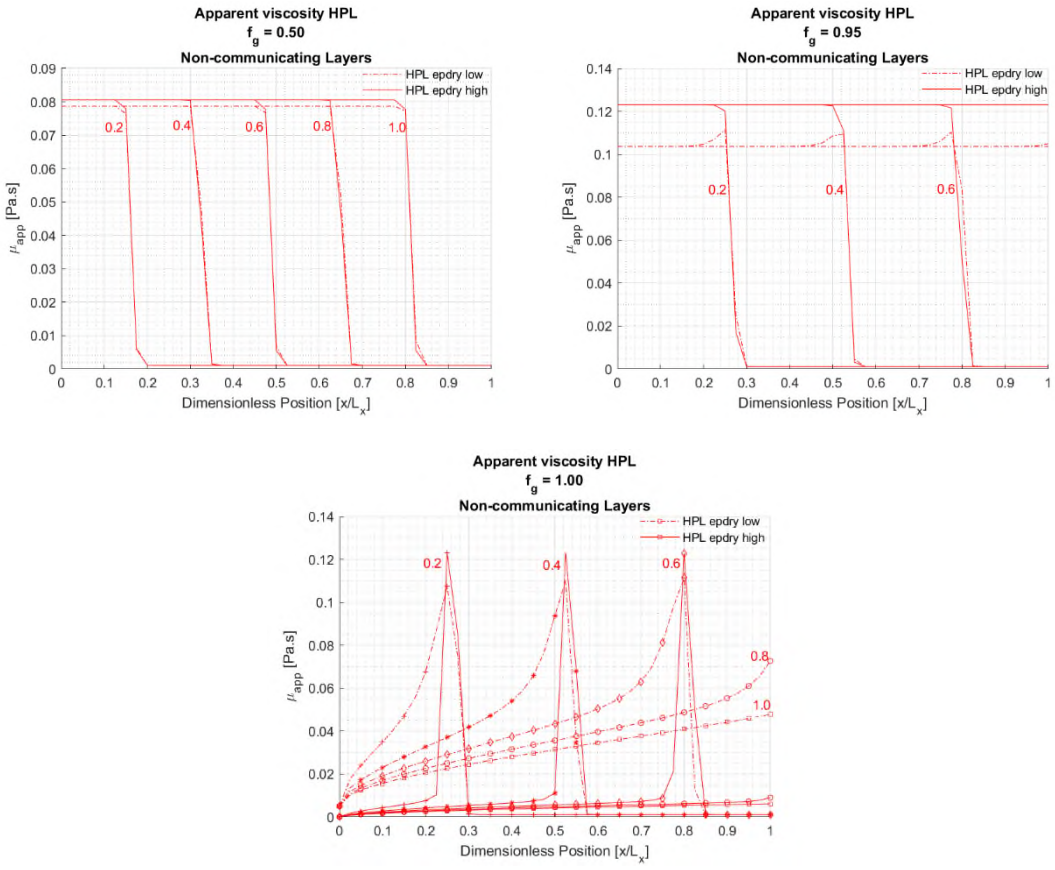

Figure 2.8 Foam apparent viscosity in HPL for non-communicating layers as function of position at different dimensionless times. Left: fg =0.50. Right: fg=0.95. Bottom: fg=1.0

Apparent viscosity behavior in the HPL (Figure 2.8), is similar to that of the LPL, nonetheless the values are significantly higher and the effect of *epdry* is more pronounced. At 50% injection quality (low quality regime) apparent viscosity remains constant behind the for both *epdry* values although higher in magnitude in high *epdry* due to larger foam strength.

At 95% injection quality, the effect of being just at the quality regime transition and in the high quality regime is revealed. At the transition saturation, occurring at 95% quality in high *epdry*, the behavior is similar to the low quality regime behavior, whereby foam apparent viscosity is constant behind the foam front, nonetheless at foam's maximum apparent viscosity. Similarly, for low *epdry,* apparent viscosity immediately behind the shock is at the foam's peak value followed upstream by a small reduction due to foam collapse, indicative of high quality regime.

At 100% injection quality in the HPL (Figure 2.8 bottom), water saturations upstream the shock are below *fmdry* (0.27), hence foam calescence is seen. However, while foam collapse is smooth in the low *epdry* case, indicated by a smooth reduction in apparent viscosity from the maximum value to the injection face (dashed lines Figure 2.8 bottom), foam collapse in the high *epdry* is marked by an abrupt change nearly 10 fold (continuous lines Figure 2.8 bottom), this shows that in the high quality regime when saturation fall below *fmdry*, *epdry* plays a paramount role in how dryout occurs.

Foam apparent viscosity is indicative of how large the pressure drop will be in the layer; however, it also depends also on the layer's permeability and the content of foam in the layer. The combined effects can be seen in the LPL and HPL pressure profiles shown in Figure 2.9 and Figure 2.10 respectively.

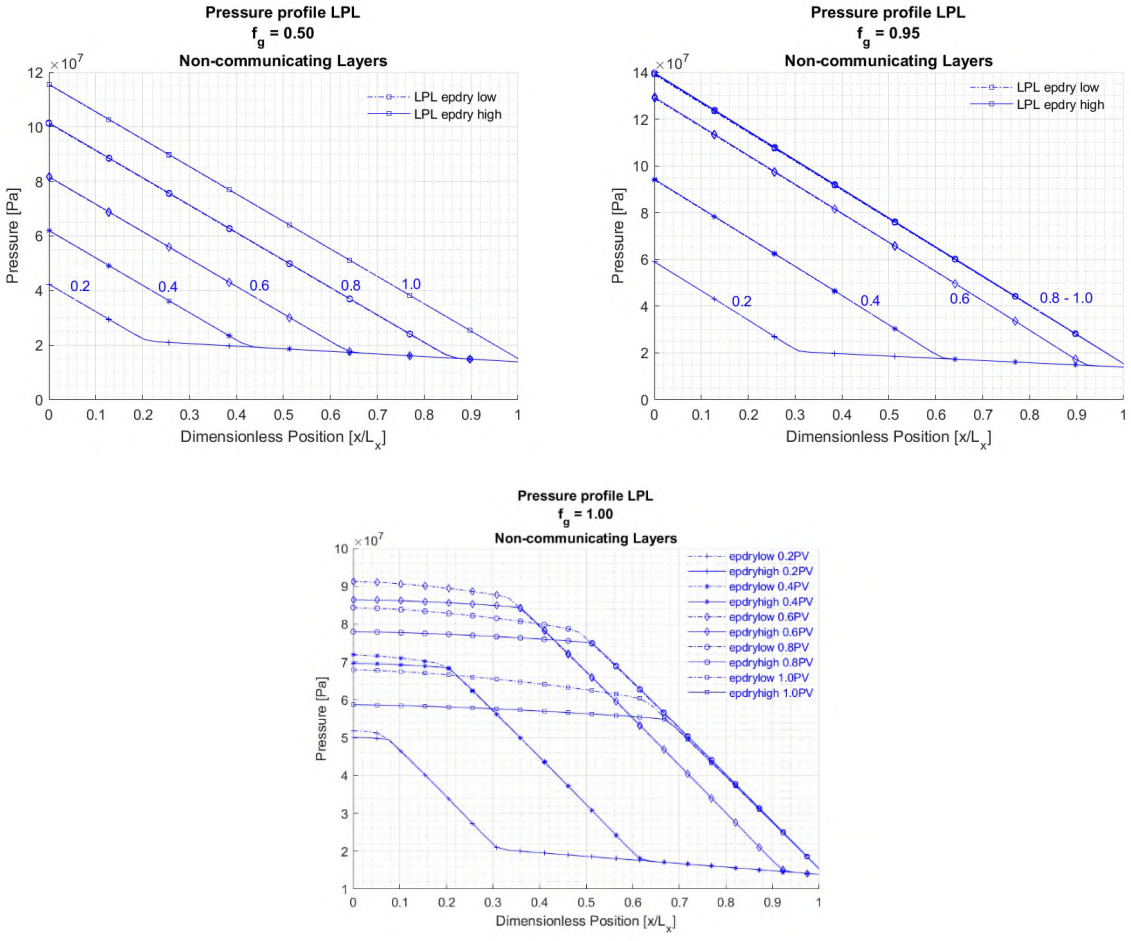

Figure 2.9 Pressure profile in LPL for non-communicating layers as function of position. Left: fg =0.50. Right: fg=0.95. Bottom: fg=1.0

At 50% in the LPL (Figure 2.9 left), the pressure increases as the reservoir gets flooded with foam and mobility is reduced. The pressure increase over the 1.0 PV foam injection is nearly 7 fold. A similar pressure pattern is observed in the LPL at 95% injection quality (Figure 2.9 right), but unlike in 50% quality where pressure rises at all displayed times, at 95% there is a slightly decrease in pressure of 200KPa (2 Bar) between 0.8 PV and 1.0 PV caused

by foam collapse after BT; yet, these variations are almost imperceptible but ascertain the high quality regime behavior. The patterns are straight lines attributed to constant apparent viscosity behind the shock.

The influence of *epdry* in pressure in the LPL at 50% and 95% injection quality is negligible, however, bigger differences can be seen at 100% injection quality. At this condition, the pressure profile isn't a straight line from the shock to the injection face. In contrast, it shows that, close to the injection face where foam is weak, pressure drop is rather soft and, in the places, where strong foam is present the pressure gradient increases. Moreover, the small delay in foam dryout as well as it smoother dryout creates larger pressure gradients at injection face.

Unlike the LPL, where pressure differences due to *epdry* are only seen at 100% injection quality, the HPL pressure response exhibits sensitivity to this parameter at all the simulated injection qualities. The extent upon which results differ can be seen in Figure 2.10, where it can be noticed that they become larger with increasing injection quality and as injection progresses.

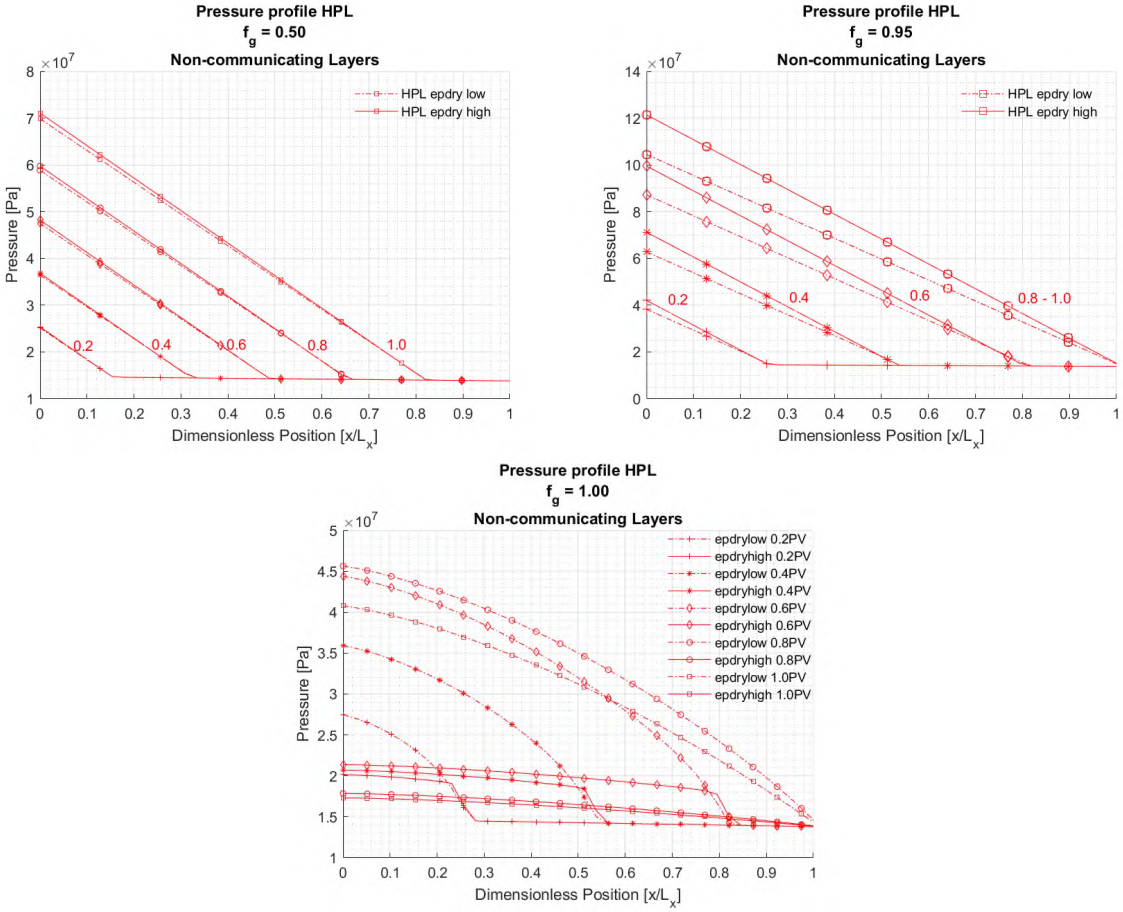

Figure 2.10 Pressure profile in HPL for non-communicating layers as function of position. Left: fg =0.50. Right: fg=0.95. Bottom: fg=1.0

At 50% injection quality in the HPL, the weaker foam with lower *epdry* results in lower pressures within the layer. Nonetheless, since foam strength does not vary significantly at this injection quality, the pressure differences between low and high *epdry* are small and max only to 1.22MPa (12Bar) at the injection face at 1PV. Likewise, at 95% injection quality, pressure increases as time progresses and foam fills the layer. However, due to the more pronounced differences in foam strength, the differences between the pressure profiles from low and high *epdry* are larger and at 0.8-1.0 PV the pressure difference reaches 170Bar.

At 100% injection quality (Figure 2.10 bottom), the pressure profiles for the two *epdry* values appear remarkably different at their equivalent injection volumes. The high *epdry* profiles (continuous lines Figure 2.10 bottom) show a pattern resembling its counterpart in the LPL. It is evident that the collapsed foam behind the front creates small

pressure gradients, and the only significant pressure increase occurs at the foam front where apparent viscosity is at its maximum value. In the low *epdry* case, the smooth foam dryout creates a pressure drop that is significantly larger than the high *epdry*, nonetheless since apparent viscosity is not constant the profile becomes curved with smaller gradients as the foam strength is reduced.

In conclusion, foam behavior in both layers is comparable if water saturation is above *fmdry*, though numerical differences are marked in pressure and viscosities. At *100*% injection quality considerable differences in foam performance between the layers is observed, and in HPL even substantial differences between low and high *epdry* occur.

The saturation profiles show distinguishable features between the low quality and high quality regimes that ultimately causes differences in RF, viscosity and pressure profiles. In the low quality regime water saturation behind the shock is homogeneous, with a remnant water saturation equal to the injection face water saturation, hence, with constant apparent viscosity.

In the high quality regime above *fmdry*, a peak in apparent viscosity behind the shock is seen and is caused by the higher water saturation behind the shock as compared to the injection face water saturation, this peak vanishes upstream as water saturation is reduced, and foam collapse starts occurring. When water saturation falls below *fmdry* (high quality regime) foam collapses severely and the peak is amplified. The collapse behavior is governed by the sharpness of the transition at *fmdry* which is given by *epdry*.

In the HPL, the higher contrast between high *epdry* and low *epdry* (50:1) marks noticeable differences in foam strength, in which high *epdry* creates a stronger foam with a more abrupt foam collapse in the high quality regime. This implies that in the low quality regime high *epdry* yields to larger recoveries and in the high quality regime as saturation approaches *fmdry* the recovery efficiency is reduced, and better recoveries occur with low *epdry*.

The parameters chosen to model the foams reduce mobility in the HPL such that foam moves faster in the LPL. Due to the higher speed, pressure regimes in the LPL are significantly greater than in the HPL, suggesting that in terms of pressure drop, permeability's impact is larger than mobility reduction. In terms of velocity, faster foam fronts imply lower apparent viscosities. The different velocities between the layers create different pressure regimes that create vertical pressure differences that will cause crossflow between the layers if communication is allowed.

2.2 Communicating layers simulation case

With non-communicating layers, NCL, it is reasonable to assume that pressure gradient occurs in the horizontal direction due to homogeneity within the layer, therefore fluid movement occurs only horizontally. But as shown by the pressure plots in NCL (Figure 2.9 and Figure 2.10), the LPL is subjected to larger pressure regimes creating a vertical pressure gradient that will cause crossflow between the layers. In this section the extent to how this pressure gradient impacts foam performance will be explored .

Figure 2.11 shows the juxtaposition of the pressure profiles from the LPL and HPL with communicating layers, CL. On the left and right columns, the low and high *epdry* cases are shown, while the rows show the different injection qualities. These profiles show that the pressure patterns along the reservoir don't vary much when compared to NCL i.e. the position of maximum pressure, the dimensionless time at which it occurs, and how pressure drops from the injection face to the production face. Moreover, CL follows the observed trend in NCL of increasing injection face pressure from 50% to 95% injection qualities and decreasing at 100%. However, as shown by the overlaying pressure profiles in Figure 2.11, communication tends to equate the pressure between layers though diversion that occurs in places where vertical pressure gradients occur, which are in the vicinities of the injection

face and shock front. At the scales shown in Figure 2.11 the differences are difficult to spot, therefore the vertical pressure difference between layers is presented in Figure 2.12 to facilitate examination of crossflow.

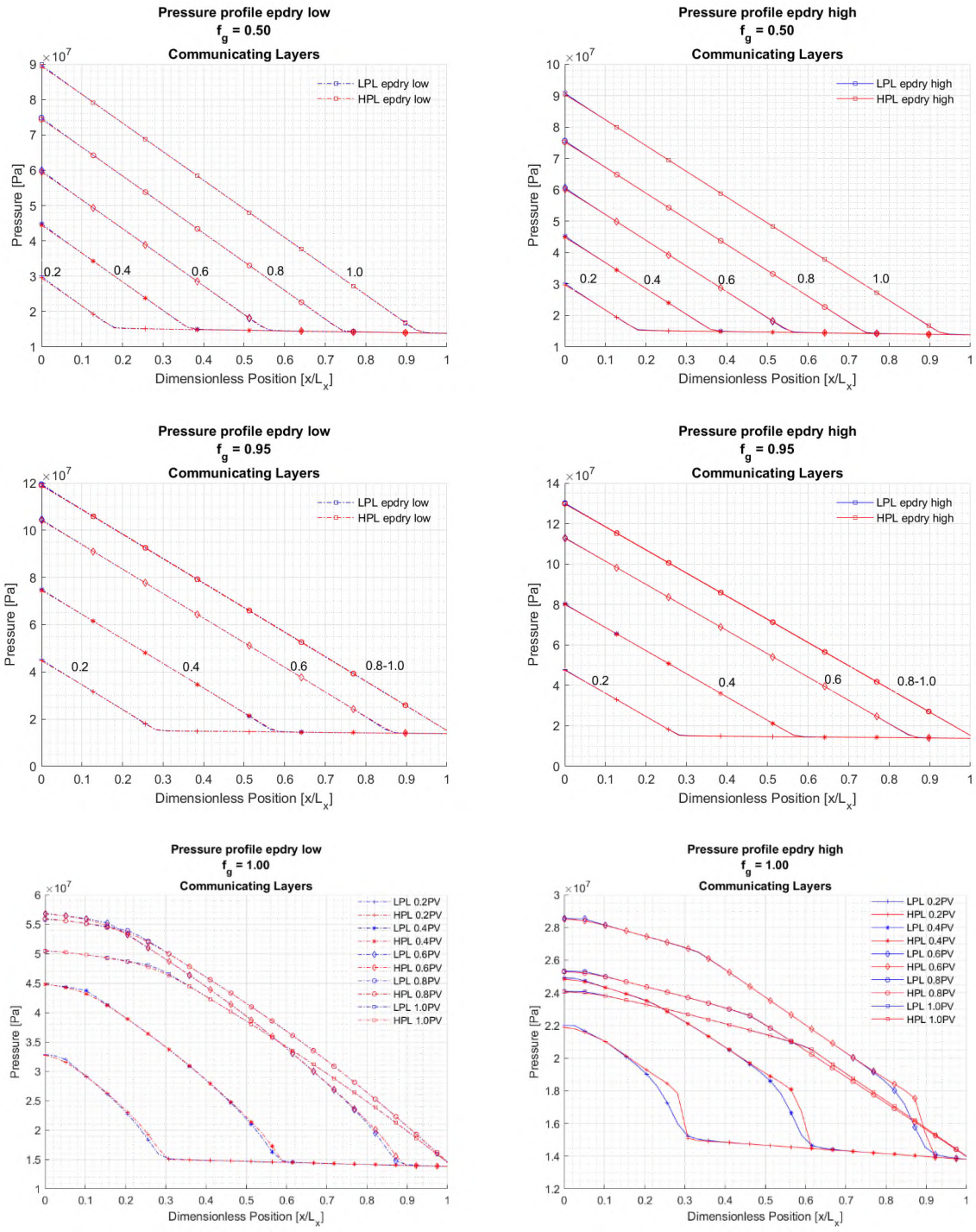

Figure 2.11 Pressure profiles for communicating layers. Top left: fg=.50 *epdry* low. Top right fg=.50 *epdry* high. Middle left: fg=.95 *epdry* low. Middle right: fg=.95 *epdry* high. Bottom left: fg=1.0 *epdry* low. Bottom right: fg=1.0 *epdry* high

In terms of *epdry*, at 50% injection quality, relative differences related to *epdry* are as small as 1.3% at the injection face, with high *epdry* having larger pressure regimes, while at 100% injection quality differences can be as large as 120% with low *epdry* having larger pressure regimes. This indicates one of the effects of larger *epdry* values on pressure: first, increasing pressure differences as injection quality increases in the low quality regime (high *epdry* having larger pressure regimes) and second, a sharp inversion in the profile in the high quality regime when saturations fall below *fmdry* and foam dries out (low *epdry* values having higher pressure regimes). The relative

differences of high to low *epdry* pressure profiles for each of the injection qualities and layers can be seen in Appendix B- i.

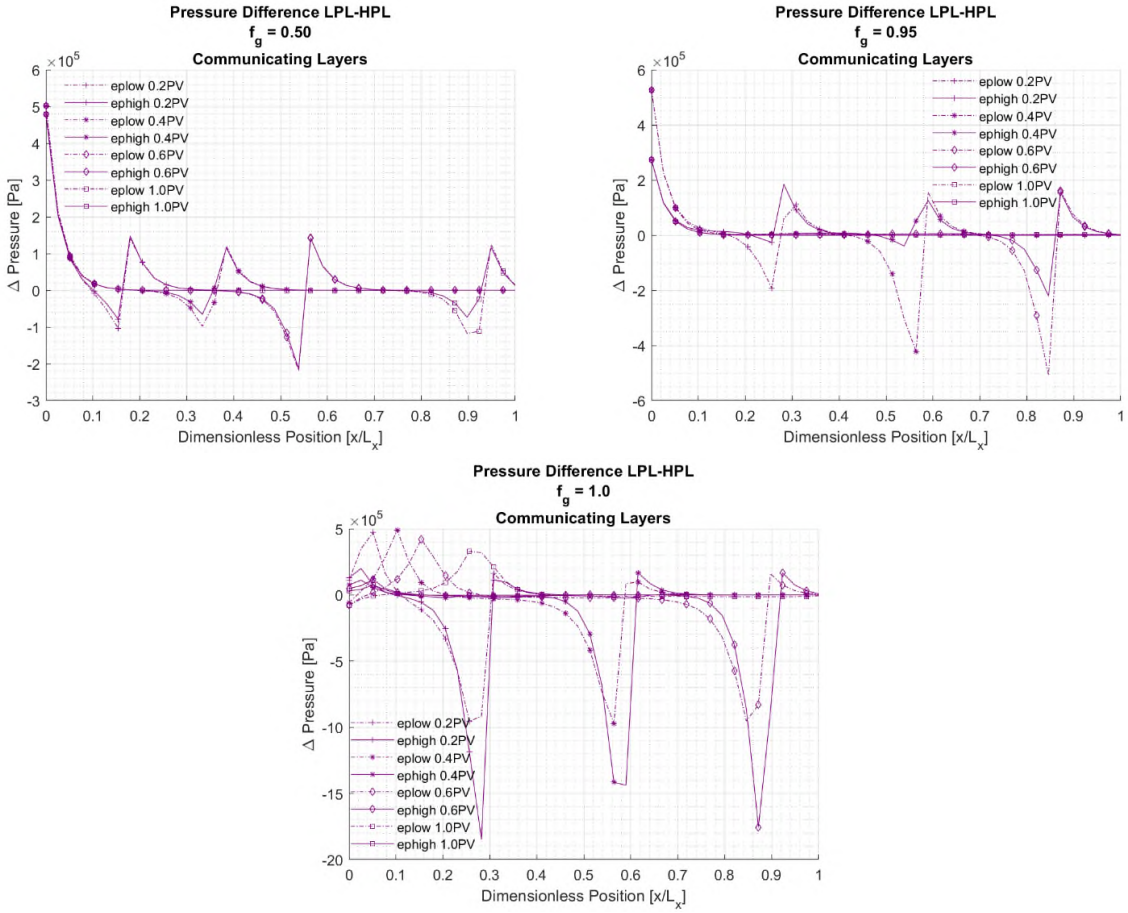

Figure 2.12 Pressure difference between HPL and LPL (communicating layers) for different injection qualities and injected volumes. Left: fg=0.51.Right: 0.95. Bottom: 1.0

Crossflow is expected to occur in places where pressure gradients exists, Figure 2.12 allows to precisely capture the places by showing the pressure difference between LPL and HPL. In the figure it can be seen that for all qualities and both *epdry* values there are three distinctive segments. First, a segment where pressure is higher in the LPL, followed downstream by a segment where pressure is higher in the HPL and third a segment where the initial behavior is replicated in a smaller scale. The pressure difference indicates the direction of the crossflow and it shows that it occurs in both directions, from LPL to HPL and from HPL to LPL.

At 50% injection quality diversion behaves similar for both *epdry* cases. At 95% and 100% injection qualities it shows that the weaker foam, low *epdry* for 95% and high *epdry* for 100%, create larger pressure differences. Using the pressure gradient between adjacent grid cells and Darcy's law, the total velocity can be obtained. Figure 2.13 shows the extent of diversion occurring between layers. The comparison is made for both *epdry* values and a hypothetical case where gas is not foamed. The plots are shown for 0.4 PV as an example since the patterns are repeated prior BT.

Figure 2.13 vindicates the fact the diversion occurs at the places with vertical pressure gradient and more important, it allows to see the amount of flow each layer is undertaking. The main observation is that at 50% and 95% injection quality, there are noticeable differences between foamed gas and pure gas (no surfactant), whereby if gas is not foamed more than 90% if the flow goes through the HPL as opposed to foam injection where the fraction is reduced. Similarly, at 100% injection quality most of the flow occurs through the HPL, although the difference between foamed gas and un-foamed is significantly smaller than at 50% and 95%.

At 50% injection quality diversion occurs close to the injection face and most of the flow occurs though this layer. Behind the shock nearly 60% of the flow occurs through the HPL whereas in front of the shock the fraction is nearly 90%, indicating that water ahead of the foam front in the LPL flows through the HPL. There are no significant differences between both *epdry* cases.

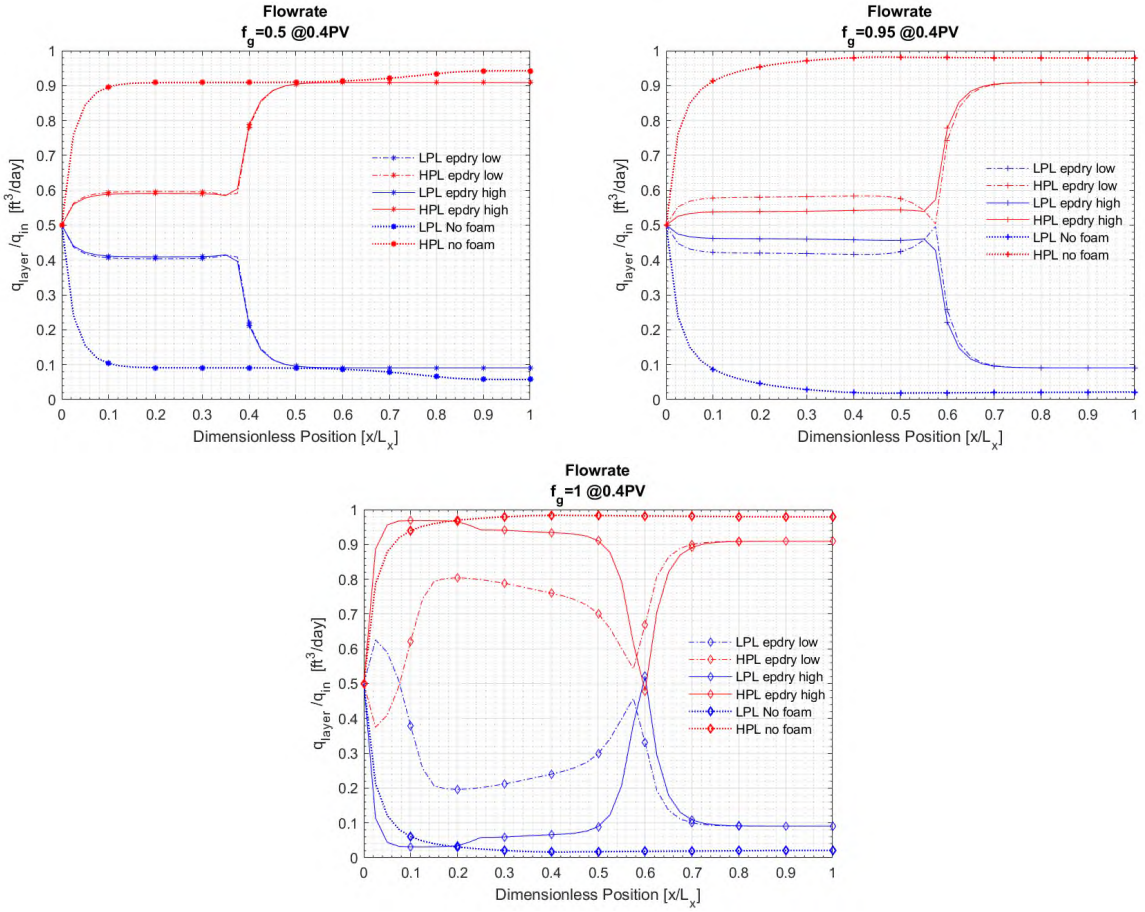

Figure 2.13 Flowrate fraction through HPL and LPL at 0.4PV (communicating layers) for different injection qualities. Left: fg=0.50. Right: fg=0.95. Bottom fg=1.0

At 95% injection quality a similar behavior is seen, whereby foam is diverted from the LPL to the HPL close the injection face, nonetheless is a smaller proportion than 50% injection quality. In addition to lower foam diversion, it can also be seen that behind the foam front in low *epdry* foam is being diverted from the HPL to the LPL. Again, ahead of the foam front it can be seen that most of the flow occurs through the HPL, indicating also that water is being diverted from LPL to HPL as it flows easier through this layer.

At 100% injection quality, close to the injection face, a different pattern is observed in the low *epdry* case (dashed lines Figure 2.13 bottom), where foam is being diverted from the HPL to the LPL, nonetheless the effect is reversed further downstream, and foam is diverted from the LPL to the HPL. Afterwards, it follows the same patters observed before where foam is diverted from the HPL to the LPL behind the shock. The 100% injection quality high *epdry* exhibits a behavior in which two segments can be observed, foam diversion from the LPL to HPL close to the injection face and from the HPL and to the LPL behind the foam front (continuous lines Figure 2.14 bottom). This can be caused by the peak apparent viscosity behind the foam front in the HPL that finds less restriction by diverting to the LPL than increasing its apparent viscosity (the apparent viscosity profiles can be seen in Appendix B ii)

In terms of quality regime, in the low quality regime and transition (50% injection quality and 95% injection quality high *epdry*), foam diversion only occurs close to the injection face. Conversely, foam diversion from the HPL to the LPL occurs behind the shock in the high quality regime 95% low *epdry* and 100% injection quality. This behavior suggests a dependence on quality regime in regard to foam diversion from the HPL to the LPL. However, the ability to of a phase to flow through the layer ultimately depends on the mobility (ratio of absolute permeability and apparent viscosity).

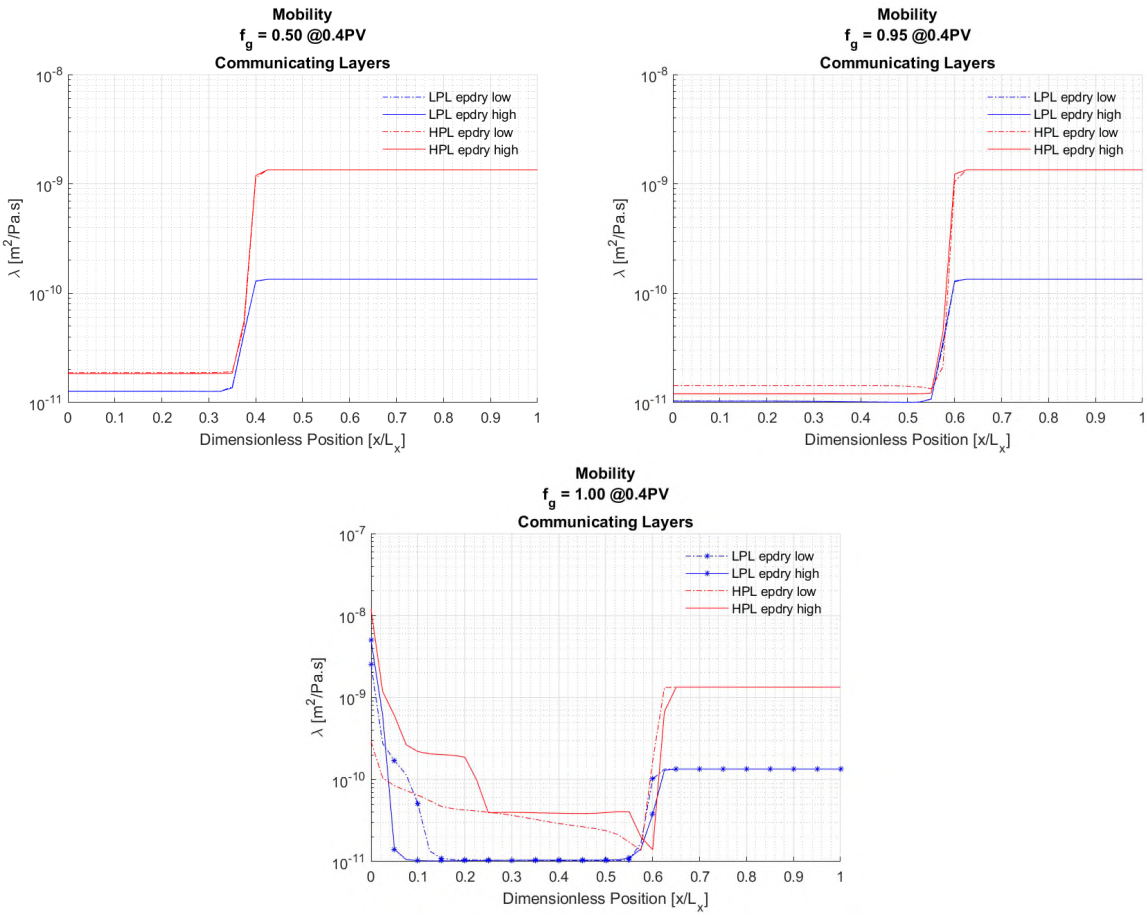

Figure 2.14 Foam Mobility per layer (communicating layers) at different injection qualities and 0.4PV. Left: fg=0.50. Right: fg=0.95. Bottom: fg=1.0

Figure 2.14 shows the total mobility in each layer at each injection quality and *epdry* value. With the location and direction of diversion, which are seen in Figure 2.13, the information can be combined in an effort to understand how diversion works. It can be seen that diversion will occur from lower mobility to higher mobility as the flow tries to find the path of less resistance. Hence, every time there is a crossover between mobilities in Figure 2.14 a corresponding change in flow can be seen in Figure 2.13, furthermore it can be seen that the larger the mobility contrast between layers the larger the diversion.

Mobility's behavior in foams is equivalent to that of the apparent viscosity, in the sense that they can indicate the ability to flow in a porous media, and both can reflect how foam dries out. They both are dependent on water saturation, which ultimately dictates foam's strength or mobility reduction. At 50% and 95% injection qualities, mobility (also apparent viscosity - Appendix B ii) behind the foam front exhibits constant values that depend on water saturation, and they indicate that foam collapse (dryout) is not occurring (Figure 2.14 right and left). Conversely, at 100% injection quality, mobility indicates that foam dryout is occurring (Figure 2.14 bottom), however, it occurs differently in the HPL and LPL indicating sensitivity to the *epdry* value. In the low *epdry* collapse

behind the foam front is rather smooth as opposed to high *epdry* where it is sharper and occurs in two steps. The profiles are shown for 0.4PV, as an example as the patterns are very similar prior BT.

The observed mobility behavior (Figure 2.14) indicates that at 50% and 95% injection qualities mobility control is better than at 100% injection quality. This difference in mobility control should also be reflected in the water saturation profiles and ultimately reflect the desaturation effectiveness. Figure 2.15 shows the water saturation profiles for the different injection qualities and *epdry* values simulated.

The saturation profiles indicate that communication between the layers attempts to equate the speed at which the foam fronts move, nonetheless the foam front moves slightly faster in the HPL. At 50% injection quality the water saturation behind the foam front in both layers indicates that desaturation is still efficient, and diversion impacts the foam fronts propagation speed and hence the pressure regimes. Similarly, at 95% injection quality desaturation is still efficient and achieves water saturations fairly homogeneous behind the shock, although spreading waves can be observed in the LPL.

Unlike 50% and 95% injection qualities, where water saturation behind the foam fronts reached values close to the injection face water saturation independently from *epdry value*, hence efficient desaturation; at 100% injection quality, *epdry* and therefore diversion, seems to have effect on desaturation behavior. With high *epdry* in the LPL desaturation below 0.36 occurs rather slowly and at 1PV nearly 80% of the layer is with water saturation above this value, contrarily in the HPL the saturation reaches its minimum value of nearly 0.27 (below *fmdry*) behind the foam front. Even though the delayed desaturation of the LPL is also seen in low *epdry* this does not have significant impact and at 100% injection quality with low *epdry* has the highest desaturation from all simulations with communicating layers.

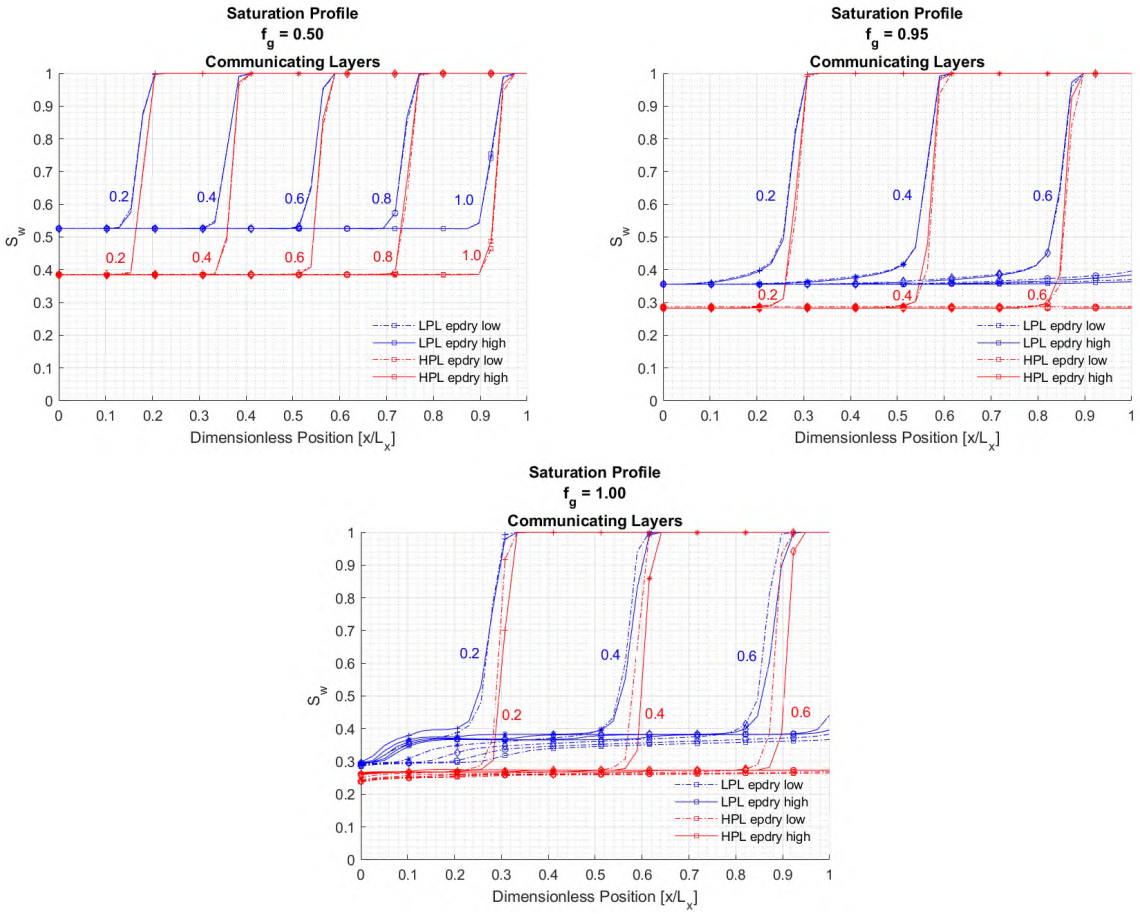

Figure 2.15 Water Saturation Profile for communicating layers at different injection qualities and dimensionless times. left: fg=0.50. right: fg=0.95. Bottom: fg=1.0

The desaturation effectiveness is better seen with the recovery factors which are shown in Figure 2.16. As in the NCL case, the total recovery factor (bottom frame) increases as injection quality increases, nonetheless it can be seen that with high *epdry* the difference between 95% and 100% is marginal. As explained in the preceding paragraph, desaturation at 100% injection quality in the LPL high *epdry is* impacted negatively by diversion and its overall effect can be seen in Figure 2.16 right, where recovery is lower than at 95% injection quality. This suggests that diversion can negatively impact recovery in the high quality regime when water saturation approaches *fmdry* and foam dryout is occurring, and the more abrupt the foam collapse (the higher the *epdry*) the more the recovery is reduced.

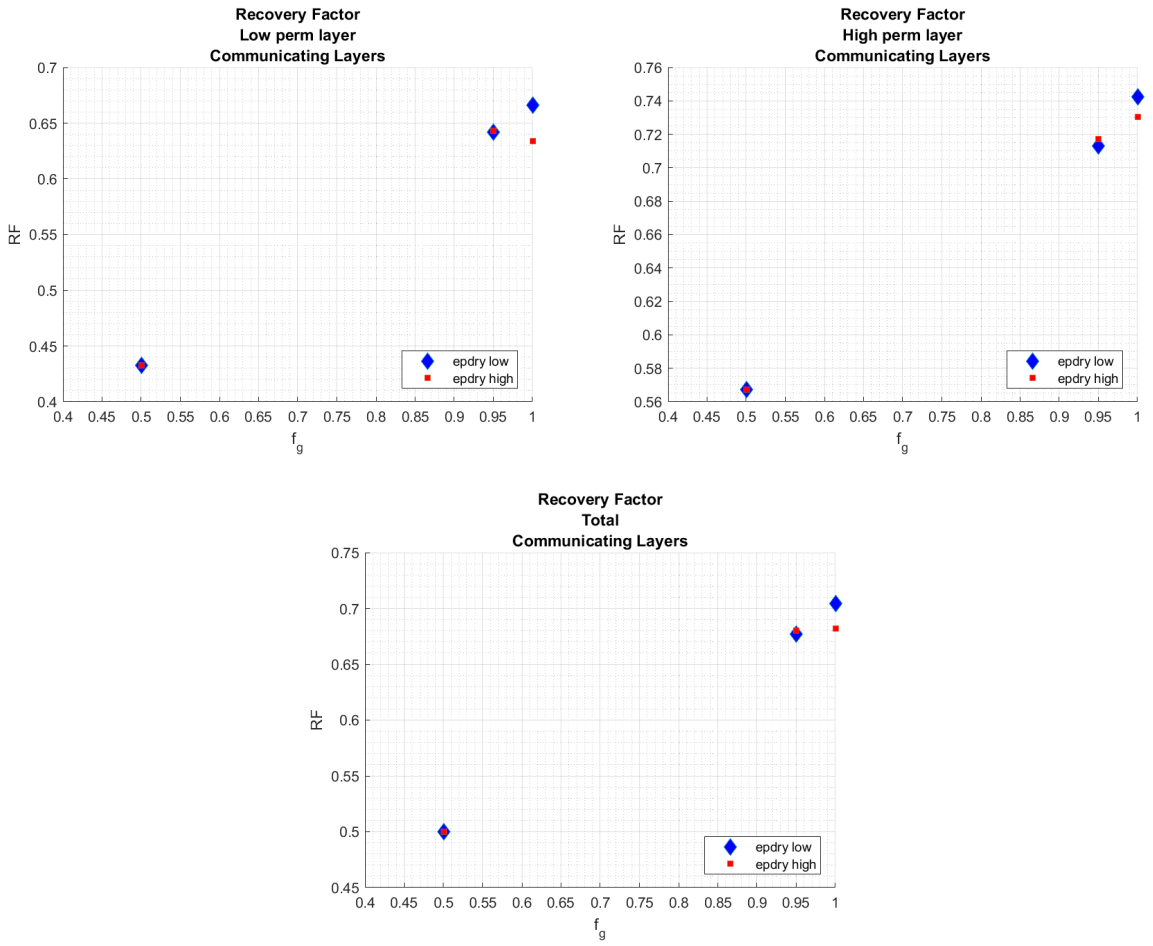

Figure 2.16 Recovery factor for communicating layers at different injection qualities. Top left: LPL. Top Right: HPL. Bottom: Total

Allowing communication between layers has shown the selective nature of flow whereby flow will divert trying to find the path of less resistance, i.e. where mobility is larger and lower pressures are achieved. Hence, the greater the mobility contrast between layers the greater the diversion. Additionally, due to diversion, foam fronts in both layers attempt to move at nearly the same speed and pressure nonetheless the higher mobility of the HPL causes slightly higher speeds and faster pressure build up at the foam front.

The STARS model (Computer Modelling Group, 2010) used to model foam shows that even though *fmmob* dictates the maximum achievable mobility reduction, the parameters in the dryout function i.e. *epdry* can have significant impact on foam performance. In the simulation, having fixed *fmmob* and *fmdry* values in each layer with a varying *epdry* showed that foam mobility can be severely impacted in the vicinities of *fmdry* where foam dries out and collapses. This effect on foam dryout can impact the reservoir desaturation i.e. High *epdry* values (abrupt foam collapse) can be linked to reduced sweep efficiency at high injection qualities (qualities whose equivalent water

saturation is below *fmdry),* as opposed to low *epdry* values (smooth foam collapse) that result in larger recoveries as injection quality increases.

2.3 High *fmmob* contrast simulation case

The preceding section dealt with the effects of flow diversion in presence of heterogeneity. It showed the selective nature of flow, where flow occurs through the path of less resistance. With the parameters used to model foam mobility control was achieved however, flow occurred preferentially through the high permeability layer. In this section, the simulation will use a *fmmob* contrast of 116:1 with the objective of seeing the effects of severe mobility reduction in the HPL.

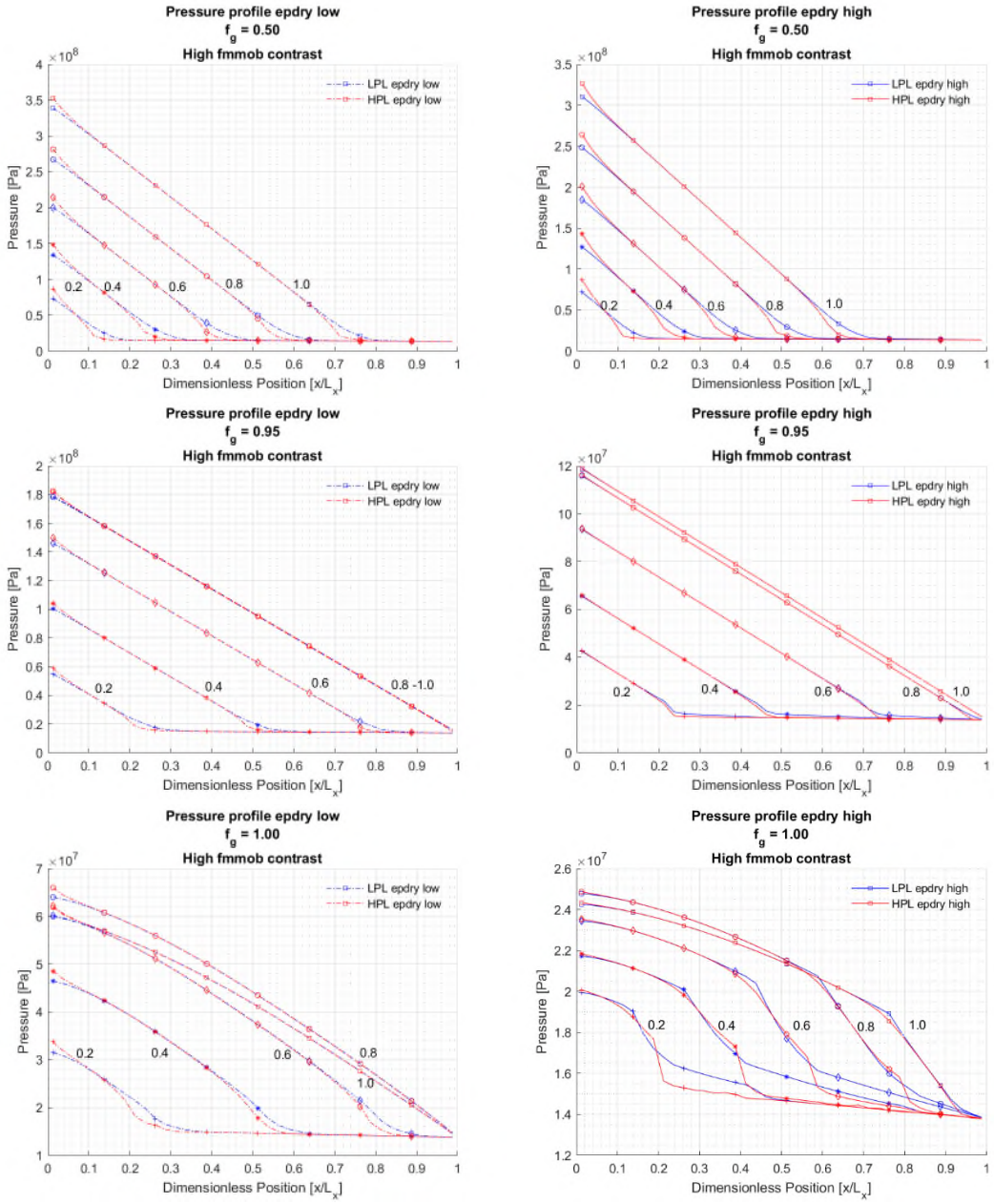

Figure 2.17 Pressure profile for high *fmmob* contrast for both *epdry* cases. Top left: fg=.50 *epdry* low. Top right fg=.50 *epdry* high. Middle left: fg=.95 *epdry* low. Middle right: fg=.95 *epdry* high. Bottom left: fg=1.0 *epdry* low. Bottom right: fg=1.0 *epdry* high

The simulations will be done for three injection qualities, namely 50%, 95% and 100%, with high and low *epdry* values. The foam model parameters can be seen in Table 2-3. At the qualities simulated it can be seen from Figure

2.3 that the HPL will always be in the high quality regime whereas the LPL will be in the low quality regime at 50% and in the high quality regime in the other simulations.

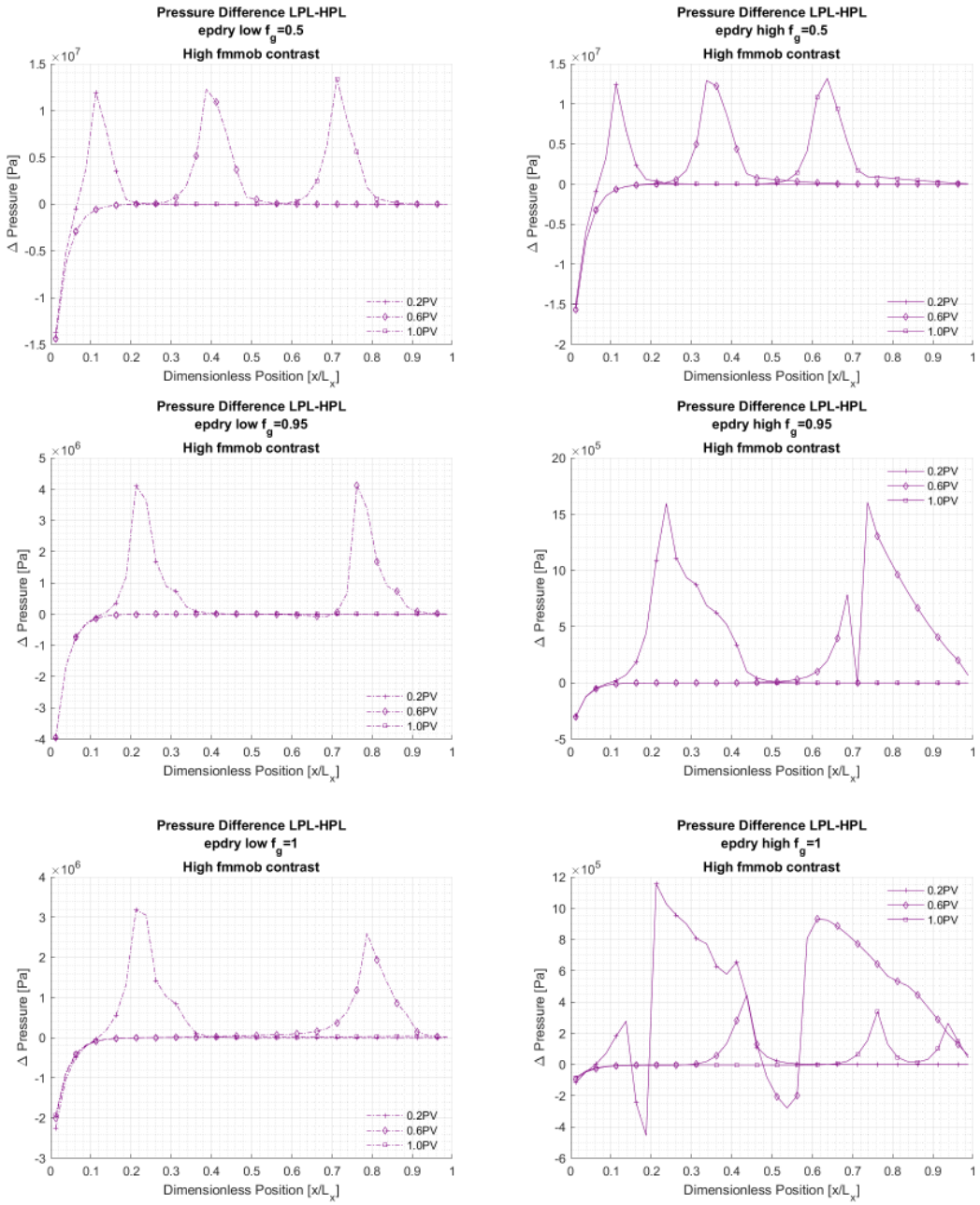

Figure 2.18. Pressure difference profiles between LPL and HPL for different injection volumes. Top left: fg=0.50 low *epdry*. Top right: fg=0.5 high *epdry*. Middle left: fg=0.95 low *epdry*. Middle right: fg=0.95 high *epdry*. Bottom left: fg=1.0 low *epdry*. Bottom right: fg=1.0 high *epdry*.

The pressure regimes, shown in Figure 2.17, show that the largest pressure regimes are achieved at 50% injection quality, where the strongest foam from the simulated qualities is found. Although foam is stronger with high *epdry* at this injection quality this doesn't imply higher pressures at the injection face. In fact, foam front advances faster in the simulations with low *epdry* which causes the reservoir to get filled with foam faster and in turns gives larger pressures at the injection face. The faster advancement of the foam and larger pressures at the injection face with low *epdry* remain valid for all the injection qualities.

At all injection qualities and *epdry* values, the mobility impairment in the HPL drives a faster pressure rise at the injection face that causes foam diversion from the HPL to the LPL. The diverted foam speeds up foam propagation in the LPL that in turn drives a faster pressure rise at the foam front creating a vertical pressure gradient. This

gradient causes foam diversion from the LPL to the HPL. In Figure 2.17 it as also revealed that faster advancement of the foam front becomes more pronounced as injection quality increases. Interestingly, although HPL is always in the high quality regime and suffers from coalescence (Shown in apparent viscosity profiles in Appendix B iii), it remains strong enough to impair mobility in the layer even at 100% quality injection.

In Figure 2.17 only big pressure differences between the layers can be seen. This masks pressure differences between layers that can be 1 or 2 orders magnitude smaller than injection face pressure. Figure 2.18 shows the pressure difference between LPL and HPL to spot the places where vertical pressure gradients occur, and therefore it allows to see the locations and direction of fluid exchange.

In Figure 2.18 as in Figure 2.17 it can be seen that close to the injection face, pressure is higher in the HPL and inverse at the foam front. Nonetheless, it shows that the segments where vertical pressure gradients exist extend more than what can be resolved from Figure 2.18. Moreover, it shows that the segment in which pressure is larger in the LPL increases as injection progresses as opposed to the segment in which HPL pressure is greater (close to the injection face) that reaches a constant width (segment along the length of reservoir) soon after injection starts.

Pressure differences by themselves cannot determine the amount of flow diversion, however they indicate the direction and locations where it occurs. To aid the understanding of foam performance with high *fmmob* values the saturation profiles (Figure 2.19) and mobility (Figure 2.20) are presented.

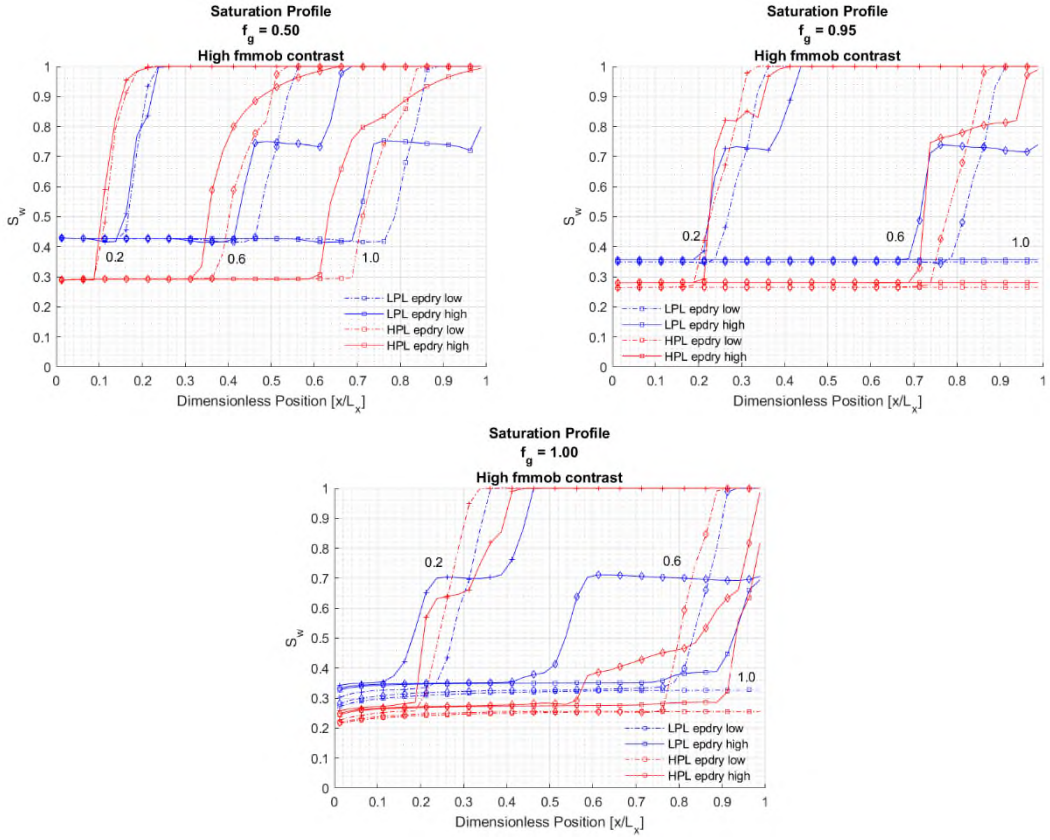

Figure 2.19 Water Saturation Profiles for high *fmmob* contrast at different injection qualities and injected volumes. left: fg=0.50. right: fg=0.95. Bottom: fg=1.0

The saturation profiles in Figure 2.19 show that high *epdry* vastly reduces vertical conformance. Whilst at low *epdry* foam fronts are nearly vertical for all injection qualities, at high *epdry* the profiles differ from vertical patterns. This type of behavior suggests that within the layers flow is being stratified. The reduction in vertical conformance in the high *epdry* simulations is better seen in Figure 2.21 where water saturation at each grid cell in the reservoir is shown. In the figure, the four bottom grids represent the LPL, the top four grids represent the

HPL and the solid lines represent the average water saturation in each layer. It is clear that the flow occurs preferentially through the top most grids of the LPL and the bottom most grids of the HPL. In consequence foam moves through the layers in what appears to be two foam fronts. The advancement of foam in this manner creates irregular pressure profiles that cause "wiggling" profiles in the mobility (Figure 2.20) and apparent viscosity (Appendix B iii). These "wiggles" are probably caused by the irregularities in the pressure profiles, that create numerical instabilities between the foam fronts, therefore interpreting foam behavior in these segments becomes unreliable.

Despite the irregularities caused by the loss of vertical conformance, the desaturation of the layers behind the foam front, shown in Figure 2.19, show that for the HPL, although increasing quality improves the desaturation of the layer, changes are not big and desaturation remains within 0.25 and 0.29 with high *epdry* and 0.29 to 0.22 with low *epdry*. In contrast, in the LPL the desaturation is considerably improved at high injection qualities and changes from 0.43 to 0.33 with high *epdry* and 0.43 to 0.28 with low *epdry*. The differences can be attributed to the fact that in the HPL all the injection is done in the high quality regime whereas in the LPL the injection is done at both high quality and low quality regimes. Furthermore, the fact that low *epdry* induces a smoother foam collapse results in stronger foams at 100% injection quality which in turn yield to better desaturation. As in the previous scenario of CL, it can be seen that saturations below *fmdry* are delayed in high *epdry*. This indicates that at *fmdry* with high *epdry*, larger water fractional flows can occur.

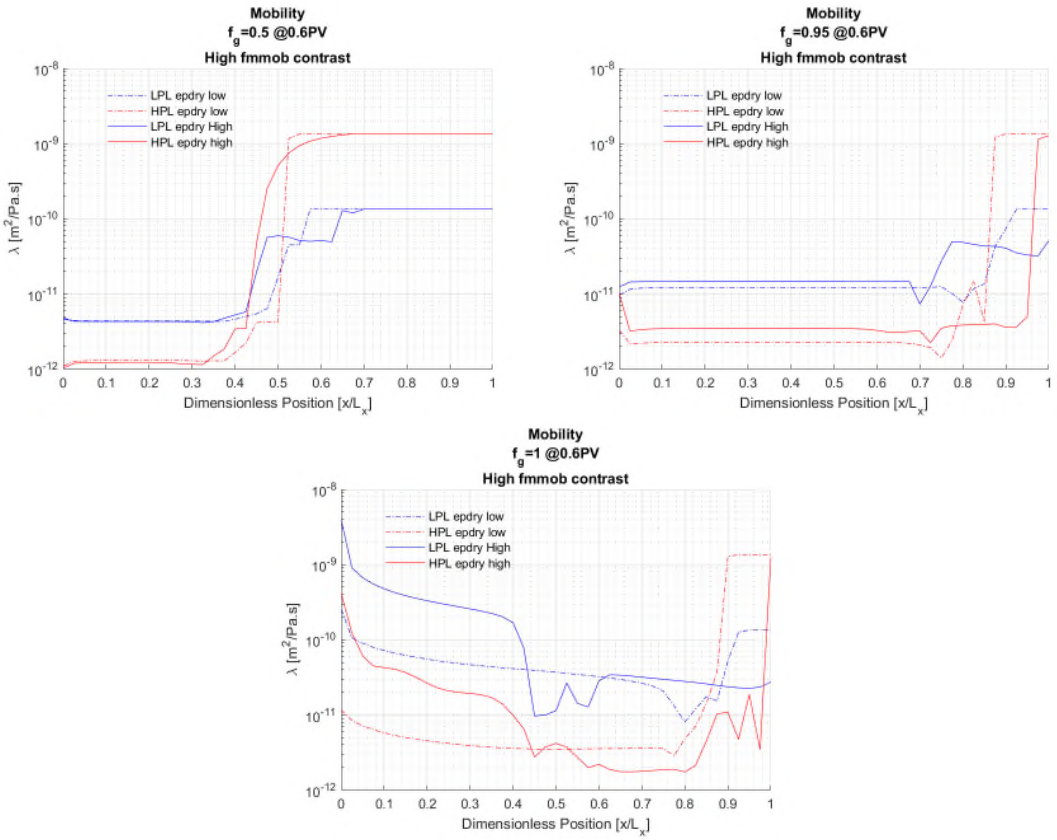

Figure 2.20 Foam Mobility per layer (high *fmmob* contrast) at different injection qualities. Left: fg=0.50. Right: fg=0.95. Bottom: fg=1.0

As far as mobility is related, Figure 2.20 shows the effect of the strong foam in the HPL, whereby foam mobility is higher in the LPL indicating that foam flows easier through this layer. The figure shows that the biggest mobility reduction is achieved at 50% injection quality which was already intuited from the pressure profiles. In contrast, at 100% injection quality the weakest foams appear and the highest mobilities appear. This results suggest that foam diversion from the HPL in the high quality regime in combination with low vertical conformance can limit foam strength. Nonetheless, it remains strong enough to cause larger mobility than in the LPL.

In good vertical conformance foam floods, such as the one described in the preceding section, it was found in that the largest mobility reduction (highest apparent viscosity) could be achieved in the high quality regime when foam contacts a fully water saturated grid-cell and forces it to go through all the range of apparent viscosities while desaturating it. Although in this simulation it is difficult to point a foam front, the just mentioned fact persists and it can be seen, at all injection qualities and *epdry,* that behind the foam fronts mobility reduction occurs in a step or "triangular" fashion indicating that maximum apparent viscosity is being achieved behind "each" foam front. Nonetheless, the values suggest that in this case, the strong foam from the HPL is not reaching its maximum value and at certain apparent viscosity value (below the maximum attainable) foam is diverted.

The previous observation can be corroborated with Figure 2.22, where the fraction of injected flow flowing through each layer is shown. At 95% injection quality in the low epdry this can be seen around dimensionless position 0.7 where a subtle increase in flow is seen in the LPL. At 100% injection quality with low epdry, this can be seen around dimensionless position 0.9 with change in slope in both flow in the HPL and LPL and at high epdry around position 0.58 it manifests itself as an increase in flow in the LPL.

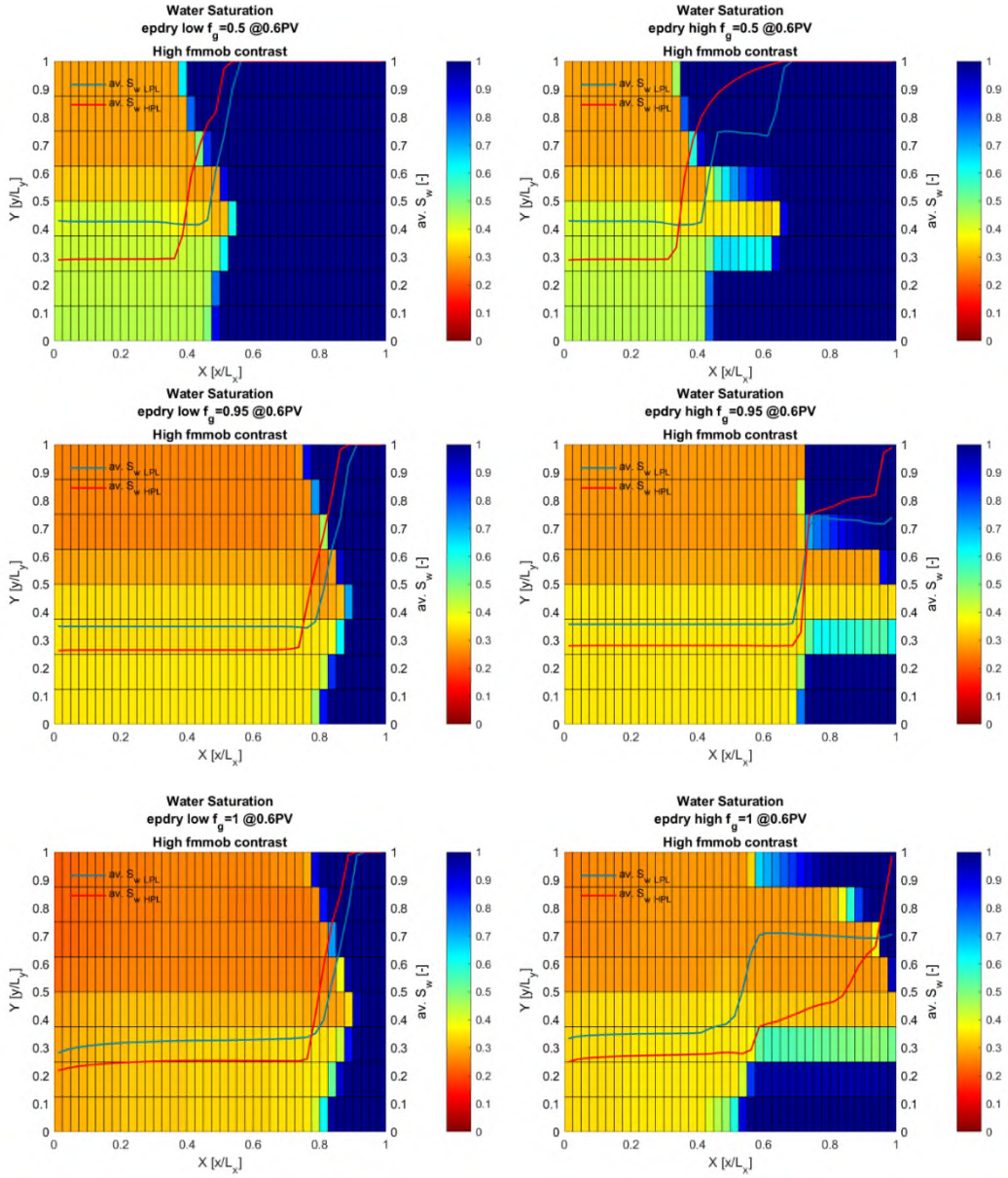

Figure 2.21 Water saturation in reservoir at 0.6PV Top 4 layers represent HPL and 4 bottom layers represent LPL. Top right: fg=0.5 high *epdry*. Middle left: fg=0.95 low *epdry*. Middle right: fg=0.95 high *epdry*. Bottom left: fg=1.0 low *epdry*. Bottom right: fg=1.0 high *epdry*

As mentioned, the lack of vertical conformance causes earlier BT and this in turns has effects on recovery. Figure 2.22 shows recovery as foam injection progresses for the different layers as well as the total recovery from the reservoir for the three injection qualities. It can be seen that the best recoveries occur with low *epdry* at 100% and 95% injection qualities, where good vertical conformance is seen. Although at 95% injection quality with high *epdry* conformance is also poor, the fact that all foam fronts arrive to the producer makes recovery efficient. Nonetheless, it is lower than its counterpart at 95% low *epdry* due to the fact that saturation at the injection face is lower at low *epdry*. Conversely, at 100% injection quality it can be seen that reduction in sweep efficiency limits recovery even below the 95% injection quality. At 50% injection quality, the fact that recovery hasn't occurred after 1PV, and the fact that water saturation at the injection face is the highest from all the simulations results in lower recovery. Moreover, at 50% injection quality, since foam in the LPL is in the low quality regime, recovery is higher in high epdry as opposed to the HPL where foam is weaker because it is in the high quality regime.

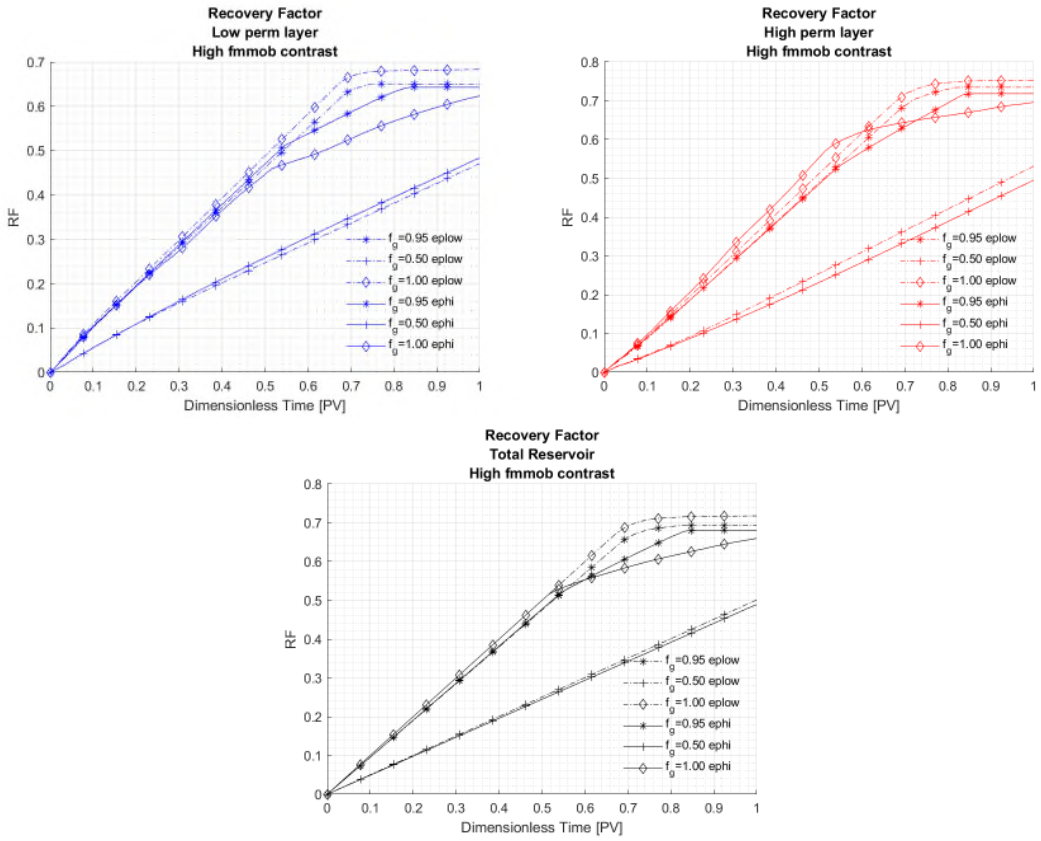

Figure 2.22 Recovery factor at different injection qualities (high *fmmob* contrast). Top left: LPL. Top Right: HPL. Bottom: Total

Using a high *fmmob* creates strong foams that can reduce mobility to the extent that a high permeability layer can have lower mobility than a low permeability layer. This indicates that with strong foams flow can be forced through a low permeability media. However, large *fmmob* contrast reduce vertical conformance which results in lower sweep efficiency. In addition, the large contrast creates simulation instabilities.

The large mobility reduction intended with strong foams appears to be limited by diversion, where foam is diverted to the higher mobility layer before reaching its maximum potential mobility reduction i.e. maximum apparent viscosity. This suggest that stronger foams don't imply better recoveries. In contrast, in presence of heterogeneities, high *fmmob* contrast is detrimental to recovery efficiency if vertical conformance is lost.

Strong foams create pressure regimes that can be challenging in applications in real world. However, STARS model uses more functions that relate to other physical considerations that can result in lower pressure regimes.

Nonetheless, the intention here is to understand how heterogeneity affects foam permeance using the dryout function.

2.4 Conclusions

In the present study it can be concluded that the dryout function in the STARS foam model can represent effects of permeability in heterogenous reservoirs, but it requires tuning the parameters governing foam behavior. Under different sets of parameters, foams can present different effects on sweep efficiency and flow diversion.

Varying *epdry* while having all other parameters fixed can yield to different results in foam performance, indicating that this parameter is fundamental to accurately describe foam floods, special if injection is being done in the high quality regime where water saturation can be below *fmdry* (saturation at which foam dryout starts occurring).

While high *epdry* and high *fmmob* create stronger foams, when heterogeneities exist, foam behavior is greatly dependent on mobility at each layer, and despite having a foam that can be potentially strong in a homogeneous media, when heterogeneities exist, foam strength can be limited due to the fact that flow will look for the path of less resistance.

Epdry has the potential of shifting the location of the transition quality, and as its value is increased the critical water saturation approaches *fmdry*. In the communicating layers simulation, at 95% injection quality, the quality regime was shifted from high quality regime to transition quality regime by increasing the *epdry* value. Nonetheless, in the high quality regime it was observed that only minor foam collapse occurred, thus only minor changes in foam performance were seen.

In the low quality regime, recoveries increase as injection quality increases and can be potentially higher as foam strength increases (higher *fmmob*) as long as foam front advances uniformly. As shown in the high *fmmob* contrast case, lack of vertical conformance results in an inefficient sweep.

In the high quality regime recoveries are larger than in the low quality regime, although desaturation stagnates at water saturation slightly below *fmdry*. Moreover, the higher the *epdry* value the closer desaturation is to *fmdry*. As noted, spreading waves with saturation below *fmdry* travel slower as *epdry* increases.

Fmmob governs how strong a foam can potentially be, nonetheless when large *fmmob* contrast exists in the heterogeneities, vertical conformance can be impaired resulting in lower recovery efficiencies, with the disadvantage that numerical errors may arise from the simulation.

3 Experimental Section

3.1 Microfluidics Introduction

In porous media, pores and fractures are usually in the order of microns, microfluidic devices can be manufactured to this scales enabling visual characterizations of flow. Microfluidics is a discipline that studies movement, handling and manipulation of liquid substances across nano, micro and macro scales (Lifton, 2016). The use of microfluidics gives an unlimited range of possible pore networks configurations and fractures due to its manufacturing capabilities. In fact, the manufacturing capacity is so large that very accurate representations of porous media can be achieved, nonetheless the physica-chemical properties of porous networks is still limited. Although the flow in micromodels is not a 3D rock, even with similar grains and pore space (Gauteplass et al., 2015), foam generation mechanisms and fluid-fluid-solid interactions observed in micromodels can be used to understand the phenomena in real rocks.

Flows in reservoirs are often characterized by dimensionless numbers such as Reynolds and Capillary. Therefore, when comparing flow behaviors these should be considered and it is important to be aware that at microfluidic scales these numbers may vary in orders of magnitude. Reynolds number is significantly lower due to characteristic lengths, and capillary number significantly higher due to the larger speeds involved in microfluidics.

3.1.1 Hydraulic Capacitance and bottle neck effect

It has been assumed that the microfluidic system has rigid surfaces. This consideration yields to mass being constant in time. Nonetheless, the fact that fluids can be slightly compressible, and walls can deform with pressure results in changes in the volume stored in the microfluidic system. This delta volume is referred as compliance. The effect of compliance in the microfluidic set-up is lag between the response of the different sensors in the system e.g. pressure will build up before the microscope sees any fluid movement.

Furthermore, at macroscale, it is usually assumed that compressibility is related to Mach number (ratio of fluid speed to the speed of sound) but at microscales, viscous effects can have effects on compressibility. This anomaly is presented in a microfluidic system as a long transient prior steady stabilization of pressure under constant mechanical driving motion such as that generated by syringe pumps. This effect is referred as the “Bottle neck effect” [30]. The latter transient effect is the main contributor to the lag in the response between pump start and flow movement. The magnitude of the effect depends upon the velocity at which pumps are run and the changes in cross sectional areas throughout the system and as explained the system compliance.

3.1.2 Mixing in Microfluidics

In many microfluidic applications it is often necessary to create mixtures. The fundamental problem of microfluidic mixtures is the low Reynolds number where hydrodynamic instabilities and turbulence are practically nonexistent (Tabeling, 2011). Consequently, if no mixing enhancing devices are used, the mixing in the microfluidic system will be dominated by a combination of diffusion and convection.

The Peclet number, given in Equation 3.1.1 relates the magnitude of the convective fluxes to that of diffusive fluxes. In the numerator *u [m/s]* is the velocity, and *l[m]* is the length of the system, and *D [m^2/s]* in the denominator is the diffusion coefficient. Thus, the higher the Peclet number the higher the influence of convection over diffusion. Equation 3.1.2 is referred as the convection diffusion equation and describes the changes in concentration.

$$Pe = \frac{ul}{D} \qquad \text{Equation 3.1.1}$$

$$\frac{\partial c}{\partial t} + \vec{u} \cdot \nabla c = D\nabla^2 c$$ Equation 3.1.2

From Equation 3.1.2and Equation 3.1.1 it can be concluded that the mixing process can be separated in two different processes, i.e. diffusion across scalar gradients and shortening of the diffusion length by motion of the fluid. Solving Equation 3.1.2, whilst neglecting the convection term (which is possible when velocities are low, like in microfluidic flows), results in an estimation of the required lengths (Equation 3.1.3), and times (Equation 3.1.4) to achieve full miscibility.

$$l_{diff} = \sqrt{Dt}$$ Equation 3.1.3

$$\mathrm{t}_{ch} \propto \frac{l^2}{D}$$ Equation 3.1.4

In a mixing process, such as the one presented in Figure 3.1, where two fluids under steady conditions are brought together and flow parallel to each other, diffusion occurs perpendicular to the flow direction. It can be observed from Figure 3.1, that the concentration profile changes downstream while fluids are being mixed. Equation 3.1.4 and Equation 3.1.3 will determine the required length and time to achieve uniform concentration (miscibility). If mixing can not be achieved by the mechanisms explained, mixing can be enhanced through stirring or mixing devices.

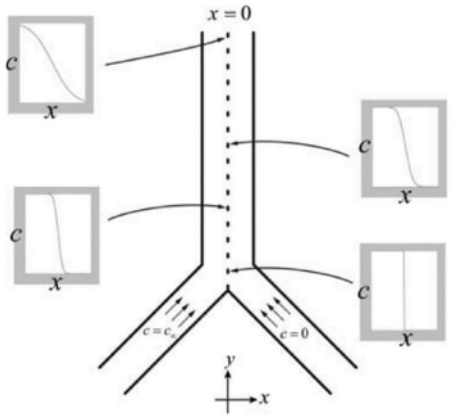

Figure 3.1 Two inputs one output microfluidic device with only diffusion occurring in the x-direction

3.1.3 Microfluidic studies in foams

As far as pure foam floods in microfluidic chips, studies such as the one performed by Ma et al. (2012) and Gauteplass et al (2015) on chip configurations with high and low permeabilities regions showed that injecting gas along with a surfactant solution in a co-flow was beneficial for diverting flow from the high perm region towards the low perm region. The research showed that foam is effective at displacing the oil from the low perm region as consequence of the reduced mobility in the fracture and high permeability region. One of the observations done by Ma (2012) revealed that low permeability regions were prone to weak foams as opposed to high permeability regions where foam were stronger. Further studies have shown the effect of fractures geometry on the mobility reduction factor (Buchgraber, Castanier and Kovscek, 2012).

Quennouz et al. (2012) tried to characterize foam generation. In a simple foam generation set up for co-injection aqueous and gas phases at fixed pressures, foam texture was categorized as a function of injection pressures. In Figure 3.2 five categories of foam were identified. Region 1 and 5 represent single phase high pressure regions where no foam was generated. Starting from region 1 where only water was seen, with increasing the gas pressure region 2 shows small bubbles flowing independently in the aqueous phase, representing weak foams. As the gas pressure increases more, in region 3 the foam becomes stronger and lamellas start appearing. At region 4 strong foams are fully developed with the aqueous phase present only in the lamellas (Quennouz et al., 2012). As seen in Figure 3.2, foam generation exhibits a linear relationship between gas pressure and liquid pressure with an initial gas pressure threshold.

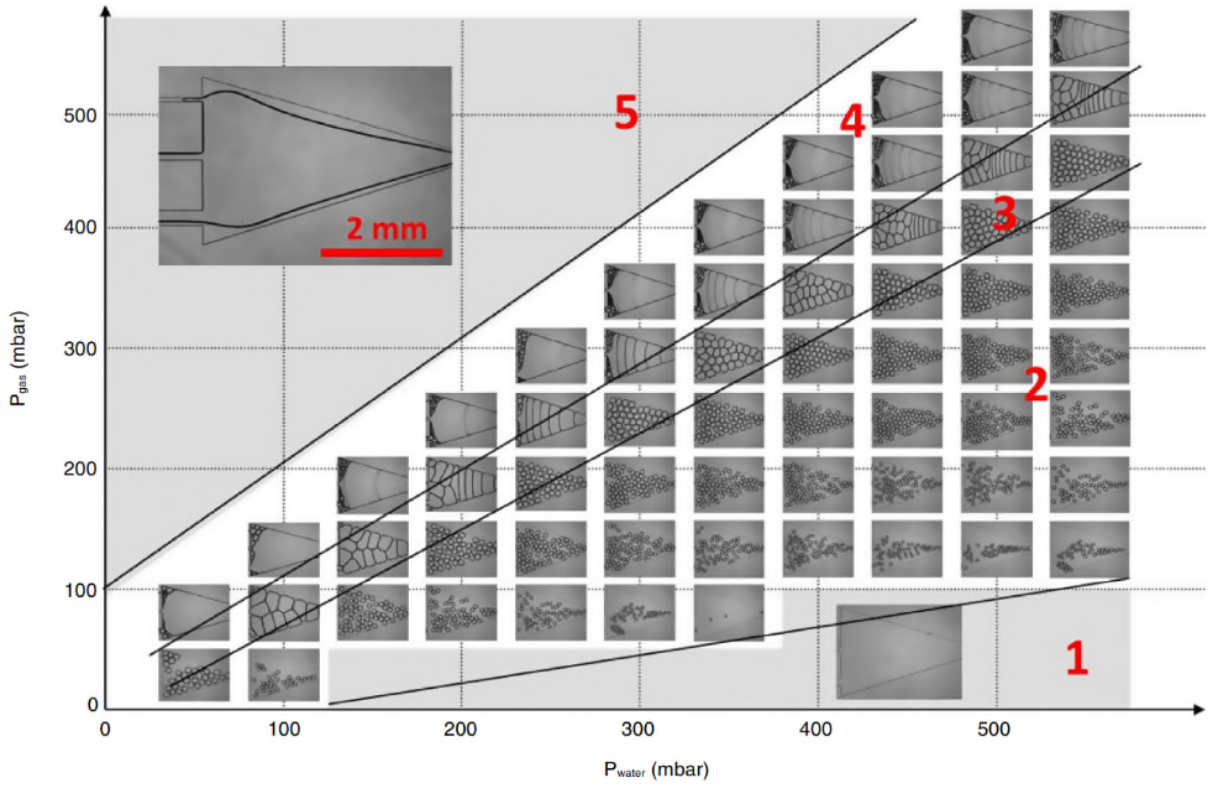

Figure 3.2 Diagram of foam generation according to injection conditions (Quennouz et al., 2012)

As far as microfluidic studies of foams in presence of oil, studies from authors such as Kuhlman (1990), Sagar & Castanier.(1997) and Osei-Bonsu et al. (2017) focus on immiscible or semi-miscible conditions. While using supercritical CO_2 with crude oil (semi-miscible), Kuhlman (1990) found that oil spreading is dominated by the low interfacial tension between oil and gas, $\sigma_{ow.}$ However, if the interfacial tension between water-gas, $\sigma_{wg,}$ drops below the oil-gas IFT, σ_{og}, oil tendency to spread is reduced. Nonetheless, this effect is not generalized since the spreading also depends on surfactant type as noted by the author.

When the effects of oil are not merely spreading, foams can be destabilized through several mechanisms. In presence of micro-emulsions, the surfactant may segment into the oil, enabling the dehydration of the lamellae in the aqueous phase. Another mechanism involves the spreading of oil around the lamellae and displacing the foam stabilizing interface (Sagar and Castanier, 1997).

Osei-Bonsu et al. (2017) studies on the effects of oil viscosity revealed that the generation of stable foam is delayed in presence of light oil while the dynamics of oil entrapment is dictated by the stability of the foam. Their experimental work showed that light oils are more detrimental to the stability of foam since light oils limits foam

creation unless the appropriate surfactant is used. The negative effect may demonstrate itself by delaying foam generation and propagation speed.

In micromodels with pre-generated foam, bubbles bursts are observed upon contact with oil. This results in gas escaping through the porous network and displacing some oil on the way. When bubbles burst, Osei-Bonsu et al. (2017) observed that the surfactant released also contributed to oil mobilization by reducing the interfacial tension between oil and water, thus lowering capillary forces.

In micromodels, oil displacement at the initial stages is dominated by the gas released resulting from bubbles burst independently from oil properties. The subsequent displacement is a function of properties such as oil viscosity. As stated previously, the increased sweep efficiency is dominated by foam stability, which depends upon the entry coefficient, which can be thought as a barrier that the oil droplet needs to overcome before it can spread or bridge the gas-liquid interface. The strength of this barrier – Pseudoemulsion film – increases with hydrocarbon chain length, therefore the heavier, more viscous oils permit the development of more stable foams.

As the critical foam quality is reached, increasing foam quality promotes bubble collapse and coarsening, consequently more gas escapes from the pore network delaying the propagation of stable foams. Furthermore, the effect of flowrate is related to the rheological nature of foams, which in general is shear thinning. Hence, since oil viscosity is constant, the viscosity ratio reduction observed at high flow rates is attributed to the reduction in foam apparent viscosity (Osei-Bonsu et al. 2017).

Schramm and Novosad (1990) found that the foam-oil interaction appears not to involve the spreading of oil unlike the observations from Osei-Bonsu (2017). In contrast, Schramm and Novosad (1990) found that foam stability in the presence of oil depends to the degree to which oil can be emulsified and imbibed into foam lamellae; they found an inverse relation between emulsification and foam stability, thus the smallest degree of emulsification the more stable the foam. When oil emulsification occurs, oil drops enter and rupture the lamellas. The two opposed explanations rely on the behavior at the pseudoemulsion film (gas-aqueous-oil interface), while some argue that the spreading of oil affects lamellae elasticity properties and viscosity the other argue that the destabilization is caused by the pseudoemulsion film thinning.

When foam contacts oil, the foam can spread over oil and become emulsified or it can enter the lamella Schramm and Novosad (1990), as shown in the top right from Figure 3.3. However, if oil spreads over the foam, the effect is foam destabilization.

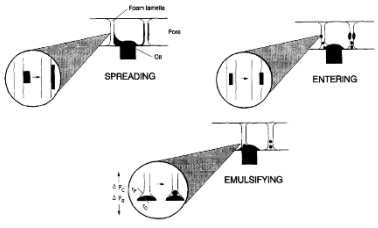

Figure 3.3 Oil foam interactions according to Schramm et al. (1990)

The interaction of oil with foam can be subdivided into three main foam types according to Schramm (1990). The foam types are seen in Figure 3.4.

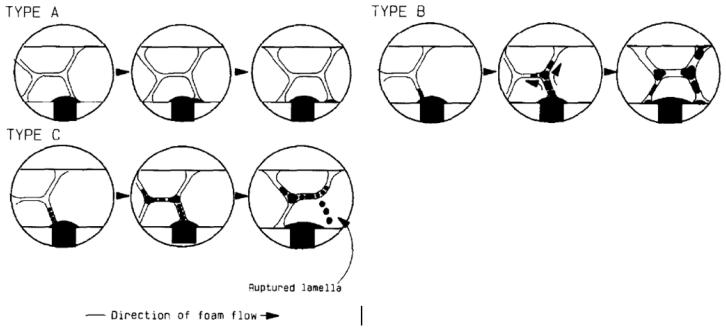

Figure 3.4 Foam-oil interactions. Foam types as viewed from microscope

In type A foams from Figure 3.4, little interaction of foam and oil is observed without any observable destabilizing effect. The main transporting mechanism involves oil droplets entrapment along the plateau border along the wall and then transported downstream. The micro-displacement is attributed to Laplace capillary suction, however only little amounts of oil are transported.

In type B foams from Figure 3.4, oil is emulsified (into small droplets) and transported along the plateau borders. As the plateau borders become saturated with oil lamellae rupture started occurring creating a destabilizing effect is observed. Oil is transported some distance before lamellae rupture occurs.

Type C foams from Figure 3.4, showed the most severe interaction. Upon contact of oil and foam, very small oil droplets are formed and transported using the mechanism described in type B foams. However, due to the smaller size of droplets, thinner lamellas were 'invaded' further promoting foam destabilization.

The oil destabilization effects according to the foam type created depends upon the oil droplet size under emulsification. The smaller the droplet size the larger the effect. Under this scenario the most oil-resistant foams are those which have larger oil-aqueous phases interfacial tension and low surface tension; i.e. negative entering coefficient.

3.2 Experimental motivation

To better understand how foam displacements work, experiments at micro and macro scale such as microfluidics and core experiments can be conducted. Understanding the interactions between foams and oil at microscale can ease the understanding of the behavior of foam floods at macroscale.

It is known that the presence of oil can be detrimental to foam stability through different mechanisms. These destabilization mechanisms come from studies of oil- foam interaction under immiscible conditions, i.e. when gas and oil are present in different phases. However, it is not rare to find cases where reservoir fluids are miscible or partially miscible with the foaming gas Osei-Bonsu et al. (2017) such as when injection CO_2 during tertiary recovery. Hence, interest in understanding the behavior of miscible CO_2 foams in EOR processes arises as there is little knowledge on how oil-CO_2 interactions affect foam behavior. In miscible displacements, the gas and oil will become one phase by any of the mechanisms explained in section 1.1. This implies that at the displacement front a mixture gradient from pure gas to oil will be present. Since the mixture is in a single phase, the mechanisms by which oil collapses foam are not necessarily equivalent, and therefore studies such as the one pretended here, will complement these knowledge. The single oil-gas phase condition provides the baseline for the experiments intented in this project; extending the studies done by Kahrobaei et al. (2017) on the effects of oil in CO_2 foams under miscible conditions in the core scale.

Throughout this document, foams have been referred as a gas dispersed in a liquid phase but, in the experiments conducted in this project, the so called -gas phase- will not be a gas per se, but rather a supercritical fluid.

Nonetheless, the term foam will be used to refer to the colloidal dispersion formed by C_{10}-CO_2 and Surfactant. Furthermore, for coherence and to ease the understanding of the jargon used in foams, that can be sometimes confusing, the term *"non-aqueous phase"* will refer to fluid arising from the miscible mixture of C_{10} and CO_2; x will refer to the molar fraction of CO_2 present in the non-aqueous phase; and Finally, quality -f_{na}– will refer to the ratio of mixture flowrate to total flowrate (non-aqueous phase and surfactant solution) as explained in section 1.2.1, though the subscript is changed to mark a difference between immiscible and miscible conditions.

The CO_2 foam scans conducted by Kahrobaei et al. (2017) in cores revealed three distinctive apparent viscosity regimes, shown Figure 3.5, that are dependent on the CO_2 fraction. Regime 1: Increasing apparent viscosity with increasing CO_2 fraction, Regime 2: Decreasing apparent viscosity with increasing CO_2 fraction and Regime 3: Constant viscosity independently of the CO_2 molar composition. It is evident that the highest apparent viscosities occur at pure foam *x=1* and pure emulsion *x=0*, regimes 1 and 2 respectively. Regime 3 exhibits a behavior whereby the viscosity is nearly independent from the non-aqueous phase composition. Furthermore, the apparent viscosity is lower than pure foam and emulsion.

With this intriguing behavior in mind, the objective of this study is to investigate how variations in non-aqueous phase composition -x- and quality -f_{na}-, affect foam properties such as texture and rheology with an approach that will focus on the visual observations done at micro-scale level, using a microfluidic chip under a microscope.

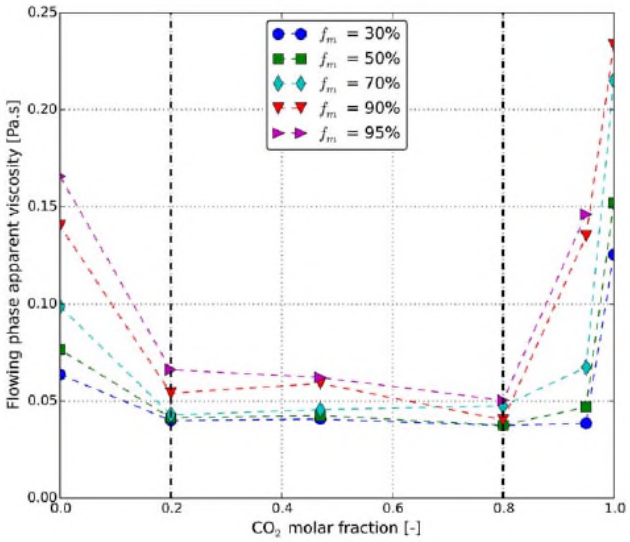

Figure 3.5 Kahrobaei et al. (2017) CO2 foam apparent viscosity regimes

3.2.1 Experimental Set-up design

To study the microscale foam behavior, a microfluidic set-up consisting of pumps to drive the fluids, a microfluidic chip -representing the reservoir/core- under a microscope and capillary tubes will be used. The schematic representation of the set-up is presented in Figure 3.6. This design will allow the combination of different flows into microfluidic channels under the assumptions stated in 3.1.2 where the fluid will be considered as a Stokes flow, with time and distance as the mixing drivers. The considerations for flow and mixing within this project are discussed in section 3.2.6.

One of the main challenges that arise while working with microfluidics is the difficulty to reproduce *normal* reservoir pressure and temperatures. As an example, the electronics inside the microscope and control module in the pumps can be jeopardized at high temperatures; Therefore, high temperatures should be avoided. With regards to pressure, microfluidic chips are normally made from glass, resulting in pressure limitations, which for the chip used in this project is 100 bar. With the temperature and pressure limitations in mind, the operating

point should be such that full miscibility between C_{10} and CO_2 can be achieved while having temperature and pressure as low as reasonably possibly. The set-point pressure will be supported by the back-pressure nitrogen tank, shown in the upper right corner of Figure 3.6. and the temperature will be provided by a heating cell.

Because microfluidic scale is comparable to dust/air debris particles, and the set-up is placed in a non-isolated environment, it is important to have a means to operate the set-up without exposing its internal components to the surroundings. The elements such as the external line, vacuum pump and coupled fluid reservoirs (CO_2 bottle, green and blue cylinders) shown in the schematic provided in Figure 3.6. provide redundancy to the system to meet the design requirements of having an isolated system.

To conduct the experiment, it is not only important to have a robust set-up but also an appropriate selection of the operating conditions in terms of pressure, temperature and velocity. The correct selection of these parameters will enable the execution of the project objectives while keeping the equipment within its operational limits. For this purpose, each individual parameter that is required as input will be treated throughout the chapter.

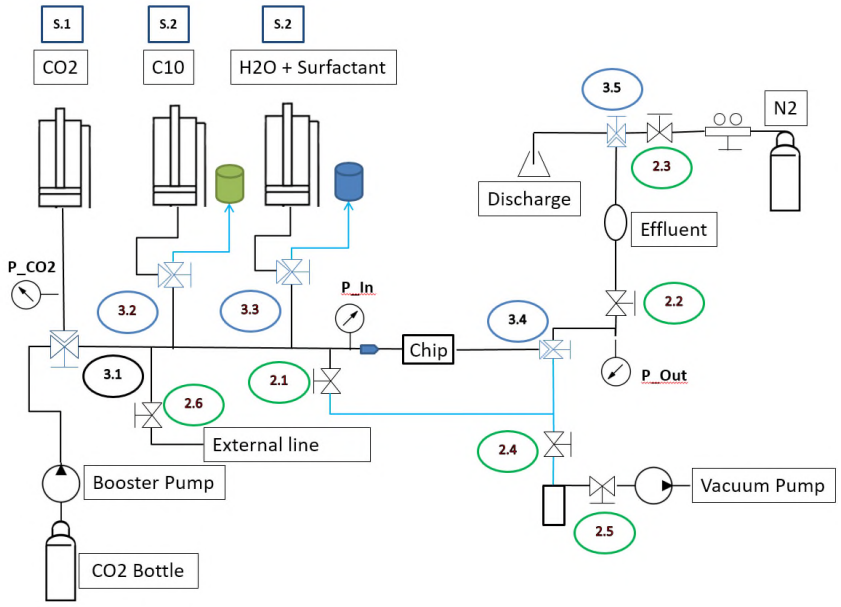

Figure 3.6 Microfluidic set-up Schematic

Furthermore, to be consistent with Kahrobaei et al. (2017) experiments, the degrees of freedom will be the same, i.e. flow rate will be fixed at a constant value, and the inlet pressure and temperature will be kept as constant as possible, the same chemicals will be used, and brine salinity and surfactant concentrations will remain unaltered. However, due to limitations in microfluidic set up, the temperature and speeds used in the experiments that inspired this project will be difficult to honor. Nonetheless, to maintain some degree of consistency between experiments, the *gas phase* will remain a supercritical fluid, reservoir speeds will be in the order of ft/d range and the temperature will be kept as steady as reasonably achivable by placing the set-up in a pseudo-insulated cage with a heating cell. Although the cage reduces temperature variations, the mean temperature fluctuates a couple °C around the set point. The experimental set point will be further discussed in section 3.2.4.

3.2.2 Materials

Alpha olefin sulfonate - AOS (BIO-TERGE AS-40)- will be used as the surfactant in a weight concentration of 0.5% diluted in a 1% NaCl weight concentration brine. This surfactant belongs to the ionic surfactant category and its critical micelle concentration, CMC, is 0.008 wt% in a 1 wt% NaCl brine (Kahrobaei, Vincent-Bonnieu and

Farajzadeh, 2017). Decane (n-C10) and Carbon Dioxide (CO_2) will represent the oil and the gas phases respectively. A microfluidic chip will be used as the porous media.

The microfluidic chip is a Micronit rectangular 90x15x1.85 mm D263 borosilicate-glass micromodel whose schematic is shown in Figure 3.7. It consists of two sintered substrates with thicknesses of 1100 μm and 750 μm with pattern imprinted using a wet-etching method. The pattern is shown in Figure 3.8. The etch depth on each substrate is 5 μm, hence the total etch depth is 10 μm. The pattern consists of circular, normally distributed pores, aligned in 849 columns with 10/11 pores per column. The pore size varies from 18μm to 45μm. The micromodel physical characterization is shown in section 3.2.3. The pressure rating of the microfluidic chip is 100 Bar.

The micromodel will be placed in a Leica microsystems DMi8 inverted light microscope. The fluids will be pushed using three Harvard Apparatus PHD Ultra 4400 syringe pumps using 2.5 ml and 8 ml stainless steel syringes.

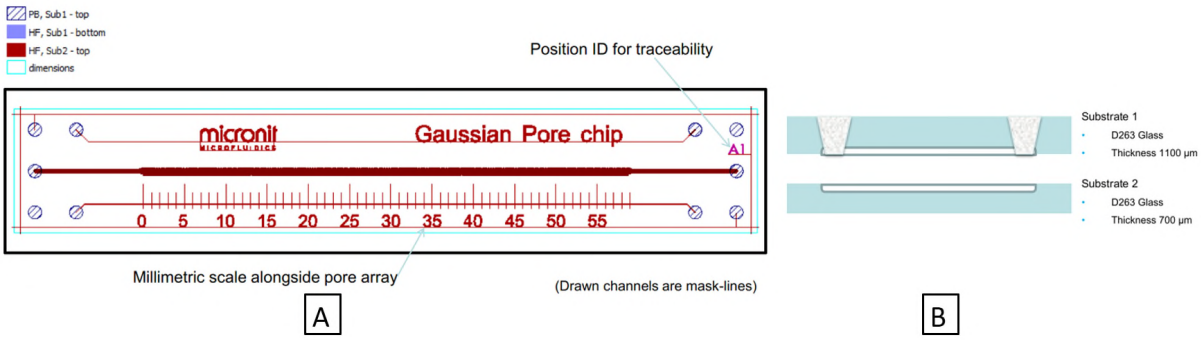

Figure 3.7 Chip design provided by Micronit

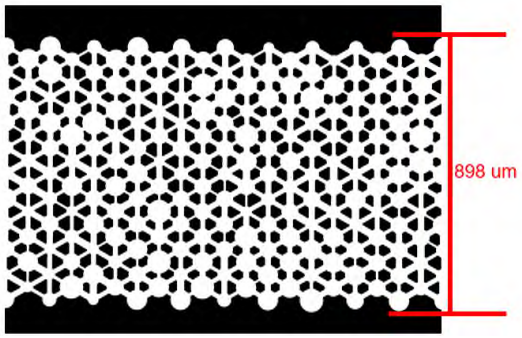

Figure 3.8 10/11 x 849 gaussian pore pattern etched on micromodel

3.2.3 Microchip Characterization

The permeability of the microchip is determined by measuring the pressure drop across the microfluidic chip length at different demi-water flowrates using Darcy's law. Single phase Darcy's law can be arranged in such way that the flow velocity can be plotted in the ordinate and the ratios of pressure drop and viscosity in the abscissa.

$$\frac{q}{A_t} = k\left(\nabla P \frac{1}{\mu}\right)$$ Equation 3.2.1

It can be seen from Equation 3.2.1 that the proportionality constant between the LHS and RHS of the equation is given by the permeability, *K*, as shown in Figure 3.9. The measurements are taken in increasing and decreasing velocity steps to verify hysteresis behavior.

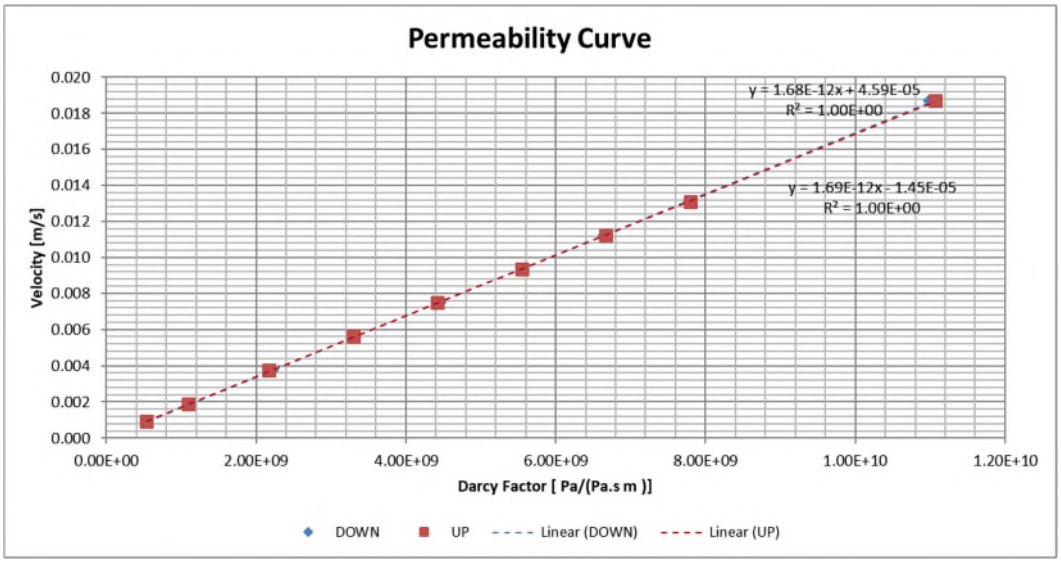

Figure 3.9 Microfluidic chip permeability calculation

The flowrate *q* is given by pump and it is converted into velocity by dividing it by the cross sectional area of the microchip, *A*. The Microchip cross sectional area is determined by the total etch total: 10 μm, and the pore-network width: 898 μm. The test fluid used is water at room temperature and pressure, with viscosity of 9.51 *Pa.s.*

The porosity of the microchip is estimated using image analysis. It is important to mention that although in reservoirs porosity is referred to the 3D volume, the "chip" porosity for the experiments is approximated using the 2D porosity measured from the images captured by the microscope along the length of the microfluidic chip pore network, similar to the one shown in Figure 3.8. The underlying assumption is that the chip is a 59 x 0.898 mm rectangle composed of "grains" and pores. Using a complete picture of the microchip pore network the grains individual sizes, grain distribution and total grain area can be estimated using image analysis. The porosity can be calculated using the total chip area and total grain area.

CHIP PROPERTIES	
Grain Area [[μm]	15430884
Chip Width [μm]	898
Chip height [μm]	10
Chip cross section Area [μm^2]	8980
Chip surface Area [μm^2]	52982000
Chip effective length [μm]	59000
Chip Porosity	0.71
Chip effective volume [μl]	0.38
Chip Permeability [m2]	1.68E-12

Table 3-1 Microfluidic chip characterization

Figure 3.10 shows the grain size distribution, which is obtained by measuring the surface area of all the grains in the microchip using image analysis and placing them in a histogram. The grain size distribution as, expected normally distributed. Using the microchip surface are given in Table 3-1, the chip porosity is determined to be 0.71. The relevant physical properties of the microchip are given also given in the just mentioned table.

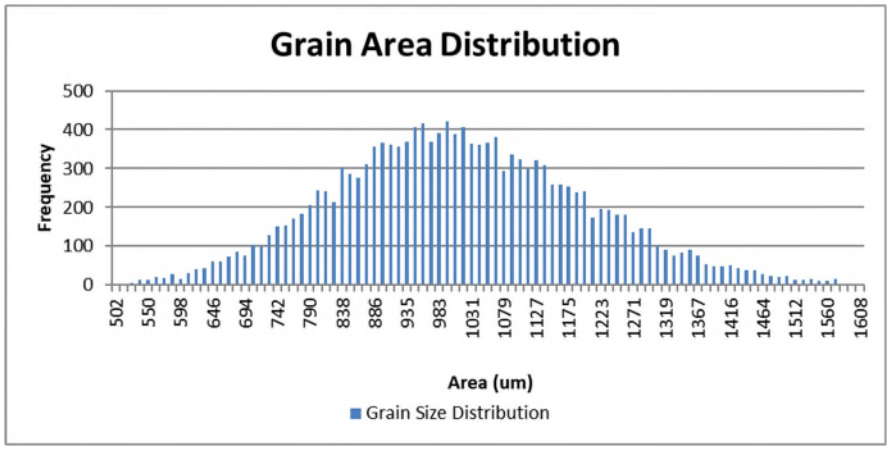

Figure 3.10. 2D Porosity and permeability graphs

3.2.4 Pressure and temperature operating point

Since the experiment objective is to perform characterization of foam under miscible C_{10}-CO_2 conditions, the operating point should be chosen such that it falls in the single phase region of the of the C_{10}-CO_2 binary diagram, which illustrated in Figure 3.11, which obtained by simulating the PT diagram in PVT sim using Peng-Robinson EOS. The intersection of the dashed orange horizontal line at 77 bar (7.7 MPa) and the dashed orange vertical line at 30°C (303 K) in Figure 3.11 presents an operating point that fulfills the experimental requirements of single phase for all molar compositions while being below the 100 Bar rating of the microchip. This condition will be referred as the experimental condition.

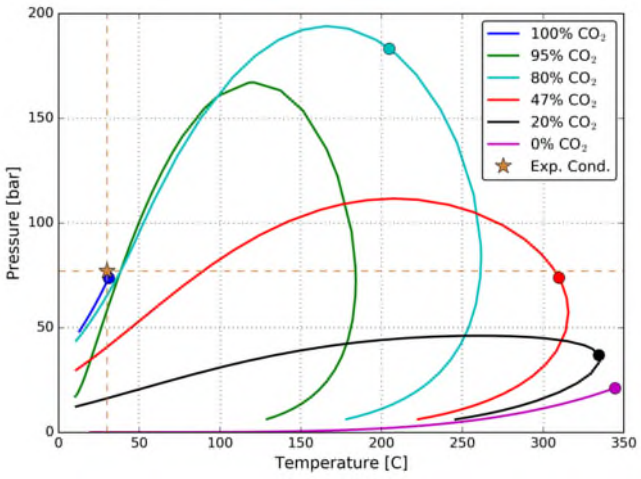

Figure 3.11 Phase diagram of CO_2 – C_{10} binary system. Calculated using PVT sim and Peng Robinson EOS

3.2.5 Non-aqueous phase density estimation

Estimating the density of the C_{10}-CO_2 is required for the calculation of the experimental volumetric flows. The densities can be obtained by either direct measurements using experimental methods or approximations using equations of state. For the C_{10}-CO_2 mixture at the experimental conditions (7.7 MPa and 303 K), literature is scarce, resulting in limited availability of "real" densities. Hence, an EOS will be used to obtain the densities for the different molar fractions of C_{10}-CO_2 mixtures. To compensate for the uncertainty generated by the unavailability of experimental measurements at the experimental conditions, a comparison between experimental measurements close to this point and different EOS will be done. This will give an idea about the accuracy of the EOS outputs and therefore provide an idea on the accuracy of the estimations.

The equations of state (EOS) that will be compared are: Peng Robinson (1976) , GERG-2008 (Kunz et al., 2012), Helmholtz-energy explicit (HEOS) (Kunz and Wagner, 2012) and modified Benedict–Webb–Rubin (MBWR) (Outcalt

and McLinden, 1996). The experimentally measured CO_2-C_{10} mixture densities that will be compared against the EOS are the ones performed by Zambrano (2016) and Song (2012). The comparisons are shown in Figure 3.12 and Figure 3.13. The EOS densities outputs are represented by solid lines while the experimental measurements are represented by markers. The comparisons are done at 10 Mpa (100 Bar) and 313 K and 323 K since these are the literature measurements closest to the operating point.

The comparison between the experimental measured and EOS estimated densities suggest good agreement between experimental measurements and estimations. Since CoolProp software (Bell et al., 2014) uses HEOS and this software is being used to estimate the thermodynamic properties, an error estimation with the experimental measurements and this EOS is presented in Figure 3.14 and Figure 3.15 . The maximum error obtained in these graphs will be used to get an idea on the maximum error that can be attributed to the density estimation.

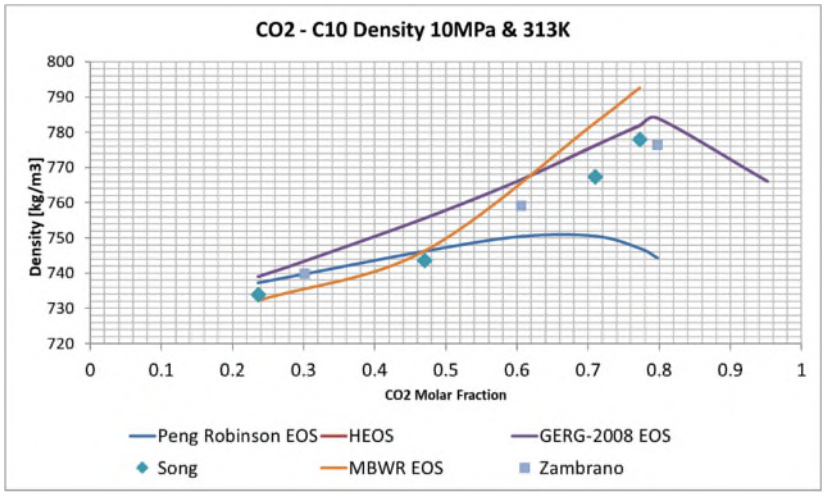

Figure 3.12 $CO_2 - C_{10}$ Density experimental and EOS comparison at 10MPa and 313K

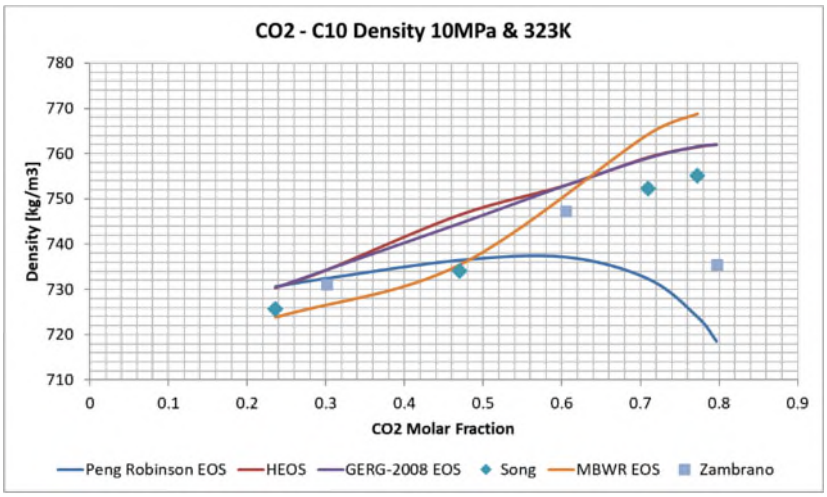

Figure 3.13 $CO_2 - C_{10}$ Density experimental and EOS comparison at 10MPa and 323K

The largest difference between the experimental measurements and HEOS at 313 K and 323 K is 3.5% and occurs with Zambrano (2016) measurements at 0.797 CO_2 molar composition. This difference will be used to calculate the flowrate range at $f_g=1$ and 200 ft/d, which is the highest non aqueous phase flowrate that will be used during the experiments. The results are shown in Figure 3.16, and show that the maximum expected differences occur at pure C_{10} or CO_2 flow with +/- 0.025 µl/min. The steps to calculate the flowrate will be shown in Appendix A.

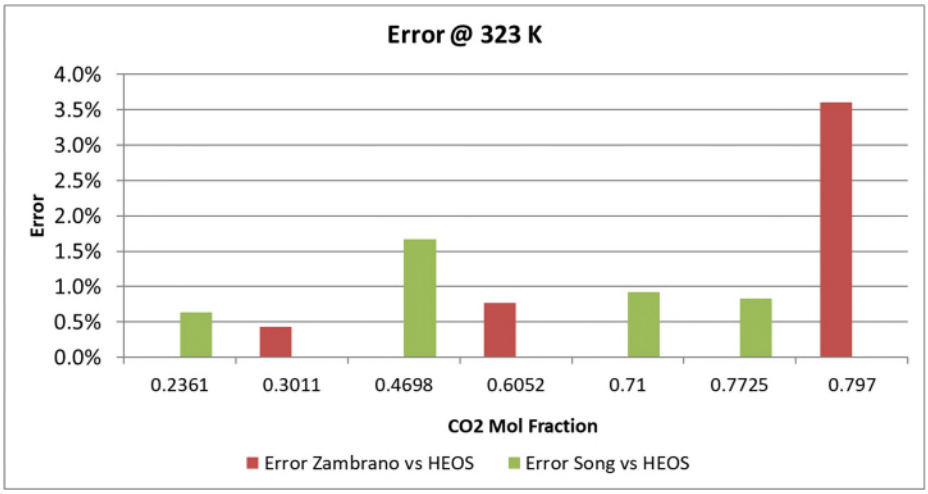

Figure 3.14 Error between HEOS and experimental data at 323 K

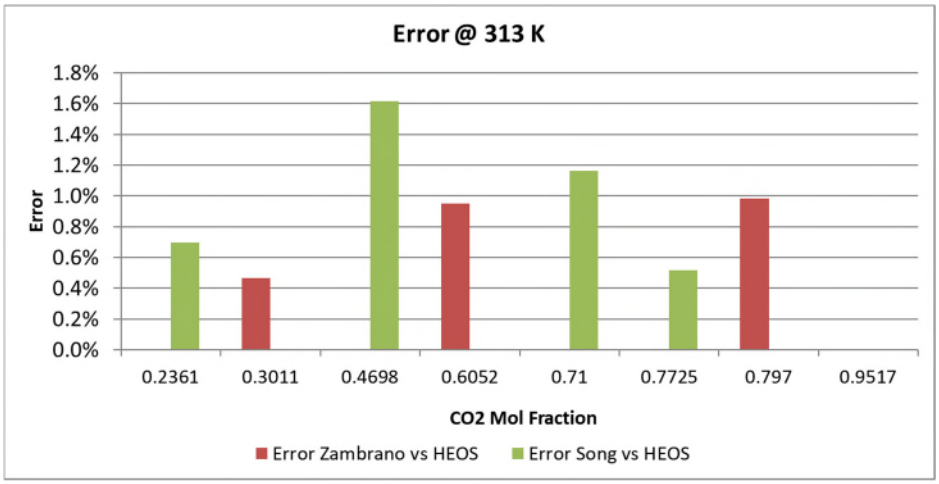

Figure 3.15 Error between HEOS and experimental data at 313 K

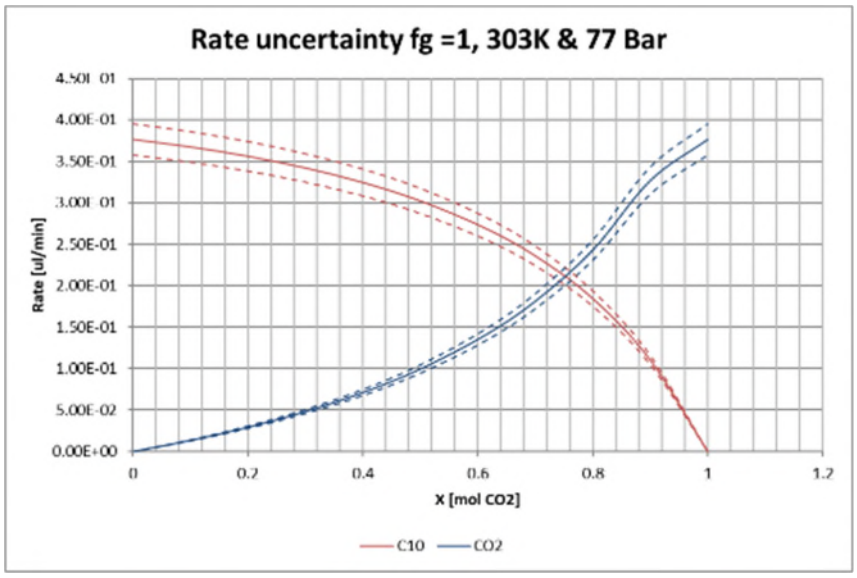

Figure 3.16 Flowrate uncertainty at 200 ft/day for f_g=1 .

3.2.6 Non-aqueous phase mixing analysis

Mixing in microfluidics is challenging since the flow is laminar with very low Reynolds numbers. The dominant factors in mixing are time, length and diffusion coefficient as described in section 3.1.2**Error! Reference source not found.**. The fact that the experiment is conducted at the micro-scale and low speeds results beneficial for mixing. It is expected that miscibility between CO_2 and C_{10} is achieved by diffusion in the capillary tubes before arriving to the microchip entrance. The possibility of achieving miscibility is supported by Liu et al. (2016), where evidence that at conditions close to the experimental conditions CO_2 the diffusion coefficients can be in the order of 10^{-10} m^2/s in bulk CO_2 - n-Decane solutions. Furthermore, Farajzadeh et al. (2007) found that at initial stages of natural convection, CO_2 mass transfer is enhanced, and the diffusion coefficient can reach values of 10^{-8} m^2/s, vindicating even more the presupposition of achieving miscibility of CO_2 and Decane in the capillaries. A small sensitivity analysis to the diffusion coefficient is presented in this section. Figure 3.17 shows the Reynolds and Peclet numbers for three different diffusion coefficients and different velocities, the values are shown in orders of magnitude to show how large variations affect mixing properties.

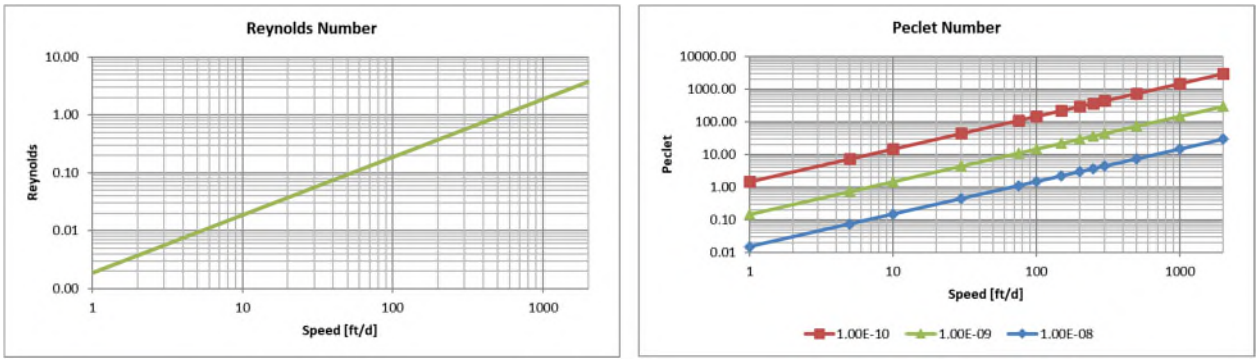

Figure 3.17 Reynolds and Peclet number sensitivity analysis for different diffusion coefficients

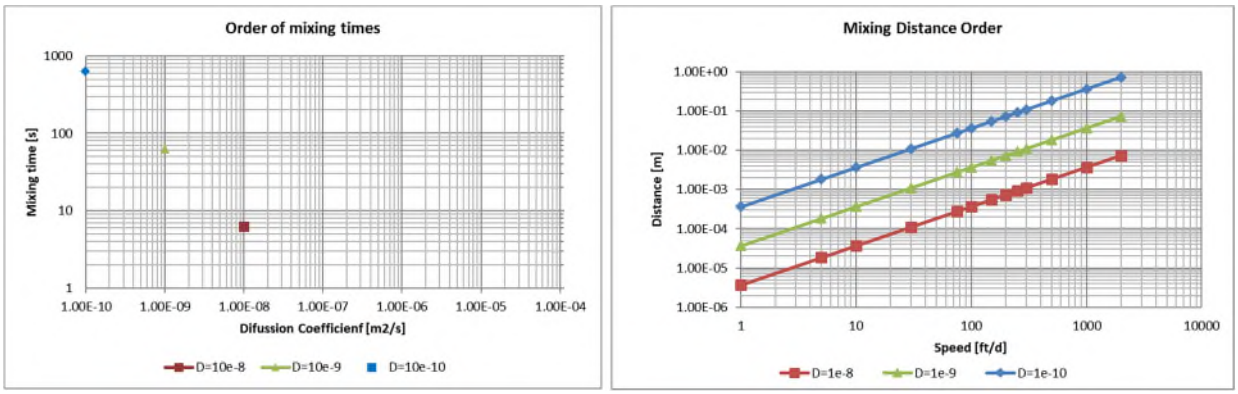

Figure 3.18 Sensitivity of mixing order time and distance for different Diffusion coefficients

The mixing times can vary from fractions of minute to fractions of hour, as shown in Figure 3.18. Likewise, the mixing distance significantly increases with smaller diffusion coefficients. However, optimistic results are observed, for a speed of 200 ft/d the distance varies from tenths of centimeters to less than mm, which are in accordance with the lengths of the system. The diffusion coefficient is the most important parameter in the mixing analysis as it will determine whether a fully miscible mixture can be achieved, but it is expected that at microfluidic scales, the system length will be enough to reach miscibility.

3.2.7 Experiment velocity set point

Velocity is one of the variables that have effect on scaling numbers such as Reynolds or capillary numbers. Although scaling numbers should remain comparable in experiments done at different scales, the fact that velocity in microfluidic experiments is too high results in a capillary number orders of magnitude larger than core or field scales. Furthermore, the Reynolds number at microfluidic scale indicates that flow is a creeping flow, i.e. Reynolds close to 0.

Core flood experiments are done at ft/d velocity regimes; however, this is not easily achievable in microfluidics due to the low flowrates that can fall out of the equipment specifications. The flowrates are obtained with the combination of syringe volume and pump specifications. Table 3-2 gives the pump speed specifications (pumps used in the experiment) and Table 3-3 provides the volumetric performance for the different syringes available in the laboratory. The 0.1ml and 0.25 ml syringes do not meet the 77 bar pressure requirement for the experiment, hence, these syringes will not be considered. From the usable syringes, the 2.5 ml syringe provides the lowest flowrates.

Harvard Pump		
	Min	Max
Speed [mm/min]	0.36	190.8
Max Force [lb] [N]	200	889.644

Table 3-2 Harvard Apparatus PHD Ultra 4400 pump specification

Syringe [mL]	Type	ID [mm]	Min Rate [miuL/min]	Max Rate [miuL/min]	Pressure Rating [Bar]
0.1	Glass	0.461	6.01E-05	31.85	69
0.25	Glass	2.3	1.50E-03	792.73	34
2.5	Steel	4.851	6.65E-03	3526.39	103
8	Steel	9.525	2.57E-02	13595.60	103
20	Steel	20.5	1.19E-01	62976.13	

Table 3-3 HA PHD 4400 Pump - Syringe combinations performance

The minimum speed at which the experiment can be run is determined by the lowest flowrate required. The most challenging case will be in the low-quality regime with low CO_2 molar fractions. Figure 3.19 shows the scenario for $X_{CO2}=0.1$, which requires the experiment's minimum CO_2 flowrate; The scenario is pessimistic if the CO_2 dissolution in brine is not considered. Nonetheless, even if CO_2 dissolution is considered, the minimum speed remains in the same order of magnitude. The dotted black line in Figure 3.19 shows the smallest flowrate required in the experiment, while the colored lines present the attainable speeds using the 2.5 ml syringe. From this figure the minimum speed at which all qualities and CO_2 molar fractions are achievable is 200 ft/d. Hence, this will be the total velocity used in the experiments.

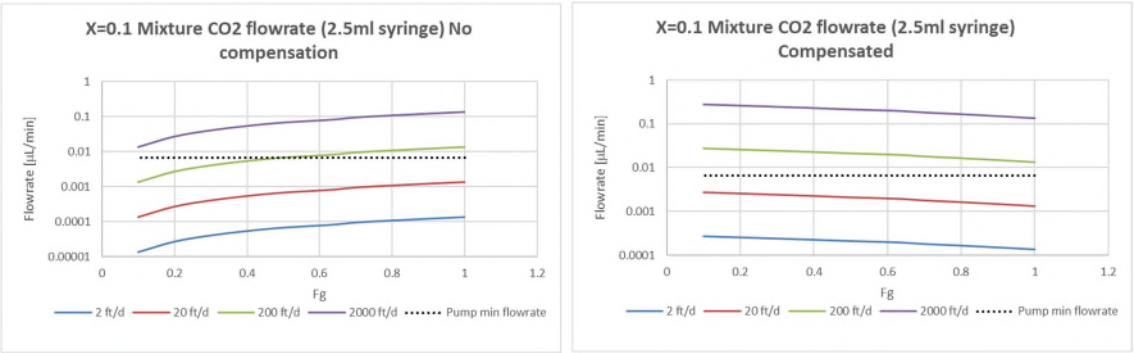

Figure 3.19 CO2 flowrate with 2.5 ml syringe. (Left No CO2 dissolved in brine. Right CO2 dissolved in brine compensated)

The microfluidic experiment will be conducted at speeds two orders of magnitude larger than core level experiments, such as those in Kahrobaei et al. (2017). The high velocity implies that the capillary number of microfluidic experiments is not comparable to core experiments.

3.3 Experimental Output

As previously stated, one of objectives of the project is to analyze how compositional changes in the CO_2-C_{10} mixture and surfactant affect foam properties. To achieve this, the three fluids will be passed through the microfluidic chip at constant total flowrate. The conditions at which fluids will be injected are presented in Table 3-4.

Parameter	Value
Pressure [bar]	77
Temperature [k]	303
Speed [ft/d]	200
Volume [µl/min]	0.3768

Table 3-4 Experimental set points

The experiment will be conducted with the philosophy of foam scans. For a fixed molar fraction, several foam qualities will be tested in a random sequence. The non-aqueous phase and surfactant rates are calculated according to Table 0-1 Volumetric flowrates formula and the specific C_{10} and CO_2 flowrates according to Equation 3.4.6, Equation 3.4.8 and Equation 3.4.9.

During the foam scans, a handful of issues related to microfluidics operation and materials were found. Because of these experimental setbacks, the foam scans did not perform in a way, that even qualitative comparisons could be done with Kahrobaei et al, (2017) experiments. Section 3.3.1 presents the problems and attempted solutions.

Table 3-5 presents the summary of the tests, which are conducted in this study.

Test Number	X_{CO2}	f_g	Total velocity [ft/d]
1	100	67	200
2	100	50	200
3	100	90	200
4	100	50	200
5	100	10	200
6	100	80	200
7	100	20	200
8	100	80	200
9	100	20	200
10	90	20	200
11	80	80	200
12	80	63	2000
13	80	20	2000

Table 3-5 Experiments summary

3.3.1 Experimental setbacks

3.3.1.1 Pressure instability

During the microfluidic experiments, it was impossible to reach steady state pressure profile. Figure 3.20 presents the comparison between foam flood experiments done in the microfluidic set-up to those conducted in cores.

Figure 3.20A presents the pressure gradient history of the microfluidic experiment of pure CO_2 with quality of 0.67. Figure 3.20 B is the pressure gradient history of the microfluidic experiment with miscible mixture of CO2-C10 with a CO_2 molar fraction of 0.80 and quality of 0.80. Figure 3.20 C shows a foam scans done at core-scale for different non-aqueous phase compositions (X_{CO2}), at a fixed non-aqueous phase quality of 0.50. The main observable difference between Figure 3.20 A, B and C is the inability of the microfluidic system to reach a steady-state pressure profile. As shown in Figure 3.20 C, the expected behavior during a foam scan is given by different stages, that can be identified by slope changes, i.e. no foam followed by foam generation and finally, steady state. Foam generation occurs when the pressure drop starts increasing, (viscosifying effect) and is reflected by a "constant" slope increasing pressure drop. This stage is followed by a steady-state pressure drop.

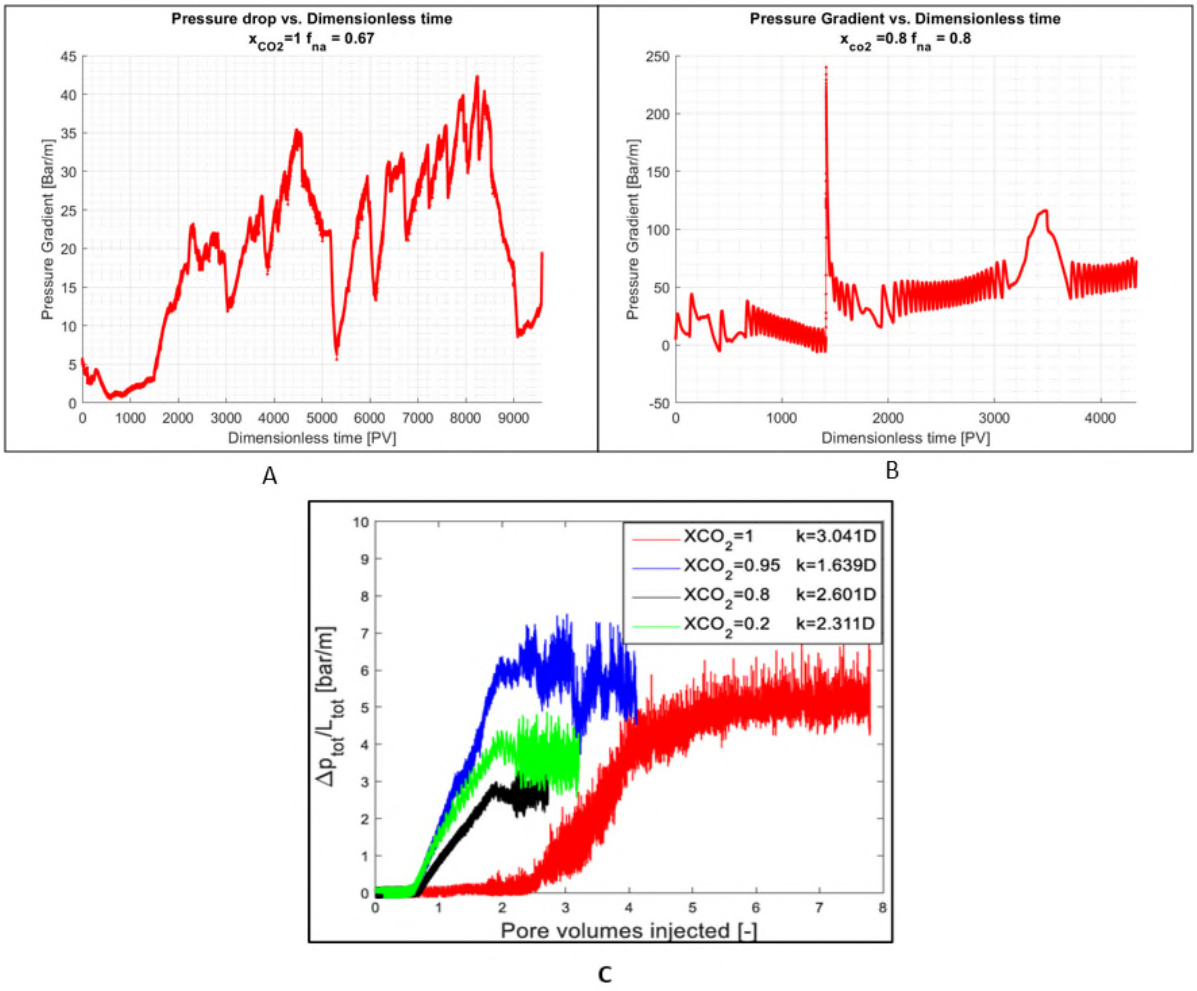

Figure 3.20 Foam scans: Pressure drop as a function of pore volumes. A,B microfluidics; C core flood (Kagoro, 2017)

On the other hand, in the microfluidic experiments, as shown in Figure 3.20A, the sudden increase in the pressure gradient after 1800 PV of injection can be interpreted as foam generation. However, it can be noticed that a steady state profile is never achieved. The pressure gradient increases from 1500 PV until 4580 PV when a considerable pressure gradient drop occurs. The pressure gradient drop occurs until 5300 PV where foam generation can be observed again. This pattern, of pressure drop fluctuation is repeated from 5300 PV to 8380 PV. At this PV, another considerable pressure gradient drop is observed followed by foam generation again.

Foam behavior in Figure 3.20B as opposed to Figure 3.20A does not exhibit either foam generation or steady state. Even more, at the early stages, around 1300 PV, negative pressure drop is observed, suggesting either a leak or back flow has occurred. The leak was ruled out by performing a pressure test after the experiment was finished. Hence, the explanation for this negative pressure drop is a back flow. The causes of back flow will be discussed

further in this chapter, as they represent one of the challenges faced during CO_2 foam tests in the microfluidic set up.

Figure 3.20 A and B show how foam scans done in microfluidic devices are rather unpredictable and steady state is never reached, condition that must be fulfilled to conduct a foam quality scan. Although, rheology is expected differ from core level experiments, due to the nature of the porous media, scales and velocities, it was expected to achieve steady state so that foam could be characterized.

Whilst conducting the experiments, one of the main concerns was the inability to generate constant and stable mixing at the microchip entrance. The observed behavior was dominated by fluids arriving at the microchip entrance in slugs. This problem will be presented in the next section. One of suspected reasons that caused the pressure gradient fluctuations reported in this section, is the sluggish behavior observed at the microchip entrance.

3.3.1.2 Sluggish fluid behavior

Throughout the experiments it was common to see batches of the non-aqueous phase and aqueous phase arriving at the microchip entrance in random slugs. Typical slug arrivals are shown in Figure 3.23 and Figure 3.25, where the snapshots shown are taken at the microchip entrance whenever the phase entering the microchip changes. The dimensionless time corresponding to the displayed snapshot is indicated at the bottom of the snapshot. Every phase alternation is denoted by a letter that refers to a dimensionless time. The times are then correlated to positions in the pressure gradient history, shown in Figure 3.22 with vertical dashed lines marked on top by the corresponding letter.

The pressure instabilities described in section 3.3.1.1 are observed again in Figure 3.21, which corresponds to the test with $x_{co2}= 1$, and $f_{na}= 0.50$, where fluctuations in pressure at several dimensionless times can be observed. As mentioned, these pressure instabilities are thought to be caused by random slugs arriving at the microchip entrance. It can be noticed that between 1971 PV and 3000 PV a full cycle of pressure build down and subsequent build up occur. By looking at what is happening at the microchip entrance during this interval, it is possible to correlate the pressure behavior. Figure 3.22 shows the zoomed pressure response for this interval. During this interval, corresponding to 18 hours, images were captured every 5 minutes using 20x magnification. A subset of these images is presented in Figure 3.23.

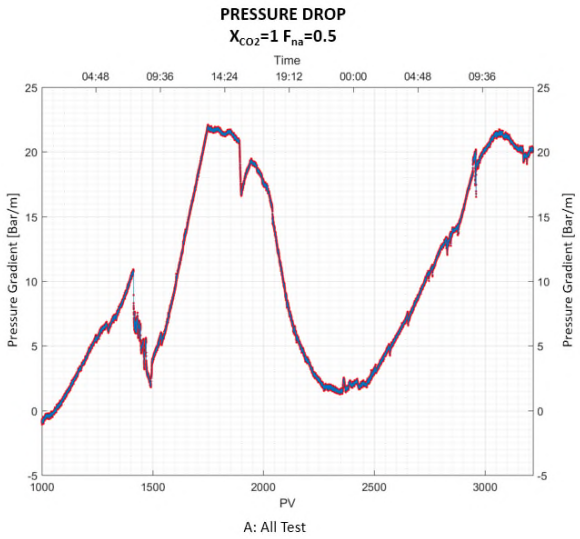

Figure 3.21 Pressure drop behavior for all Test 2: X=1, Fg=0.5

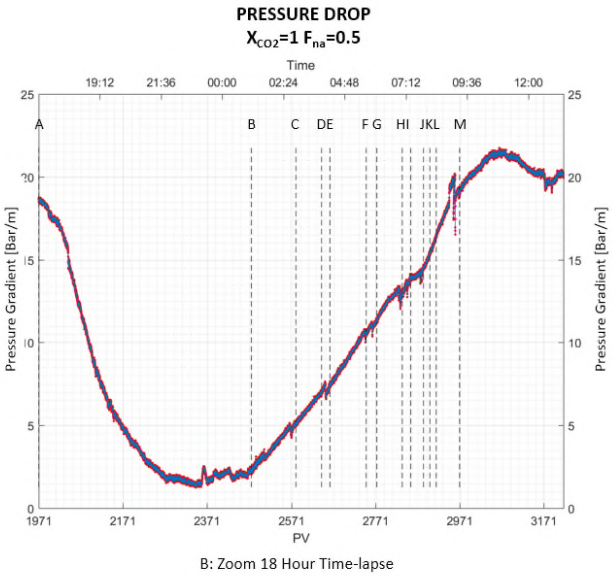

Figure 3.22 Pressure drop zoom for Test 2: X=1, Fg=0.5, showing intervals at which fluid changes are seen in the microscope

By looking at the vertical dashed lines and its corresponding pressures in Figure 3.22, a sluggish behavior is not easily detected. However, the slugs are observed using the microscope and they suggest that pressure response is not immediately altered by slugs per se, though their size has significant impact. Each slug interacts with the fluid downstream and this interaction is the main driver in the pressure response.

If a constant flowrate in the system is assumed, timing the duration of each slug will indicate the volume of each phase entering the system. Therefore, given the total flowrate and non-aqueous phase quality, the phase volumes that should be entering the system can be compared against those observed. This will indicate if the slugs honor the test design. If this occurs, a reliable mixing can be proved, and the nature of the pressure fluctuations can be further analyzed.

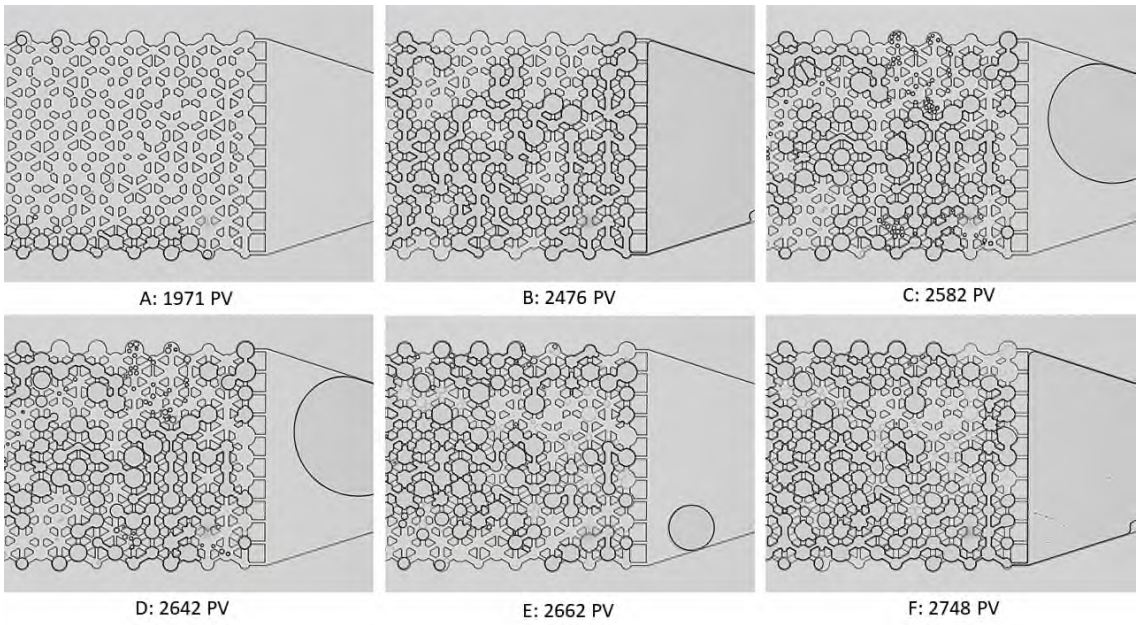

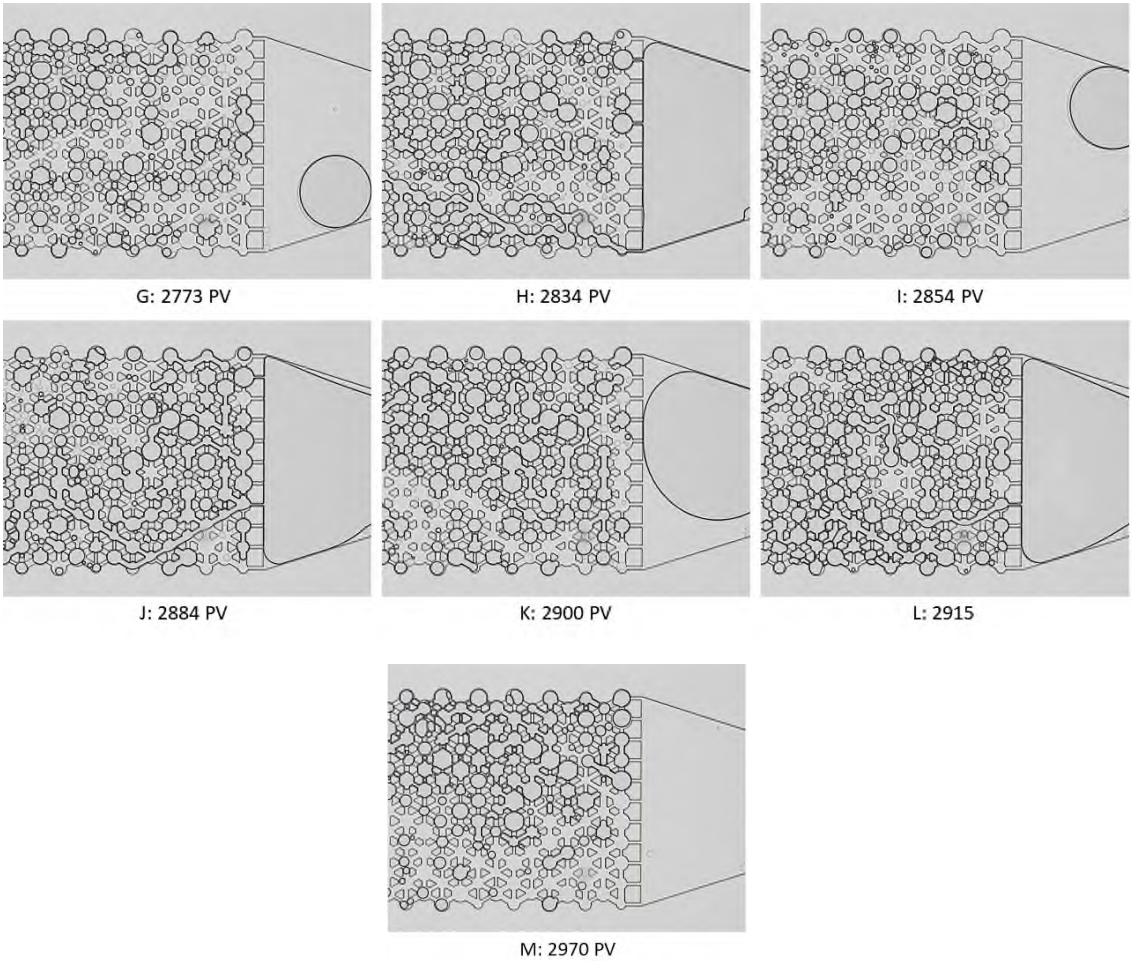

Figure 3.23. Test 2 Time lapse. A-M Images exhibit the time at which phase alternation occurs. Images taken at 20X zoom.

Based on the nature of the slug entering the porous media (Figure 3.23) Table 3-6 presents on the first and second columns the image letter and the corresponding dimensionless time. The third and fourth columns show the volume entering the media. This volume it's either attributed to aqueous or non-aqueous phase depending on the phase entering the system as observed with the microscope. The phases are distinguished by their color, which is clearer for water than CO_2.

Frame	PV total	Δ aqueous PV	Δ non-aqueous PV
A	1971	505	
B	2476		106
C	2582	60	
D	2643		20
E	2663	86	
F	2749		25
G	2774	61	
H	2834		20
I	2855	30	
J	2885		16
K	2900	15	
L	2915		55
M	2970	112	
End of lapse	3082		
Total phase PV		869	242

Gas to total volume ratio	0.2

Table 3-6, Dimensionless time at which phases alternate in Figure 3.23

The non-aqueous to total volume ratio presented in the preceding table, is equivalent to the non-aqueous phase quality for the given time interval. It is expected that the slugs honor the injection quality, given that the total time is more than 1000 PV, nonetheless based on the observation this is not occurring. The gas ratio calculation done in Table 3-6 can be considered unsound as it assumes that the fluid entering the porous media is single phase, the observed behavior suggests that in order for a CO_2 bubble to enter the porous media, it should be large enough to be squeezed across the width of the microfluidic chip as shown in Figure 3.23 B,F,H,J,L. This is further justified by the non-aqueous bubble seen in Figure 3.23 C and D, upstream the pore network inlet, that remains almost stationary while the aqueous phase flows around, the bubble is finally pushed into the pore network in frame D.

The pressure zoom presented in Figure 3.22, suggests that the slugs do not have correlation with the pressure gradient, however, between frame A and B, 505 PV of surfactant enter the pore network, the foam previously inside the porous media gets pushed out and the pressure drop decreases until gas starts entering again in the porous media at frame B, where pressure starts building up again, indicating that foam is being created downstream in the microchip. This indicates that the size of the slug is indeed vey related to pressure drop, furthermore it depends on its size and the phase the slug will encounter downstream.

Since the test is set *at* $f_{na}=0.5$, it would be expected to see slugs similar in size or interval as discussed previously. In contrast, randomness in slugs appearance is recorded. The difference between the expected gas volume ratio of 0.5 and the observed of 0.2 indicates a large deviation, that can be attributed to the time lapse not capturing small bubbles entering the system, however, the difference is around 60% and it is unlikely to be attributed to small CO_2 bubbles not captured by the timelapse.

The experiment shown above does not represent an exception, instead, this was the norm. This behavior suggests that the gas might be taking a different path within the set-up or it is being accumulated somewhere downstream the microscope or there is a leak. While the first option is difficult to proof as the CO_2 will evaporate as soon as the pressure is reduced, the other two options were tackled using two approaches:

- Extended pressure test to identify any leakage.
- Changing the non-aqueous phase–surfactant mixing device to ensure better mixing.

The pressure test was repeated with no indication of fluid leaking. Therefore, since no leak was detected, the second approach was implemented. Initially, both fluids contacted each other using a normal microfluidic T-union. To ensure a better mixing the T-union was replaced with a T junction designed for mixing microfluidic applications.

The test presented in Figure 3.24, was conducted after introducing the mixing T-junction. The test conditions were $x_{CO2}=1$ and $f_{na}=0.8$. The pressure response for the entire experiment is presented in Figure 3.24A. Figure 3.24B magnifies the final 50 PV of injection. Again, the vertical lines indicate the moment at which a fluid alternation occurs. It can be seen from Figure 3.24A that similar to previous experiments, there is no sign of a steady-state pressure profile even after injection 1500 PV.

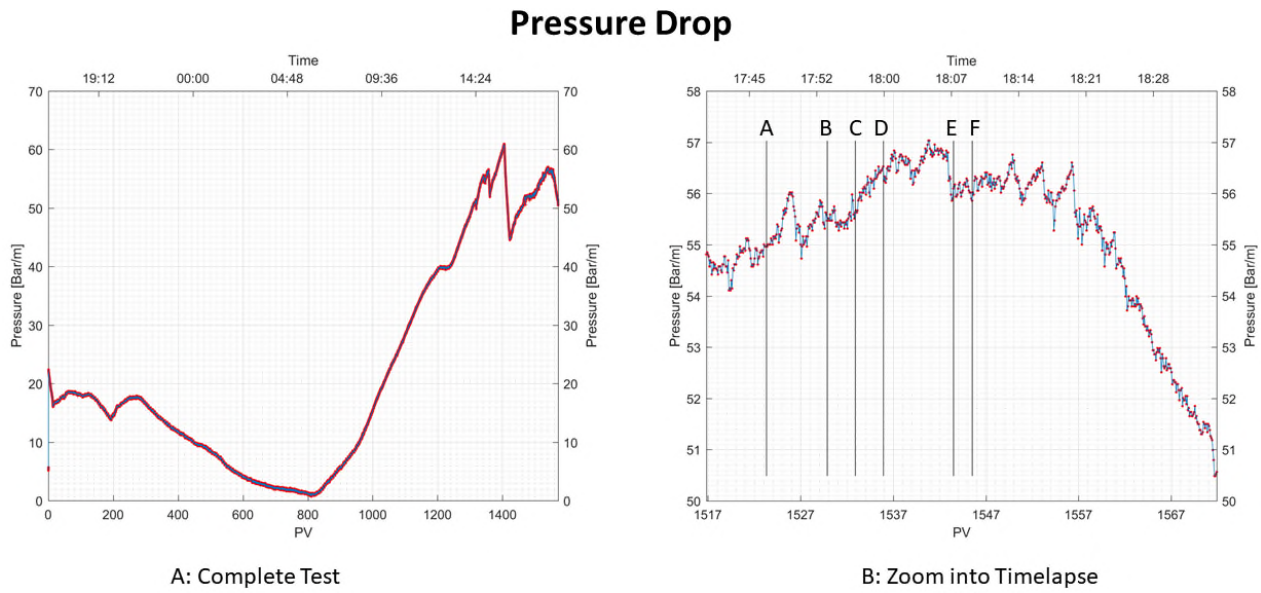

Figure 3.24 Pressure behavior for Test 2: X=1, Fg=0.8

Figure 3.25 shows the images taken at the PV's indicated by the vertical black lines shown in Figure 3.24 B. The images for the time lapse referred in this experiment are taken at 30 sec. intervals, i.e. for a preestablished time length, pictures are taken at a fixed location at regular time intervals, this case 30 sec. The images in Figure 3.25 A-F show the phases arrival after the implementation of the mixing device. The presence of some pre-generated foam at the pore network entrance, as in frame E and F, as well as smaller intervals between slugs, reveal to some extent improvement. However, slugs are still noticeable, and the foam pre-generation is not consistent throughout all the tests performed afterwards. The randomness of the slugs, even after the introduction of the T-junction, indicate that phases arrival needs to be controlled better. And this remains as one of the main challenges of the experimental set up improvement.

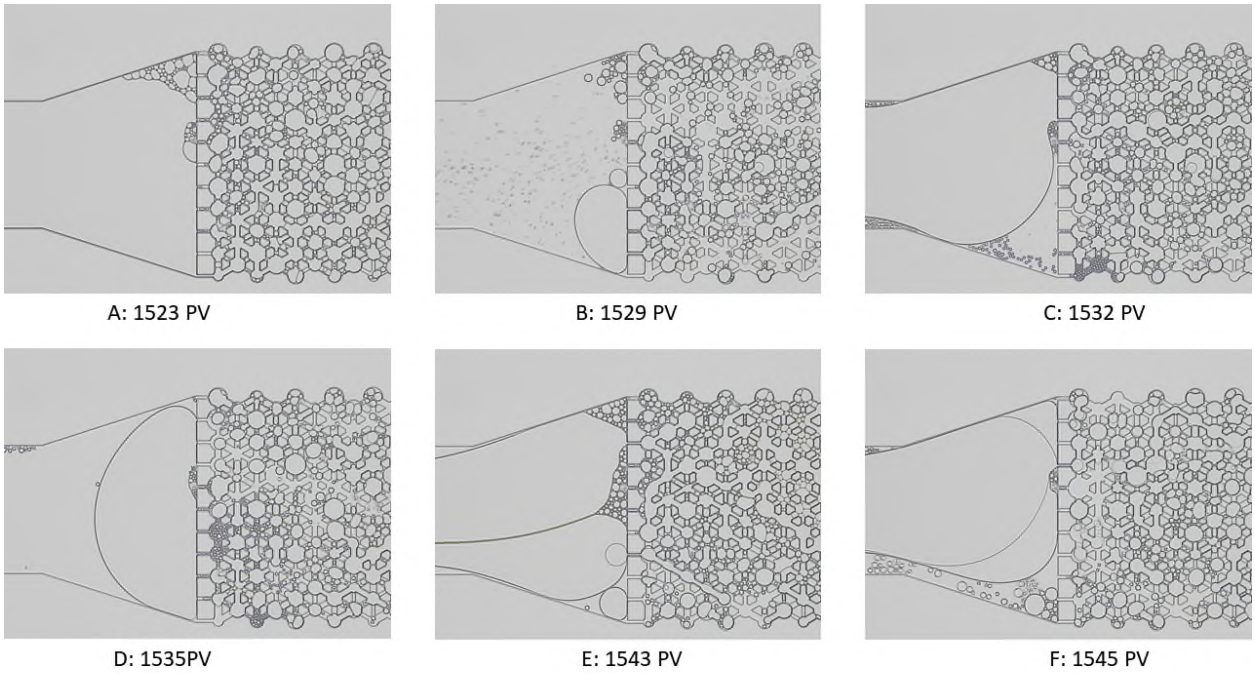

Figure 3.25 Test 6 Time lapse. A-F Images that exhibit the time at which fluid alternation occurs.

As shown throughout this chapter, the pressure fluctuations yield to difficulties in stablishing a reliable behavior of the supercritical foam.

3.3.1.3 Back flow

Throughout the experiments one common setback observed was backflow. Figure 3.26 shows the pressure history of two different experiments, Test 4 and 7, which experienced negative pressure gradients. These negative pressure gradients, which are indicated by blue ellipses in Figure 3.26, are interpreted as back flows. It is important to mention that several experiments conducted in this study showed this type of behavior. Test 4, shown by Figure 3.26A, experienced a minor backflow at 2000 PV, which was vanished quickly. However, in Test 7, shown by Figure 3.26AB, there was a sever backflow occurred at 750 PV and continued for the next 500 PV of injection.

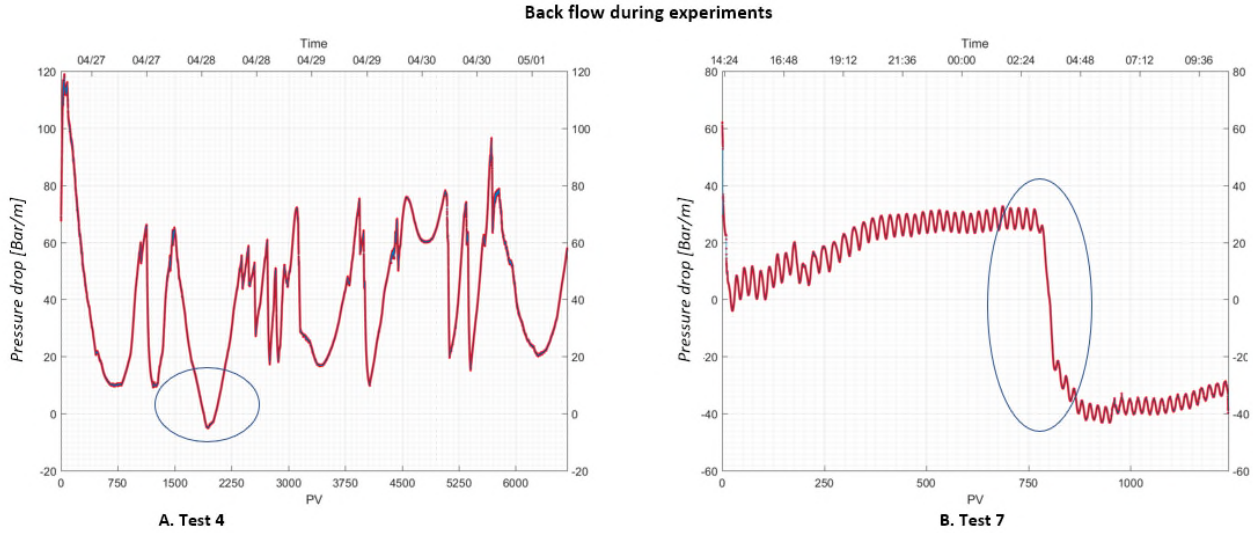

Figure 3.26 Backflow during experiments

The backflow was mainly attributed to fluid leaks at the CO_2 2.5 ml syringe caused by corrosion in the plunger. This issue is discussed further in the next subsection.

3.3.1.4 Corrosion in 2.5 ml syringe

During the troubleshooting attributed to backflow, it was found that the CO_2 syringe had evidence of fluid leak as shown in Figure 3.27. Additional troubleshooting revealed that 2.5 ml stainless steel syringes are not labeled as gas tight. Nonetheless, the seal manufacturer doesn't restrict the use of the seal with gases.

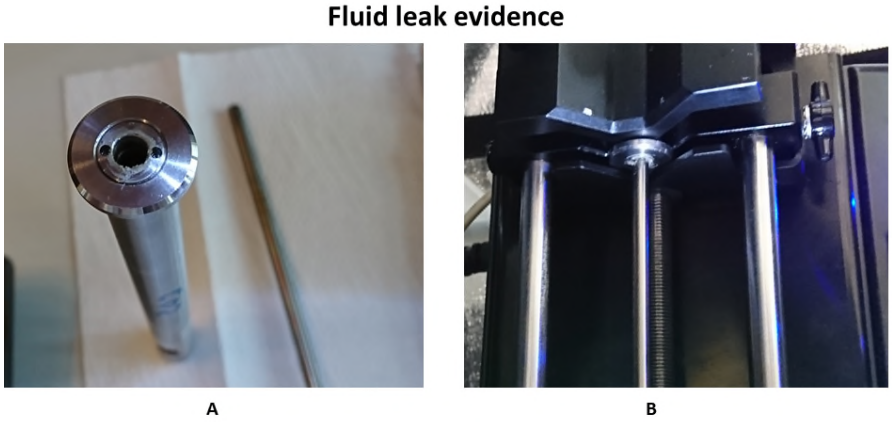

Figure 3.27 Fluid Leak Evidence. A Barrel. B Plunger

Following the evidence of a leak, further testing on the syringe was conducted and, strong corrosion evidence was found as shown in Figure 3.28. Examining the syringes revealed that the 2.5ml syringes plungers were manufactured using a non-corrosion resistant steel. This created leak paths in the plunger. Due to the problems encountered with the sealing, the 2.5 ml syringes were replaced with the 8 ml syringes which use O-rings as sealing mechanism instead of static/face seals.

Figure 3.28. Corrosion in 2.5 ml syringe plunger

3.3.1.5 Pump stalling

Due to the corrosion issues and multiple sealing problems encountered with the 2.5 ml syringes, it was decided to replace them with the 8 ml syringes. The effect of changing the syringes is related to the attainable rates i.e. tests with CO_2 molar fraction below 0.1 are unattainable using 8ml syringes. Nonetheless, experimental test showed that rates were not the only issue. A problem related to pump force arose, whereby CO_2 pump would stall due to force limitations. Although theoretically, using the 8 ml could provide a pressure of up to 125 bar, the observed behavior indicated that this limit could not be reached with pump stalling occurring before reaching 100 bar as illustrated by the blue pressure line, representing the Pin sensor (microchip entrance), before 200 PV in Figure 3.29. The time elapsed from the maximum pressure after 200 PV until approximately 1060 PV is the pressure response in the system with the pumps stalled.

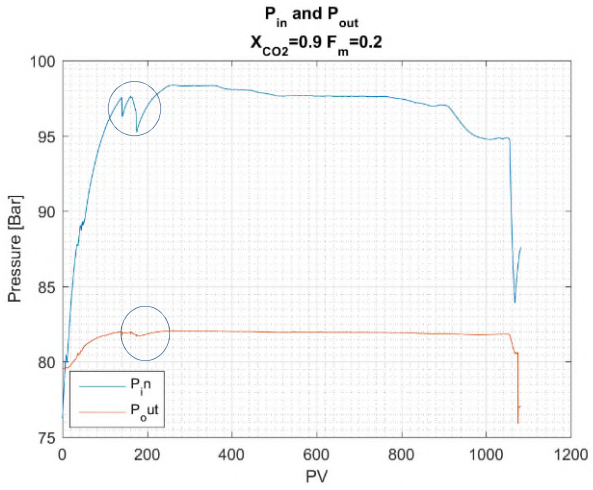

Figure 3.29 Pressure response during pump stalling

While troubleshooting it was found that 8 ml syringe O-rings would swell under the presence of CO_2 increasing the friction between barrel and plunger and therefore limiting the achievable pressure. In consequence, it was difficult to maintain a reliable mixing rate due to constant pump stalling. It was not possible to overcome this issue due to CO_2 resistant O-rings availability.

Since it was rather difficult to get constant flow using the syringe pumps, it was decided to use different pumps. The new pumps used during this stage were Quizix pumps, however, these pumps were only capable of delivering rates in the order ml/min, which led to an increase in the pressure drop over an already pressure limited set-up. Furthermore, because of higher injection rates, these pumps lowered the chances of achieving mixing by means of diffusion and even larger alterations in capillary, Reynolds and Peclet numbers.

The experiments performed with the Quizix pumps were limited by the pressure rating of the microfluidic chip which was limited to 95 bars to limit the risk of bursting the chip. Due to this pressure limitation, pumps didn't reach constant flows, as they were constantly halted by the safety pressure alarms.

3.3.1.6 Debris particles

Since the microfluidic set up is placed in a non-clean environment, the chances of introducing dust particles in the system are high. These dust particles accumulate at the microchip entrance clogging the microchip entrance. Figure 3.30 shows accumulation of debris particles at the microchip entrance.

As dust particles accumulate at the entrance, the microchip starts getting clogged affecting the pressure response of the system. To mitigate this, an in-line filter was placed prior the microchip entrance. Although the conditions improved, it was rather difficult to fully mitigate the issue. As stated, since the set up isn't placed in a clean environment, debris particles are introduced at early stages of the system rig-up. Furthermore, it was noticed that debris particles accumulated in the capillary tubes as the experiments were conducted. Even though several attempts to flush out the particles we attempted, it was impossible to achieve a debris-free set up.

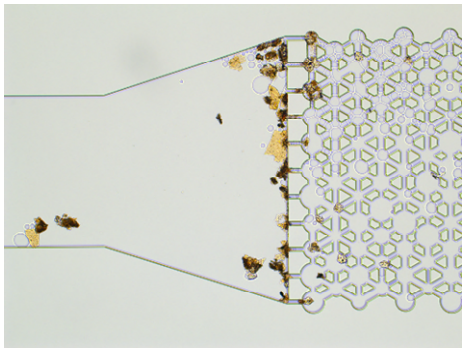

Figure 3.30. Debris particles clogging microchip entrance

3.3.1.7 Thermal fluctuations

Thermal fluctuations cause expansion and contraction of CO_2 within the setup. Since the volume in the syringe pump is more than 30x the volume in the capillary tubes (upstream the microfluidic chip) and microchip combined, the impact of its volumetric change considerable. Table 3-7 shows that departing from experimental conditions (303 *K* and 77 *Bar*) a 1 *K* temperature difference will produce 91.7 μl variation in syringe volume, attributed to the large isobaric expansion coefficient of CO_2. The observed consequence of these thermal fluctuations are backflows as shown in section 3.3.1.3, that resulted in flow control loss and therefore, non aqueous phase composition and foam quality alterations.

Figure 3.31 bottom shows the temperature variations during an experiment. The variations are 1 °C around the set point every 40 PV or approximately 40 minutes. Figure 3.31 top shows the pressure response in the gauges at the CO2 pump, chip inlet and chip outlet. From the three pressures monitored, it can be seen that the yellow curve, that corresponds to the pressure at the microchip outlet is not affected by the variations in temperature as the gauges upstream. This is mainly due to the fact that pressure downstream the microchip is controlled by the back pressure, which is regulated using nitrogen contained in a very large reservoir. This large reservoir can rapidly compensate for pressure losses (due to the regulating valve at installed in the nitrogen tank) but not for pressure increases. The overall effect downstream the microchip is a pressure insensitive to CO_2 fluctuations. On the other hand, the pressure response at the CO2 pump and the chip inlet follows the temperature fluctuations pattern. These fluctuations are about XX bar.

Property	Value
Temperature [K]	303
Pressure [Pa]	7.7×10^{6}
Isothermal expansion coefficient [1/K]	3.67×10^{-2}
Syringe Volume [µl]	2500
Volume variation in syringe [µl/C]	91.7
Chip volume [µl]	0.38
Dead volume from syringe to chip [µl]	75

Table 3-7 Thermal expansion inputs

This issue was tackled by both, limiting the opening of the box containing the setup that provides thermal insulation, and setting the temperature inside the box slightly above the maximum daytime temperate of the laboratory.

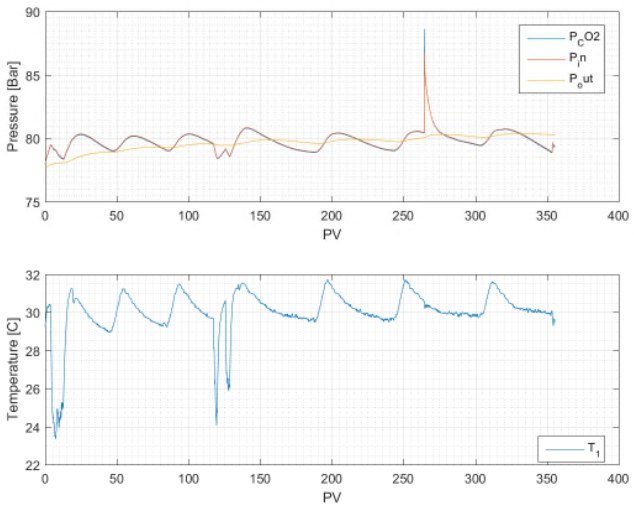

Figure 3.31 Example of temperature and pressure fluctuations around the set point

3.3.1.8 **Experimental risk matrix**

The combination of the experimental setbacks and lessons learnt whilst preparing and conducting the experiments creates the baseline for a risk assessment, which is presented in Table 3-8.

		Severity				
		1	**2**	**3**	**4**	**5**
Likelihood	**5**	- Uncertainty in mixture density estimation will cause uncertainty in flowrate calculations. - Large dead volumes have negative impact in time to replace fluid between experiments.	- Uncertainty in pump flowrate will cause uncertainty in foam quality and mixture molarity.	- Exceeding Syringes rating will syringe cause bursting. - Exceeding microfluidic chip rating will cause bursting. - Dust will clog the microfluidic chip entrance channels.	- Thermal expansion of CO_2 will cause flowrate fluctuations, resulting in unreliable quality and mixture calculations. - Corrosive nature of experimental fluids will Create debris particles that Will clog the set up and damage equipment.	- Unpredictable arrival of phases at the microchip entrance resulted in slugs that impede steady state of foam.
	4					
	3					
	2				- Differences in flow restriction between capillary tubes and microfluidic chip may result in fluids taking the wrong way resulting in undesired flow paths. - Decane n-C10 and CO_2 may not mix and will not become a single phase flow.	
	1					

Very High **High** **Medium** **Low**

Table 3-8. Experimental Risk assessment

The risk is a product of the probability of occurrence and severity of consequences. To aid visualization of risks, the matrix is displayed using a color based labeling, where red shows the highest risk and green the lowest. The benefit of categorizing risks is that it provides a priority based approach, that will prioritize the issues that can have potential impact on equipment, personnel safety and reliability of experimental outputs. The likelihood and severity are based on guidelines provided by Citadelgroup (ANON, 2018).

From the risk assessment, three items presented very high risk, namely sluggish behavior of the phases, CO_2 thermal fluctuations and corrosion issues. They are categorized in very high as their occurrence could not be prevented and mitigation measures were inefficient. Furthermore, their occurrence proved to have strong consequences on the experimental results output.

The risks considered as high mainly deal with equipment hazards that could be tackled through experimental planning. Medium risks can be separated in two categories, likely events whose impact is minimum and unlikely events whose impact is considerable.

An issue not treated in the matrix that has great impact is safety. Due to the nature of the experiment, relative high pressures are present. It is important to always have pressure gauges and regulators at the laboratory gas outlets (air, nitrogen, etc.). In addition to the risk assessment done at the beginning of the experiments, where the procedure, operation and hazards of equipment and experiments is presented, it is recommended that the equipment used in the experiments be labeled according to its pressure rating or marked. Secondly, MSDS of the chemicals used should be printed and kept along the *Laboratory card*.

3.4 Conclusions and way forward

This document reports some attempts to conduct a miscible CO_2 foam flood in a microfluidic device. Experiments have been conducted under miscible conditions showing that foam can be created within the pore network without the aid of foam pre-generation and the few experiments conducted using CO_2-C_{10} mixtures suggested that the miscibility predictions, based on a pure diffusive process is indeed attainable.

The pressure response suggests that foam undergoes processes of lamellae creation and destruction within the porous network nonetheless equilibrium between both processes was not achieved. The slugs at the microchip entrance suggest that in order to achieve steady the condition of homogenous mixing is necessary; however, it is difficult to conclude it is sufficient.

At microscale, due to the presence of large dead volumes, thermal fluctuations need to be considered and the setup should be designed such that mitigation measures are put in place. Not doing this results in backflows that produce unreliable mixing. Furthermore, due to the significant larger flow restriction through the microchip as compared to capillaries, leaks should be controlled as they can have significant impact.

Due to amount of technical challenges encountered during the experiments, a handful of suggestions will be presented. These suggestions attempt to address the uncertainties and problems related to set up.

As seen from the risk matrix, the main equipment challenge encountered is related to having constant phases arrival at the microchip entrance that could guarantee reliability in the injection quality as well as potentially steady state behavior. To improve this, it is suggested to use capillary lines with the same length from the syringe outlet to the mixing point. Use of mixing enhancing devices is recommended, however, their material should be chosen wisely as they could introduce pressure limitations due to manufacturing materials.

The second biggest issue is related to temperature stabilization; therefore, it is suggested to improve the thermal insulation of the box containing the set up.

The third suggestion with regards to equipment, is to find the appropriate seals for the 2.5ml syringes i.e. gas tight and CO_2 resistant. This will remove one variables that could be the origin of the pressure artifacts encountered in all experiments. The effectiveness of dynamic seals, such as those found in the 2.5ml syringes, at very low CO_2 flowrates should be assessed.

Introducing debris particles in the system is unavoidable if the experiments aren't carried in a clean environment. Nonetheless, since this is an unlikely solution, to mitigate the impact of working in an unclean environment, it is recommended to include filters at every syringe output and prior the microchip entrance. Microfluidics manufacturers offer different types of filtering solutions, e.g. column or inline filters, the selection should be done using design criteria, which until the realization of this experiment was not considered.

To minimize dead volume, hydraulic capacitance and compressibility effects (due to bottleneck effect), it is recommended to shorten the lengths of the capillaries and use capillaries with the smallest diameter possible, 100 μm is minimum recommended, as well as to minimize changes in diameters within the setup, e.g. use smallest syringe diameter. Shortening the lengths of capillaries conflicts with the miscibility predictions, hence this has to be considered.

Finally, the implementation of a mass/flow monitoring method or device at the microchip outlet is recommended. This will enable verification of mass conservation. Devices that allow this, are found in microfluidic experiments such as those performed by Kuhlman (1990) where the back pressure support was provided by a withdrawal pump capable of measuring flow.

As far as pumps goes, it is important to choose pumps such that design criteria can be met. In this sense, Harvard syringe pumps with stainless steel syringes proved to be more suitable as they were capable of delivering lower flowrates than Quizix pumps. Nonetheless, having CO_2 requires to look into manufacturers options as chemical resistance is important, i.e. Viton O-rings for 8ml syringes.

Appendix A. Volumetric flowrate Determination

As shown in the experimental setup schematic, three separate pumps are used to inject the fluids into the microchip. The inputs for the pumps are the volumetric flows, which determine the foam quality and non-aqueous phase molar fraction. This section describes the procedure to calculate the volumetric flows. The underlying assumption is that temperature, pressure and total velocity across the microfluidic chip (Darcy Velocity) are fixed. For nomenclature see the nomenclature section at the end of the document.

The variables considered as known are: ρ_{mix}, ρ_{CO2}, ρ_{C10}, x_{CO2}, MW_{CO2}, MW_{C10}, q_{mix}. The steps shown below are presented to show how departing from the known variables the volumetric flowrates can be calculated.

The velocity in the microfluidic chip should be constant and the same for all experiments, hence the total flowrate, q_{tot}, treated as a known parameter. The other known parameters are non-aqueous phase quality, f_{na}, and molar fraction, x_{CO2}. Note that x_{CO2} represents the different compositions at which experiments are conducted.

Given the total flowrate and the non-aqueous phase quality, the surfactant solution and non-aqueous phase flowrates can be estimated using Equation 3.4.1

$$f_{na} = \frac{q_{na}}{q_{tot}} = \frac{q_{na}}{q_{na} + q_w} \qquad \text{Equation 3.4.1}$$

The outputs from Equation 3.4.1 are therefore q_{na} and q_w (surfactant solution) as presented in the following table.

q_{na}	$f_{na}.q_{tot}$
q_w	$(1-f_{na}).q_{tot}$

Table 0-1 Volumetric flowrates formula

The next step is to estimate the mass fractions of CO_2 and C_{10} in the non-aqueous phase. Given the carbon dioxide molar fraction, the C_{10} molar fraction can be determined as follows.

$$x_{C10} = 1 - x_{CO2} \qquad \text{Equation 3.4.2}$$

Subsequently, the mass fraction can be estimated using the non-aqueous phase components molar fractions and molar weights.

$$w_{CO2} = \frac{x_{CO2}MW_{CO2}}{x_{CO2}MW_{CO2} + x_{C10}MW_{C10}} \qquad \text{Equation 3.4.3}$$

Replacing Equation 3.4.2 into Equation 3.4.3 gives the carbon dioxide mass fraction based on the desired molar fraction.

$$w_{CO2} = \frac{x_{CO2}MW_{CO2}}{x_{CO2}MW_{CO2} + (1-x_{CO2})MW_{C10}} \qquad \text{Equation 3.4.4}$$

The mass flowrate is calculated considering the definition of density and flow per unit of time. As shown in Equation 3.4.5.

$$W_i = \rho_i V_i \quad \Leftrightarrow \quad \dot{w}_i = \rho_i q_i$$ Equation 3.4.5

Combining Equation 3.4.5 and Equation 3.4.4 provide the volumetric flow of carbon dioxide. The inputs come from the desired fluid velocity and molar fraction. The non-aqueous phase density is considered a known value and is estimated using the *multi-parameter Helmholtz backend equation of state*.

$$q_{CO2} = \frac{\dot{w}_{CO2}}{\rho_{CO2}} = \frac{\dot{w}_{mix} w_{CO2}}{\rho_{CO2}} = \frac{\rho_{mix} q_{mix} w_{CO2}}{\rho_{CO2}}$$ Equation 3.4.6

Applying the same principle, the Decane flowrate can be calculated considering that the n-Decane and carbon dioxide mass fractions should add 1 as shown in Equation 3.4.7. The Decane flowrate is shown in Equation 3.4.8

$$w_{C10} = 1 - w_{CO2}$$ Equation 3.4.7

$$q_{C10} = \frac{\dot{w}_{C10}}{\rho_{C10}} = \frac{\dot{w}_{mix} w_{C10}}{\rho_{C10}} = \frac{\rho_{mix} q_{mix} w_{C10}}{\rho_{C10}} = \frac{\rho_{mix} q_{mix} (1 - w_{CO2})}{\rho_{C10}}$$ Equation 3.4.8

Equation 3.4.6 considers that the CO_2 in the system will only diffuse in C_{10} however, part of the CO_2 will dissolve in brine as well. The amount of CO_2 dissolved in brine should be compensated by increasing the CO_2 flowrate such that the brine becomes saturated with CO_2. The compensation is a function of the brine volumetric flow the solubility factor based on Zhao (2012) experiments and extracted from the web application found at PennState University web page (Zhao, 2018). For a 1% NaCl weight concentration brine at 303 K and 77 bar the K value is 1.25 [mol CO_2 / Kg H_20]. The compensation volume is therefore estimated using Equation 3.4.9

$$q_{CO2\_comp} = K_{CO2} \frac{\rho_{H2O} q_{H2O} MW_{CO2}}{\rho_{CO2}}$$ Equation 3.4.9

Appendix B. Supplementary figures for Foam injection

i. Pressure profile comparing *epdry* low and high for Case 1-Communicating layers

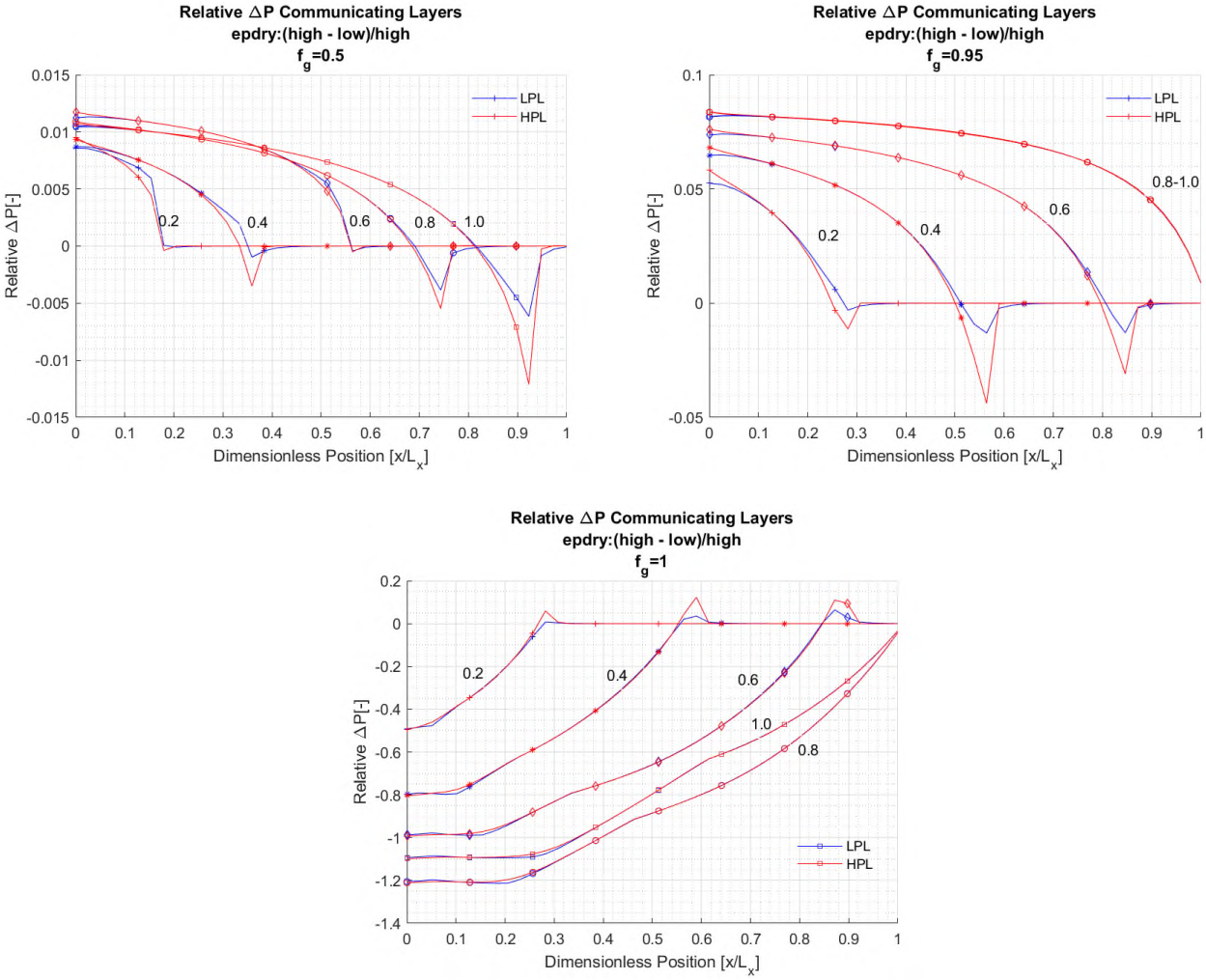

Figure 0.1 Relative pressure difference between *epdry* high and low for different injection qualities and injected volumes. Left: f_g=0.50. Right: f_g=0.95. Bottom: f_g=1.0

ii. Apparent viscosity profile comparing *epdry* low and high for Case 1-Communicating layers

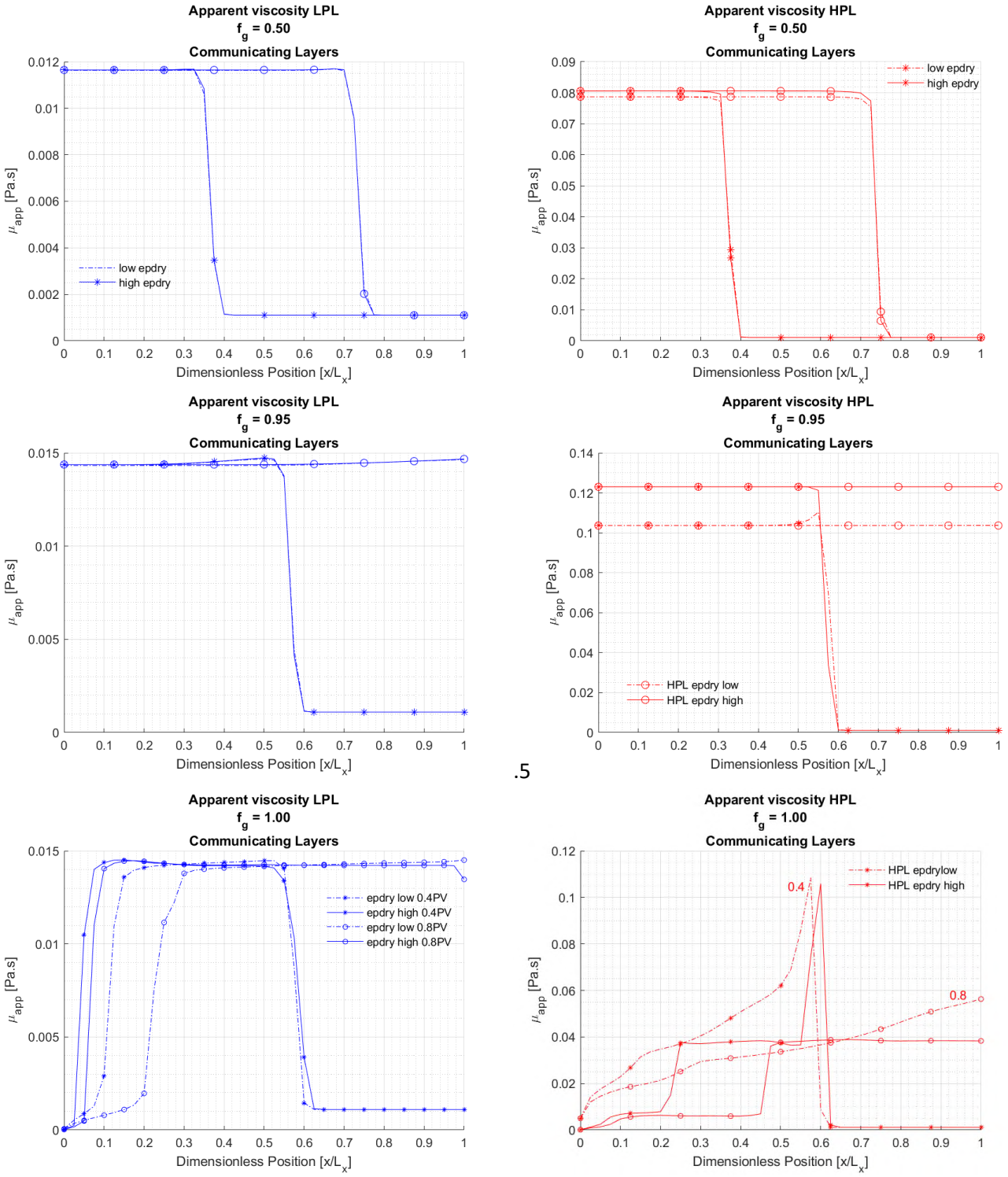

.5

Figure 0.2 Apparent Viscosity profiles for non-communicating layers for different qualities and injection volumes. Left: LPL. Right: HPL

iii. Apparent viscosity Profiles comparison for Case 2-high *fmmob* contrast

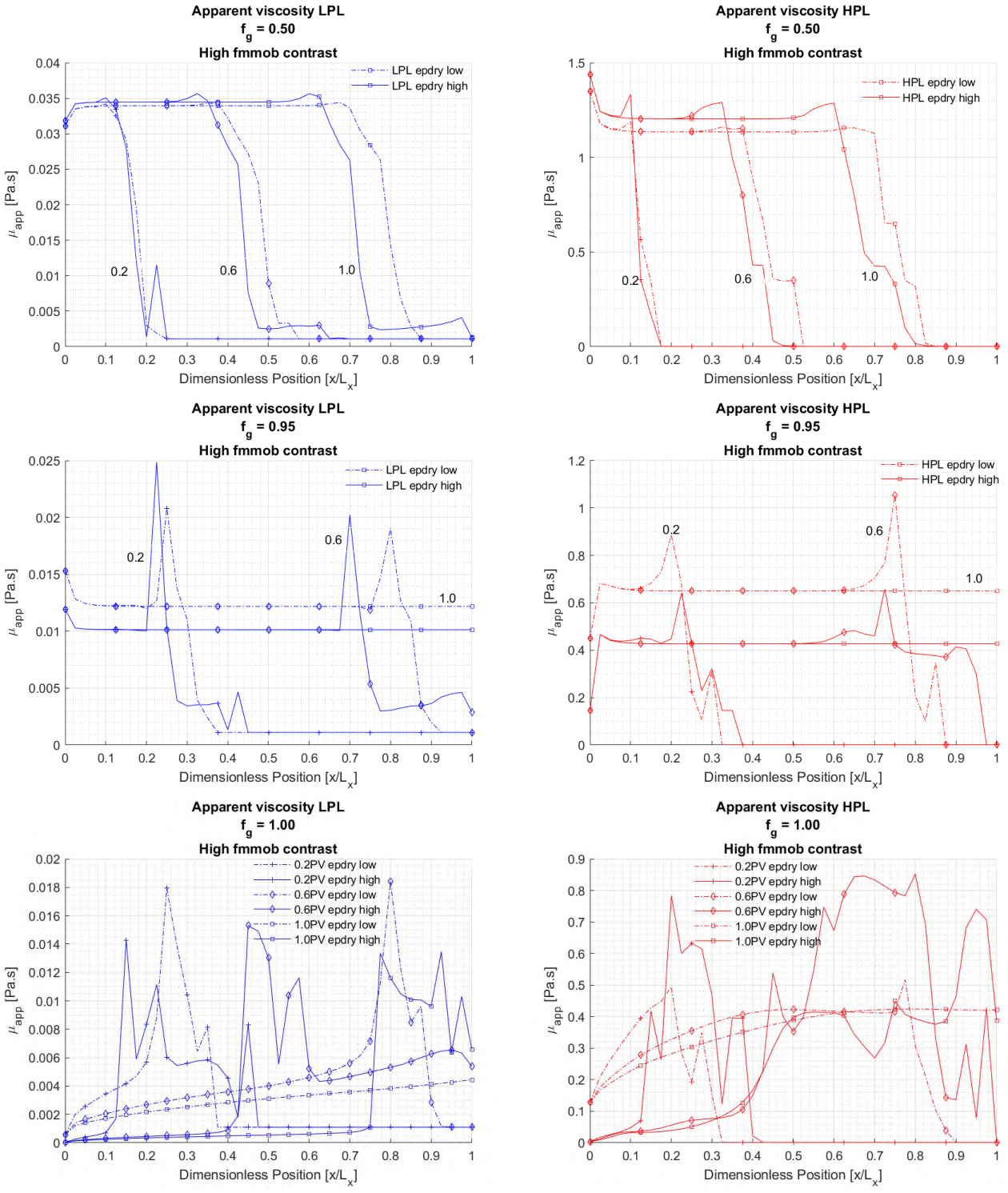

Figure 0.3 Apparent Viscosity profiles for high *fmmob* contrast for different qualities and injection volumes. Left: LPL. Right: HPL

Nomenclature

ρ: Mass density [kg/m^3]

x: Molar fraction [-]

W: Mass weight [kg]

w: Mass fraction [-]

MW: molecular Weight [kg/kmol]

$\dot{w}$ mass flowrate [kg/s]

q: volumetric flowrate [m^3/s]

q_{tot}: Total volumetric flowrate [m^3/s]

q_w: Water volumetric flowrate [m^3/s]

q_g: gas volumetric flowrate [m^3/s]

q_{na}: Non-aqueous phase volumetric flowrate [m^3/s]

K_{CO2}: CO_2 solubility in brine [kmol$_{co2}$/kg$_{h20}$]

V: Volume [m^3]

$\mu_{app.}$ apparent viscosity [pa.s]

μ_w: Water viscosity [pa.s]

μ_g: gas viscosity [pa.s]

k: Absolute permeability [m^2]

u_t: Total Velocity [m/s]

u_w: water velocity [m/s]

u_g: gas velocity [m/s]

∇p: Pressure gradient [pa/m]

k_{rw}: Water relative permeability

k_{rg}: gas relative permeability

λ: Mobility [m^2/(pa.s)]

λ_w: Water Mobility [m^2/(pa.s)]

λ_g: Gas Mobility [m^2/(pa.s)]

λ_g^f: Foam mobility [m^2/(pa.s)]

λ_{rw}: Water relative Mobility [1/(pa.s)]

λ_{rg}: Gas relative Mobility [1/(pa.s)]

λ_{rg}^f: Foam relative mobility [1/(pa.s)]

f_g: Gas fractional flow (quality) [-]

f_{na}: Non-aqueous phase fractional flow (quality) [-]

f_w: water fractional flow [-]

MCM: multiple contact miscibility

FCM: first contact miscibility

MMP: minimum miscibility pressure [Pa]

Pe: Peclet number [-]

t: time [s]

φ: porosity

l: length [m]

D: Diffusion coefficient [m^2/s]

S_w: Water saturation [-]

S_g: gas saturation [-]

S_{wc}: Connate/irreducible water saturation [-]

S_{gc}: irreducible gas saturation [-]

c: concentration

l_{diff}: Diffusion length [m]

t_{ch}: characteristic diffusion time [s]

IFT: Interfacial tension [N/m]

σ_{ow} : oil water interfacial tension [N/m]

$\sigma_{wg:}$: Water gas interfacial tension [N/m]

σ_{og}: Oil gas interfacial tension [N/m]

CMC: critical micelle concentration [-]

FM: IT foam model scaling factor [-]

$fmmob$: STARS model foam parameter [-]

$epdry$: STARS model foam parameter [-]

$fmdry$: STARS model foam parameter [-]

F_w: STARS model dryout function [-]

References

1. Advanced Resources International, Inc & Melzer Consulting. (2010). *OPTIMIZATION OF CO2 STORAGE IN CO2 ENHANCED OIL RECOVERY PROJECTS*.
2. Akasaka, R. (2008). A Reliable and Useful Method to Determine the Saturation State from Helmholtz Energy Equations of State. *Journal Of Thermal Science And Technology*, *3*(3), 442-451. doi: 10.1299/jtst.3.442
3. Al Ayesh, A., Salazar, R., Farajzadeh, R., Vincent-Bonnieu, S., & Rossen, W. (2017). Foam Diversion in Heterogeneous Reservoirs: Effect of Permeability and Injection Method. *SPE Journal*, *22*(05), 1402-1415. doi: 10.2118/179650-pa
4. Almajid, M., & Kovscek, A. (2016). Pore-level mechanics of foam generation and coalescence in the presence of oil. *Advances In Colloid And Interface Science*, *233*, 65-82. doi: 10.1016/j.cis.2015.10.008
5. Almaqbali, A., Spooner, V., Geiger, S., Arnold, D., & Mackay, E. (2017). Uncertainty Quantification for Foam Flooding in Fractured Carbonate Reservoirs. SPE Reservoir Simulation Conference. doi: 10.2118/182669-ms
6. Alvarez, J., Rivas, H., & Rossen, W. (2001). Unified Model for Steady-State Foam Behavior at High and Low Foam Qualities. *SPE Journal*, *6*(03), 325-333. doi: 10.2118/74141-pa
7. ANON, J. (2018). Risk assesment Matrix. Retrieved from http://www.jakeman.com.au/media/whats-right-with-risk-matrices
8. Bell, I., Wronski, J., Quoilin, S., & Lemort, V. (2014). Pure and Pseudo-pure Fluid Thermophysical Property Evaluation and the Open-Source Thermophysical Property Library CoolProp. *Industrial & Engineering Chemistry Research*, *53*(6), 2498-2508. doi: 10.1021/ie4033999
9. Bergeron, V., Fagan, M., & Radke, C. (1993). Generalized entering coefficients: a criterion for foam stability against oil in porous media. *Langmuir*, *9*(7), 1704-1713. doi: 10.1021/la00031a017
10. Bernard, G., & Jacobs, W. (1965). Effect of Foam on Trapped Gas Saturation and on Permeability of Porous Media to Water. Society Of Petroleum Engineers Journal, 5(04), 295-300. doi: 10.2118/1204-pa
11. Bertin, H., Apaydin, O., Castanier, L., & Kovscek, A. (1999). Foam Flow in Heterogeneous Porous Media: Effect of Cross Flow. *SPE Journal*, *4*(02), 75-82. doi: 10.2118/56009-pa
12. Buchgraber, M., Castanier, L., & Kovscek, A. (2012). Microvisual Investigation of Foam Flow in Ideal Fractures: Role of Fracture Aperture and Surface Roughness. *SPE Annual Technical Conference And Exhibition*. doi: 10.2118/159430-ms
13. Burriel, P., Claret, J., Ignés-Mullol, J., & Sagués, F. (2008). “Bottleneck Effect” in Two-Dimensional Microfluidics. *Physical Review Letters*, *100*(13). doi: 10.1103/physrevlett.100.134503
14. Casteel, J., & Djabbarah, N. (1988). Sweep Improvement in CO2 Flooding by Use of Foaming Agents. *SPE Reservoir Engineering*, *3*(04), 1186-1192. doi: 10.2118/14392-pa
15. Chalbaud, C., Moreno, R., & Alvarez, J. (2002). Simulating Foam Process for a Venezuelan Pilot Test. *SPE Annual Technical Conference And Exhibition*. doi: 10.2118/77699-ms
16. Computer Modelling Group. (2010). *STARS User’s Guide*. Calgary, Alberta, Canada: CMG.
17. Conn, C., Ma, K., Hirasaki, G., & Biswal, S. (2014). Visualizing oil displacement with foam in a microfluidic device with permeability contrast. *Lab Chip*, *14*(20), 3968-3977. doi: 10.1039/c4lc00620h
18. Eftekhari, A., Schüller, K., & Brosa Planella, F. (2015). FVTool: a finite volume toolbox for Matlab (Version doi: 10.5281/zenodo.32745).
19. Farajzadeh, R., Andrianov, A., Krastev, R., Hirasaki, G., & Rossen, W. (2012). Foam–oil interaction in porous media: Implications for foam assisted enhanced oil recovery. *Advances In Colloid And Interface Science*, *183-184*, 1-13. doi: 10.1016/j.cis.2012.07.002

20. Farajzadeh, R., Barati, A., Delil, H., Bruining, J., & Zitha, P. (2007). Mass Transfer of CO2 Into Water and Surfactant Solutions. Petroleum Science And Technology, 25(12), 1493-1511. doi: 10.1080/10916460701429498
21. Farajzadeh, R., Lotfollahi, M., Eftekhari, A., Rossen, W., & Hirasaki, G. (2015). Effect of Permeability on Implicit-Texture Foam Model Parameters and the Limiting Capillary Pressure. *Energy & Fuels*, *29*(5), 3011-3018. doi: 10.1021/acs.energyfuels.5b00248
22. Farajzadeh, R., Lotfollahi, M., Eftekhari, A., Rossen, W., & Hirasaki, G. (2015). Effect of Permeability on Implicit-Texture Foam Model Parameters and the Limiting Capillary Pressure. *Energy & Fuels*, *29*(5), 3011-3018. doi: 10.1021/acs.energyfuels.5b00248
23. Farajzadeh, R., Salimi, H., Zitha, P., & Bruining, H. (2007). Numerical simulation of density-driven natural convection in porous media with application for CO2 injection projects. International Journal Of Heat And Mass Transfer, 50(25-26), 5054-5064. doi: 10.1016/j.ijheatmasstransfer.2007.08.019
24. Gauteplass, J., Chaudhary, K., Kovscek, A., & Fernø, M. (2015). Pore-level foam generation and flow for mobility control in fractured systems. *Colloids And Surfaces A: Physicochemical And Engineering Aspects*, *468*, 184-192. doi: 10.1016/j.colsurfa.2014.12.043
25. Getrouw, N. (2016). *The static and dynamic behaviour of foam in a model porous media* (Master of Science). Delft University of Technology.
26. Harvard Apparatus. (2017). *PHD ULTRA 4400 Syringe pump series, Users's guide, 1 st ed. . Publication 5419-0004 Rev 1.0, p.11.*.
27. Helfferich, F. (1981). Theory of Multicomponent, Multiphase Displacement in Porous Media. *Society Of Petroleum Engineers Journal*, *21*(01), 51-62. doi: 10.2118/8372-pa
28. Jacobsen, R., & Stewart, R. (1973). Thermodynamic Properties of Nitrogen Including Liquid and Vapor Phases from 63K to 2000K with Pressures to 10,000 Bar. *Journal Of Physical And Chemical Reference Data*, *2*(4), 757-922. doi: 10.1063/1.3253132
29. Kagoro, R. (2017). *The effect of surfactant type, velocity and permeability on CO2 foam under miscible conditions* (Master's of Science). Delft University of Technology.
30. Kahrobaei, S., Li, K., Vincent-Bonnieu, S., & Farajzadeh, R. (2017). Effects of compositional variations on CO2 foam under miscible conditions. *Aiche Journal*, *64*(2), 758-764. doi: 10.1002/aic.15938
31. Kahrobaei, S., Vincent-Bonnieu, S., & Farajzadeh, R. (2017). Experimental Study of Hysteresis behavior of Foam Generation in Porous Media. *Scientific Reports*, *7*(1). doi: 10.1038/s41598-017-09589-0
32. Kapetas, L., Vincent Bonnieu, S., Farajzadeh, R., Eftekhari, A., Shafian, S., Bahrim, R., & Rossen, W. (2017). Effect of permeability on foam-model parameters: An integrated approach from core-flood experiments through to foam diversion calculations. *Colloids And Surfaces A: Physicochemical And Engineering Aspects*, *530*, 172-180. doi: 10.1016/j.colsurfa.2017.06.060
33. Khatib, Z., Hirasaki, G., & Falls, A. (1988). Effects of Capillary Pressure on Coalescence and Phase Mobilities in Foams Flowing Through Porous Media. *SPE Reservoir Engineering*, *3*(03), 919-926. doi: 10.2118/15442-pa
34. Kirby, Brian. *Micro- and nanoscale fluid mechanics: transport in microfluidic devices*. New York: Cambridge University Press, 2010. Print
35. Kovscek, A., & Bertin, H. (2002). Estimation of Foam Mobility in Heterogeneous Porous Media. *SPE/DOE Improved Oil Recovery Symposium*. doi: 10.2118/75181-ms
36. Kuhlman, M. (1990). Visualizing the Effect of Light Oil on CO2 Foams. *Journal Of Petroleum Technology*, *42*(07), 902-908. doi: 10.2118/17356-pa
37. Kunz, O., & Wagner, W. (2012). The GERG-2008 Wide-Range Equation of State for Natural Gases and Other Mixtures: An Expansion of GERG-2004. *Journal Of Chemical & Engineering Data*, *57*(11), 3032-3091. doi: 10.1021/je300655b

38. Lake, L. (2014). *Fundamentals of enhanced oil recovery*. Richardson, Tex.: Society of Petroleum Engineers.
39. Lee, H., & Heller, J. (1990). Laboratory Measurements of CO2-Foam Mobility. *SPE Reservoir Engineering*, *5*(02), 193-197. doi: 10.2118/17363-pa
40. Li, K. (2016). *The effects of oil on co2 foam flooding under miscible conditions.* (Master of Science). Delft University of Technology.
41. Li, R., Yan, W., Liu, S., Hirasaki, G., & Miller, C. (2010). Foam Mobility Control for Surfactant Enhanced Oil Recovery. *SPE Journal*, *15*(04), 928-942. doi: 10.2118/113910-pa
42. Li, Z., Song, X., Wang, Q., Zhang, L., guo, P., & Li, x. (2009). Enhance Foam Flooding Pilot Test in Chengdong Of Shengli Oilfield: Laboratory Experiment And Field Performance. International Petroleum Technology Conference. doi: 10.2523/iptc-13575-ms
43. Lifton, V. (2016). Microfluidics: an enabling screening technology for enhanced oil recovery (EOR). *Lab On A Chip*, *16*(10), 1777-1796. doi: 10.1039/c6lc00318d
44. Liu, Y., Teng, Y., Lu, G., Jiang, L., Zhao, J., Zhang, Y., & Song, Y. (2016). Experimental study on CO2 diffusion in bulk n-decane and n-decane saturated porous media using micro-CT. Fluid Phase Equilibria, 417, 212-219. doi: 10.1016/j.fluid.2016.02.034
45. Lotfollahi, M., Farajzadeh, R., Delshad, M., Varavei, A., & Rossen, W. (2016). Comparison of Implicit-Texture and Population-Balance Foam Models. *SPE EOR Conference At Oil And Gas West Asia*. doi: 10.2118/179808-ms
46. Ma, K., Liontas, R., Conn, C., Hirasaki, G., & Biswal, S. (2012). Visualization of improved sweep with foam in heterogeneous porous media using microfluidics. *Soft Matter*, *8*(41), 10669. doi: 10.1039/c2sm25833a
47. Ma, K., Lopez-Salinas, J., Puerto, M., Miller, C., Biswal, S., & Hirasaki, G. (2013). Estimation of Parameters for the Simulation of Foam Flow through Porous Media. Part 1: The Dry-Out Effect. *Energy & Fuels*, *27*(5), 2363-2375. doi: 10.1021/ef302036s
48. Ma, K., Lopez-Salinas, J., Puerto, M., Miller, C., Biswal, S., & Hirasaki, G. (2013). Estimation of Parameters for the Simulation of Foam Flow through Porous Media. Part 1: The Dry-Out Effect. *Energy & Fuels*, *27*(5), 2363-2375. doi: 10.1021/ef302036s
49. Marsden, S. (1986). *Foams in Porous Media, SUPRI TR-49*.
50. Moradi-Araghi, A., Johnston, E., Zornes, D., & Harpole, K. (1997). Laboratory Evaluation of Surfactants for CO2-Foam Applications at the South Cowden Unit. *International Symposium On Oilfield Chemistry*. doi: 10.2118/37218-ms
51. Orr, F., Dindoruk, B., & Johns, R. (1995). Theory of Multicomponent Gas/Oil Displacements. *Industrial & Engineering Chemistry Research*, *34*(8), 2661-2669. doi: 10.1021/ie00047a015
52. Osei-Bonsu, K., Grassia, P., & Shokri, N. (2017). Investigation of foam flow in a 3D printed porous medium in the presence of oil. *Journal Of Colloid And Interface Science*, *490*, 850-858. doi: 10.1016/j.jcis.2016.12.015
53. Osterloh, W., & Jante, M. (1992). Effects of Gas and Liquid Velocity on Steady-State Foam Flow at High Temperature. *SPE/DOE Enhanced Oil Recovery Symposium*. doi: 10.2118/24179-ms
54. Osterloh, W., & Jante, M. (1992). Effects of Gas and Liquid Velocity on Steady-State Foam Flow at High Temperature. *SPE/DOE Enhanced Oil Recovery Symposium*. doi: 10.2118/24179-ms
55. Outcalt, S., & McLinden, M. (1996). A Modified Benedict–Webb–Rubin Equation of State for the Thermodynamic Properties of R152a (1,1-difluoroethane). Journal Of Physical And Chemical Reference Data, 25(2), 605-636. doi: 10.1063/1.555979
56. Owete, O., & Brigham, W. (1984). *"A Micromodel Study of Foam Flow through Porous Media, "SUPRI TR-37,[DOE/SF/11564-6]*.
57. Patil, P., Knight, T., Katiyar, A., Vanderwal, P., Scherlin, J., & Rozowski, P. et al. (2018). CO₂ Foam Field Pilot Test in Sandstone Reservoir: Complete Analysis of Foam Pilot Response. *SPE Improved Oil Recovery Conference*. doi: 10.2118/190312-ms

58. Peng, D., & Robinson, D. (1976). A New Two-Constant Equation of State. *Industrial & Engineering Chemistry Fundamentals*, *15*(1), 59-64. doi: 10.1021/i160057a011
59. Peters, E. (2012). *Advanced petrophysics*. Austin (TX): Live Oak Book Company.
60. Peters, E. (2012). *Advanced petrophysics*. Austin, TX: Live Oak Book Company.
61. Quennouz, N., Ryba, M., Argillier, J., Herzhaft, B., Peysson, Y., & Pannacci, N. (2012). Microfluidic Study of Foams Flow for Enhanced Oil Recovery (EOR). *Oil & Gas Science And Technology – Revue D'IFP Energies Nouvelles*, *69*(3), 457-466. doi: 10.2516/ogst/2014017
62. Ransohoff, T., & Radke, C. (1988). Mechanisms of Foam Generation in Glass-Bead Packs. *SPE Reservoir Engineering*, *3*(02), 573-585. doi: 10.2118/15441-pa
63. Rossen, W. (2013). Numerical Challenges in Foam Simulation: A Review. *SPE Annual Technical Conference And Exhibition*. doi: 10.2118/166232-ms
64. Sagar, N., & Castanier, L. (1997). *Oil-Foam Interactions in a Micromodel, SUPRI TR 110,[DOE/BC/14994]*.
65. Schramm, L. (2005). *Emulsions, foams, and suspensions*. Weinheim: Wiley-VCH.
66. Schramm, L., & Novosad, J. (1990). Micro-visualization of foam interactions with a crude oil. *Colloids And Surfaces*, *46*(1), 21-43. doi: 10.1016/0166-6622(90)80046-7
67. Sheng, J. (2011). *Modern chemical enhanced oil recovery*. [Place of publication not identified]: Gulf Professional.
68. Sheng, J. (2013). *Enhanced oil recovery field case studies*. Waltham, Mass.: Elsevier.
69. Song, Y., Jian, W., Zhang, Y., Shen, Y., Zhan, Y., & Zhao, J. et al. (2012). Densities and Volumetric Characteristics of Binary System of CO2 + Decane from (303.15 to 353.15) K and Pressures up to 19 MPa. *Journal Of Chemical & Engineering Data*, *57*(12), 3399-3407. doi: 10.1021/je300388b
70. Song, Y., Jian, W., Zhang, Y., Xing, W., Zhan, Y., Liu, S., & Li, T. (2014). Density Behavior of CO2 + Decane Mixtures by Modified SAFT Equation of State. *Energy Procedia*, *61*, 440-444. doi: 10.1016/j.egypro.2014.11.1144
71. Speight, J. *Introduction to Enhanced Recovery Methods for Heavy Oil and Tar Sands*.
72. Tabeling, P. (2011). *Introduction to microfluidics*. Oxford: Oxford University Press.
73. Teng, Y., Liu, Y., Song, Y., Jiang, L., Zhao, Y., & Zhou, X. et al. (2014). A Study on CO2 Diffusion Coefficient in n-decane Saturated Porous Media by MRI. *Energy Procedia*, *61*, 603-606. doi: 10.1016/j.egypro.2014.11.1180
74. Wenjuan Liu's Portfolio: MatSE 447 - Lesson Plan. (2017). Retrieved from http://php.scripts.psu.edu/users/w/z/wzl113/Lesson%20Plan.htm
75. Zambrano, J., Gómez-Soto, F., Lozano-Martín, D., Martín, M., & Segovia, J. (2016). Volumetric behaviour of (carbon dioxide+hydrocarbon) mixtures at high pressures. *The Journal Of Supercritical Fluids*, *110*, 103-109. doi: 10.1016/j.supflu.2016.01.002
76. Zhao, H. (2018). CO2-Brine Phase Equilibria model-PART 1: CO2 solubility in pure H2O and in a single-salt brine. Retrieved from http://www.energy.psu.edu/tools/psuco20730/index.php
77. Zhao, H., Fedkin, M., Dilmore, R., & Lvov, S. (2015). Carbon dioxide solubility in aqueous solutions of sodium chloride at geological conditions: Experimental results at 323.15, 373.15, and 423.15 K and 150 bar and modeling up to 573.15 K and 2000 bar. *Geochimica Et Cosmochimica Acta*, *149*, 165-189. doi: 10.1016/j.gca.2014.11.004
78. Zinati, F., Farajzadeh, R., & Zitha, P. (2008). Foam Modeling in Heterogeneous Reservoirs Using Stochastic Bubble Population Approach. *SPE Symposium On Improved Oil Recovery*. doi: 10.2118/113358-ms